LA-UR -90-2060

CONF-9003179--1

Los Alamos National Laboratory is operated by the University of California for the United States Department of Energy under contract W-7405-ENG-36.

LA-UR--90-2060

DE90 013165

TITLE: ATMOSPHERIC MODELING IN COMPLEX TERRAIN

AUTHOR(S): M. D. Williams
G. E. Streit

SUBMITTED TO: Centro Internacional de
Fisica Y Matematicas Aplicados

Los Alamos National Laboratory
Los Alamos, New Mexico 87545

FORM NO. 836 R4
ST. NO. 2629 5/81

DISCLAIMER

issued: May 1990

Atmospheric Modeling in Complex Terrain

M. D. Williams and G. E. Streit

LOS ALAMOS

LOS ALAMOS NATIONAL LABORATORY
LOS ALAMOS, NEW MEXICO 87545

An Affirmative Action/Equal Opportunity Employer

This work was supported by the U.S. Department Energy,
Office of Policy, Planning and Analysis.

DISCLAIMER

Contents

List of Figures

Atmospheric Modeling in Complex Terrain

Michael D. Williams Gerald E. Streit

March 14, 1990

Abstract

Los Alamos investigators have developed several models which are relevant to modeling Mexico City air quality. The collection of models includes: (1) meteorological models, (2) dispersion models, (3) air chemistry models, and (4) visibility models. The models have been applied in several different contexts. They have been developed primarily to address the complexities posed by complex terrain. HOTMAC is the meteorological model which requires terrain and limited meteorological information. HOTMAC incorporates a relatively complete description of atmospheric physics to give good descriptions of the wind, temperature, and turbulence fields. RAPTAD is a dispersion code which uses random particle transport and kernel representations to efficiently provide accurate pollutant concentration fields. RAPTAD provides a much better description of tracer dispersion than do Gaussian puff models which fail to properly represent the effects of the wind profile near the surface.

ATMOS and LAVM treat photochemistry and visibility respectively. ATMOS has been used to describe wintertime chemistry of the Denver brown cloud. Its description provided reasonable agreement with measurements for the high altitude of Denver. LAVM can provide both numerical indices or pictoral representations of visibility effects of pollutants.

1 Introduction

Los Alamos investigators have developed several models which are relevant to modeling Mexico City air quality. The collection of models includes: (1) meteorological models, (2) dispersion models, (3) air chemistry models, and (4) visibility models. The models have been applied in several different contexts. They have been developed primarily to address the complexities posed by complex terrain.

The objective of this paper is to describe the models and their use. Model physics, important considerations in their use, and some past applications will be described.

2 Model System Overview

Figure 1 summarizes the objectives, scale, outputs, and applications of the atmospheric models. Figure 2 provides a summary of the characteristics of the meteorological and plume dispersion components of the modeling system. Turbulence is treated with a higher order closure approach (Yamada, 1978) which provides a more complete description of turbulence. The cloud description is currently incomplete. The model forms clouds, and, with sufficient vertical resolution near the cloud top it treats long wave radiation cooling. The model does not treat the effects of clouds on shortwave radiation, nor does it treat precipitation.

The model does treat complex terrain, tree canopies, and snow cover. A one-dimensional version of the model treats soil moisture. At present only the drag and radiation effects of tree canopies are treated (Yamada, 1982).

The model describes both solar and long wave radiation. It uses a nested grid and it can assimilate measured data into its description, if such data is available.

The dispersion model uses the transport of pseudo-particles to describe dispersion and transport. Pseudo-particle locations are transformed into pollutant concentrations with a kernel density estimator which uses integrated turbulence parameters to describe spread parameters (Yamada and Bunker,1989).

The meteorological and dispersion models have been used with a variety of computers ranging from Cray super computers to IBM-AT computers with 32 bit add-in boards.

Figure 3 describes the overall modeling system and its various components, inputs, and outputs. The meteorological model HOTMAC (Higher Order Turbulence Model for Atmospheric Circulation) requires inputs which describe meteorological conditions and terrain. Its direct output includes wind and temperature fields and mixing depths. It also supplies the transport model with a variety of other parameters which are related to the turbulent transport of materials.

The transport and diffusion code, RAPTAD (RAndom Particle Transport And Diffusion) code requires source data in addition to the information it receives from HOTMAC. It provides a direct estimate of the concentrations of stable pollutants or pollutants with a specified decay rate.

The atmospheric chemistry model, ATMOS requires source speciation, atmospheric background, and actinic fluxes in addition to inputs from RAPTAD. It provides concentrations of reactive pollutants.

The visibility model, LAVM, requires observer geometry and background visibility. It has two forms of output; visibility indices and a picture. The visibility indices describe plume contrast, visible range, and extinction coefficients while the picture depicts a scene as altered by pollutants. A clean starting picture is required if a picture form of output is desired.

LANL Mesoscale Atmospheric Modeling Capability

Objectives

Prediction of Airflows and Pollutant Transport over Complex Terrain

Scale

Horizontal	10 km to 2000 km
Vertical	Up to 10 km
Time	Up to a few diurnal cycles

Outputs

Time Dependent, 3-D Distributions of Wind, Temperature, Humidity, Pressure and Turbulence

Plume Trajectories, Concentration Distribution

Applications

Air Quality Study
Complex Terrain Meteorology
Emergency Preparedness Planning

Figure 1: Summary of Atmospheric Modeling Capability

Characteristics of the LANL Mesoscale Models

Turbulence:	**Second-Moment Closure**
Cloud:	**Statistical Process**
Surface:	**Complex Terrain, Tree Canopy, Snow Cover, Soil Moisture**
Radiation:	**Solar and Longwave**
Numerical:	**Nested Grid, 4-D Data Assimilation**
Plume:	**Lagrangian Operator**
Concentration:	**Kernel Density Estimator**
Computer:	**Super / Desktop**

Figure 2: Summary of Characteristics of the LANL Mesoscale Models

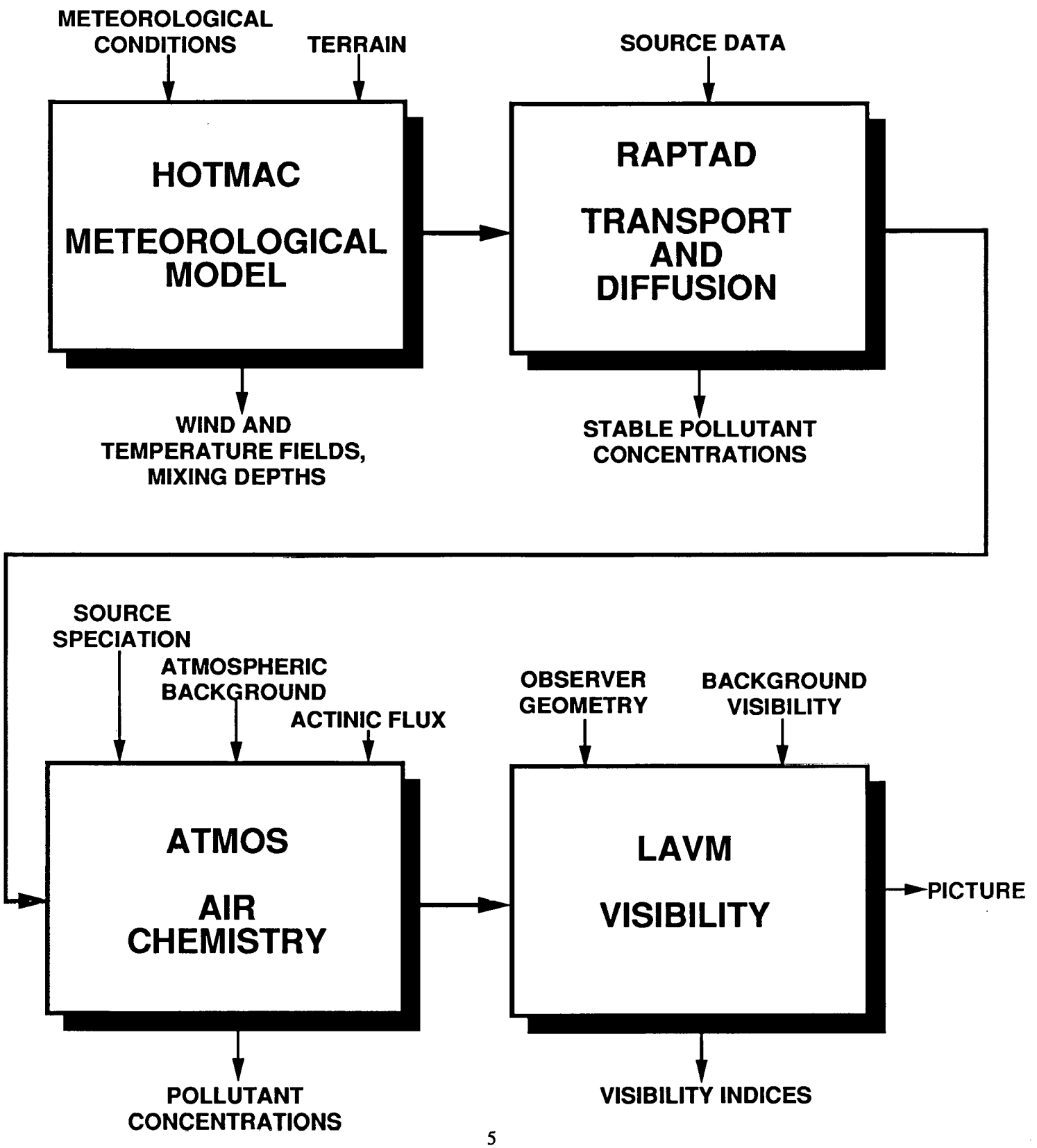

Figure 3: Information Flow in the Air Quality Modeling System

3 The Meteorological Modeling System HOTMAC

3.1 Model formulation

HOTMAC is a three-dimensional time-dependent model developed by T. Yamada (Yamada, 1985). It uses the hydrostatic approximation and a terrain following coordinate system in which the vertical coordinate z^*, is given by:

$$z^* = \bar{H}\frac{z - z_g}{H - z_g} \tag{1}$$

where z_g is the height of the ground and H is the height of the top of model domain. $\bar{H}$ is equal to H minus the height of the highest terrain in the domain.

HOTMAC solves conservation relations for the horizontal wind components, potential temperature, moisture, turbulent kinetic energy, and the turbulence length scale. HOTMAC describes advection, coriolis effects, turbulent transfer of heat, momentum, and moisture. It also describes solar and terrestrial radiation effects, turbulent history effects, and drag and radiation effects of forest canopies.

Equation 2 represents the conservation equation for the east-west component of momentum. The total rate of change of the u component of the wind is equal to the sum of a coriolis term, a buoyancy term, two horizontal eddy transport terms and a vertical momentum transport term.

$$\frac{DU}{Dt} = f(V - V_g) + g\frac{\overline{H} - z^*}{\overline{H}}\left(1 - \frac{\langle\Theta_v\rangle}{\Theta_v}\right)\frac{\partial z_g}{\partial x} + \frac{\partial}{\partial x}\left(K_x\frac{\partial U}{\partial x}\right) + \frac{\partial}{\partial y}\left(K_{xy}\frac{\partial U}{\partial y}\right) + \frac{\overline{H}}{H - z_g}\frac{\partial}{\partial z^*}(-\overline{uw}). \tag{2}$$

V_g is the north-south component of the geostrophic wind. $\langle\theta_v\rangle$ is the horizontal average of the virtual potential temperature. Equation 3 is a similar expression for the north-south components of momentum.

$$\frac{DV}{Dt} = -f(U - U_g) + g\frac{\overline{H} - z^*}{\overline{H}}\left(1 - \frac{\langle\Theta_v\rangle}{\Theta_v}\right)\frac{\partial z_g}{\partial y} + \frac{\partial}{\partial x}\left(K_{xy}\frac{\partial V}{\partial x}\right) + \frac{\partial}{\partial y}\left(K_y\frac{\partial V}{\partial y}\right) + \frac{\overline{H}}{H - z_g}\frac{\partial}{\partial z^*}(-\overline{vw}). \tag{3}$$

Equation 4 is derived from the hydrostatic approximation and it describes the vertical velocity W^*, in the z^* coordinate system.

$$\frac{\partial U}{\partial x} + \frac{\partial V}{\partial y} + \frac{\partial W^*}{\partial z^*} - \frac{1}{H - z_g}\left(U\frac{\partial z_g}{\partial x} + V\frac{\partial z_g}{\partial y}\right) = 0. \tag{4}$$

Equation 5 is the energy conservation equation which describes the total rate of change of the potential temperature.

$$\frac{D\Theta}{Dt} = \frac{\partial}{\partial x}\left[K_x \frac{\partial \Theta}{\partial x}\right] + \frac{\partial}{\partial y}\left[K_y \frac{\partial \Theta}{\partial y}\right] + \frac{\overline{H}}{H - z_g}\left[\frac{\partial}{\partial z^*}(-\overline{w\theta}) + \frac{1}{\rho C_p}\frac{\partial R_N}{\partial z^*}\right]. \quad (5)$$

The last two terms are the contributions from divergence of the sensible heat flux and divergence of the radiation field. $R - N$ is the long wave radiation flux.

Equation 6 describes the conservation of moisture mixing ratio.

$$\frac{DQ_v}{Dt} = \frac{\partial}{\partial x}\left[K_x \frac{\partial Q_v}{\partial x}\right] + \frac{\partial}{\partial y}\left[K_y \frac{\partial Q_v}{\partial y}\right] + \frac{\overline{H}}{H - z_g}\frac{\partial}{\partial z^*}(-\overline{wq_v}). \quad (6)$$

An important difference between the higher order turbulence models such as this one and simpler models is the treatment of turbulent fluxes, described by equations 7 and 8 (Yamada,1975).

$$\overline{uw} = -1q\tilde{S}_M \frac{\partial U}{\partial z}. \quad (7)$$

$$\overline{w\theta} = -\alpha 1 q \tilde{S}_M \frac{\partial \Theta}{\partial z}. \quad (8)$$

The turbulent fluxes involve two other factors: l, and q in addition to the gradients and the factor $\tilde{S}_M$ which is a function of the flux Richardson number. Simpler models would use some form of the latter two factors, but not q the turbulence speed or l which is the turbulence length scale. q and l are obtained by solving equations 9 and 10.

$$\begin{aligned}\frac{D}{Dt}\left(\frac{q^2}{2}\right) = {} & \frac{\partial}{\partial x}\left[K_x \frac{\partial}{\partial x}\left(\frac{q^2}{2}\right)\right] + \frac{\partial}{\partial y}\left[K_y \frac{\partial}{\partial y}\left(\frac{q^2}{2}\right)\right] \\ & + \left(\frac{\overline{H}}{H - z_g}\right)^2 \frac{\partial}{\partial z^*}\left[q1S_q \frac{\partial}{\partial z^*}\left(\frac{q^2}{2}\right)\right] \\ & - \frac{\overline{H}}{H - z_g}\left(\overline{uw}\frac{\partial U}{\partial z^*} + \overline{vw}\frac{\partial V}{\partial z^*}\right) + \beta g \overline{w\theta_v} - \frac{q^3}{B_1 1}.\end{aligned} \quad (9)$$

$$\begin{aligned}\frac{D}{Dt}(q^2 1) = {} & \frac{\partial}{\partial x}\left[K_x \frac{\partial}{\partial x}(q^2 1)\right] + \frac{\partial}{\partial y}\left[K_y \frac{\partial}{\partial y}(q^2 1)\right] \\ & + \left(\frac{\overline{H}}{H - z_g}\right)^2 \frac{\partial}{\partial z^*}\left[q1S_1 \frac{\partial}{\partial z^*}(q^2 1)\right] \\ & + 1F_1\left[\frac{\overline{H}}{H - z_g}\left(-\overline{uw}\frac{\partial U}{\partial z^*} - \overline{vw}\frac{\partial V}{\partial z^*}\right) + \beta g \overline{w\theta_v}\right] \\ & - \frac{q^3}{B_1}\left[1 + F_2\left(\frac{1}{kz}\right)^2\right].\end{aligned} \quad (10)$$

The development of these equations and form of the factors is described in Yamada (1981) and Mellor and Yamada (1982).

Within the soil, equation 11 applies:

$$\frac{\partial T_s}{\partial t} = \frac{\partial}{\partial z_s}\left(K_s \frac{\partial T_s}{\partial z_s}\right). \tag{11}$$

A key feature of the model is its description of the surface energy budget equation 12.

$$R_s + R_L \downarrow - R_L \uparrow = H_s + LE + G_s. \tag{12}$$

R_s is the solar shortwave radiation flux, while $R_L \downarrow$ is the downward long wave atmospheric flux and $R_L \uparrow$ is the blackbody radiation from the surface. The sensible heat flux H_s, is given by:

$$H_s = -\rho_a c_p u^* \theta^*. \tag{13}$$

where u^* is the friction velocity and θ^* is a temperature scale which is defined by:

$$\theta^* = \frac{k}{P_r} \frac{(\Theta(z_1) - \Theta_G)}{\left[In\left(\frac{z_1 + z_{o1}}{z_o}\right) + In\left(\frac{z_o}{z_t}\right) - \Psi\right]}. \tag{14}$$

In equation 14, Ψ is a stability correction factor which is zero during neutral atmospheric stability. Similar expressions are used to define u^* except that velocity at the ground is zero. LE is the latent energy flux and G_s is the soil heat flux. Equations 15 and 16 describe these variables.

$$LE = \rho_a L u^* Q^*. \tag{15}$$

$$G_s = -K_s \frac{\partial T_s}{\partial z_s}|_G. \tag{16}$$

In an urban context the surface energy balance requires an additional term which represents the heat released by man's activities. The additional heat along with differences in thermal properties between urban and non-urban surfaces produces the urban heat island.

3.2 Model usage

HOTMAC requires both terrain and meteorological inputs. Figure 4 summarizes the meteorological input required for the model. The model begins with a temperature field which is horizontally uniform. Initial potential temperatures are derived from the potential temperature at sea level and the potential temperature gradients below the height of the point which is being initialized. The vertical potential temperature is idealized as composed of up to three line segments which are continuous but have different slopes. The breakpoints are

HOTMAC METEOROLOGICAL INPUT

- JULIAN DAY
- LOCAL STANDARD TIME
- POTENTIAL TEMPERATURE AT SEA LEVEL (°C)
- POTENTIAL TEMPERATURE GRADIENT BENEATH INVERSION
- POTENTIAL TEMPERATURE GRADIENT ABOVE INVERSION
- HEIGHT ABOVE SEA LEVEL OF TEMPERATURE INVERSION
- NUMBER OF TIME STEPS AND MAXIMUM TIME STEP
- INITIAL WIND DIRECTION
- WIND SPEED
- RELATIVE HUMIDITY AT SURFACE AND ABOVE

Figure 4: Summary of HOTMAC Meteorological Input

defined by the input parameters elev1 and elev2, which are referenced to sea-level. Meteorological inputs should be chosen to be synoptic scale values. For example, figure 5 is a vertical profile of potential temperature as measured by a rawinsonde launched from the Mexico City airport. The sounding was taken at zero hours GMT, and consequently represents a late afternoon profile. In this example, the break points would probably be chosen as about 1. km above the airports elevation of 2240 meters, or 3240 meters. The next breakpoint would be about 5200 msl. The lowest 100 meters of the profile would not be represented because it is a local effect that the model's surface energy budget should produce. Figure 6 represents a temperature profile for the same sounding. Figure 7 represents a wind speed profile for the same sounding, while figure 8 describes the wind direction profile. The large excursion in direction at a height a little below 2 km is only a single point which could have been plotted near zero wind direction. There are two options for this profile: (1) a single representative wind speed and a single representative wind direction could be chosen, or (2) break points could be used which force the winds to prescribed values at two different heights.

The situation becomes somewhat more complicated during the morning and evening when stable temperature profiles produce local conditions which exhibit greater variation from one point to another. Figure 9 displays a potential temperature profile for the 12 GMT sounding on the morning following the example discussed above. Figures 10 and 11 show the wind speed and wind direction profiles respectively. In this case the structure is somewhat more complicated and there is another potential difficulty. The measured wind includes both the synoptic scale effects and the local effects which are produced by slopes and temperature differences between points. In the afternoon case the temperature differences would tend to be more uniform because a well-mixed atmosphere tends to produce uniform potential temperatures. However, during the nighttime the conditions are more variable and the initial potential temperature distribution may not provide a good representation.

The result of poorer representation is that the initial temperature field will be quickly altered to one which is more representative. However, the adjustment of the temperatures will be accompanied by adjustments in the wind fields, so that the wind field may bear little resemblance to the initial wind field. In the past we have resolved this problem by initializing the model with a very light wind field and then adjusted the wind field to the desired initial field after a more realistic temperature field has been obtained.

Figure 12 lists the major topographic inputs used by HOTMAC. In an urban application, urbanized area must also be included. The selection of the grid size and the domain (or total inclusive area) is very important. Figure 13 displays a streamline analysis based on measurements taken in the vicinity of the Great Salt Lake (Astling, 1986) in the state of Utah in the United States. We have carried out measurements, tracer studies, and model simulations to describe the fate of materials (Yamada, et al., 1989) which might be released near the

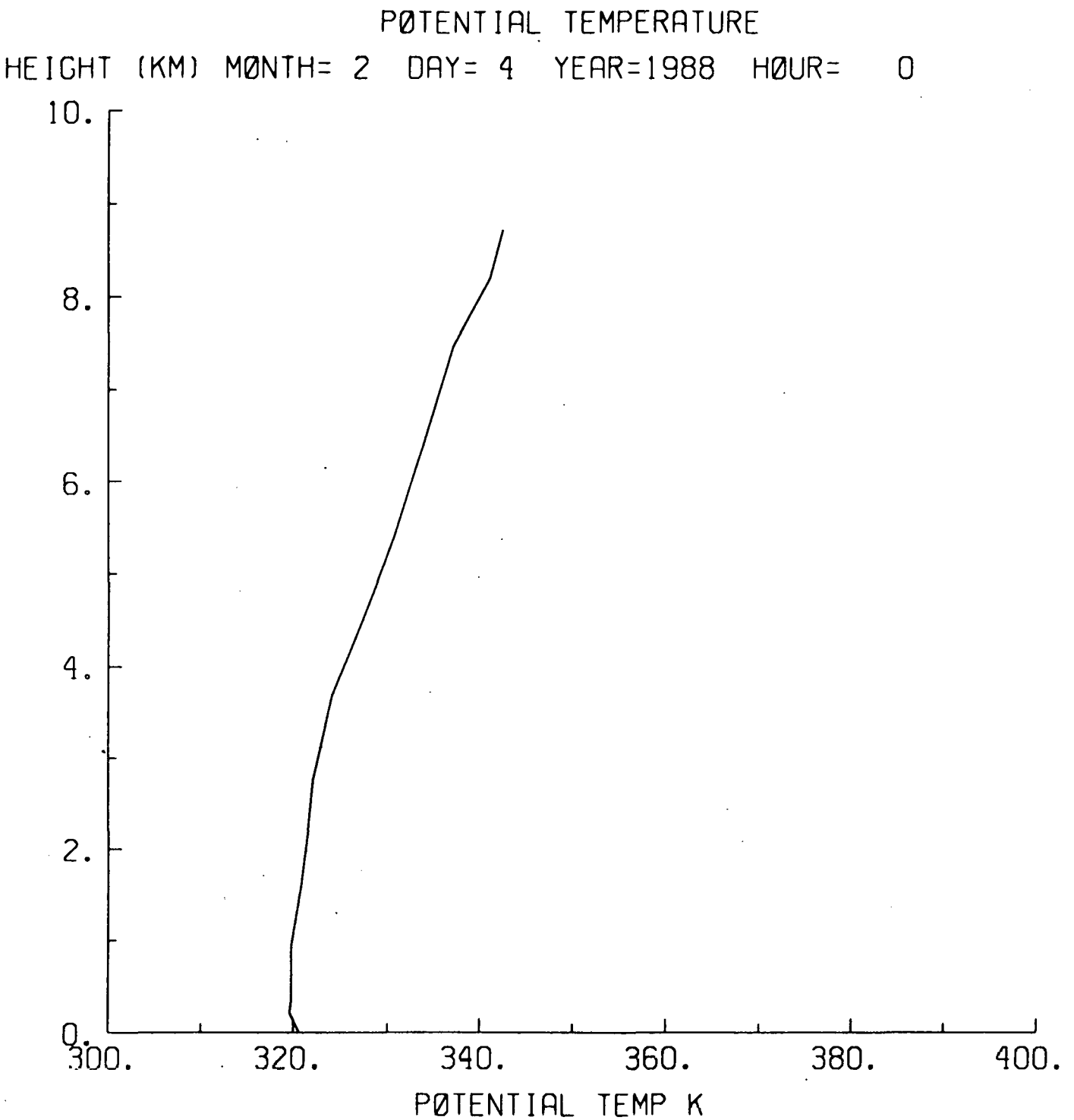

Figure 5: Vertical Profile of Potential Temperature above the Mexico City Airport on February 3, 1988 at 6 pm local time

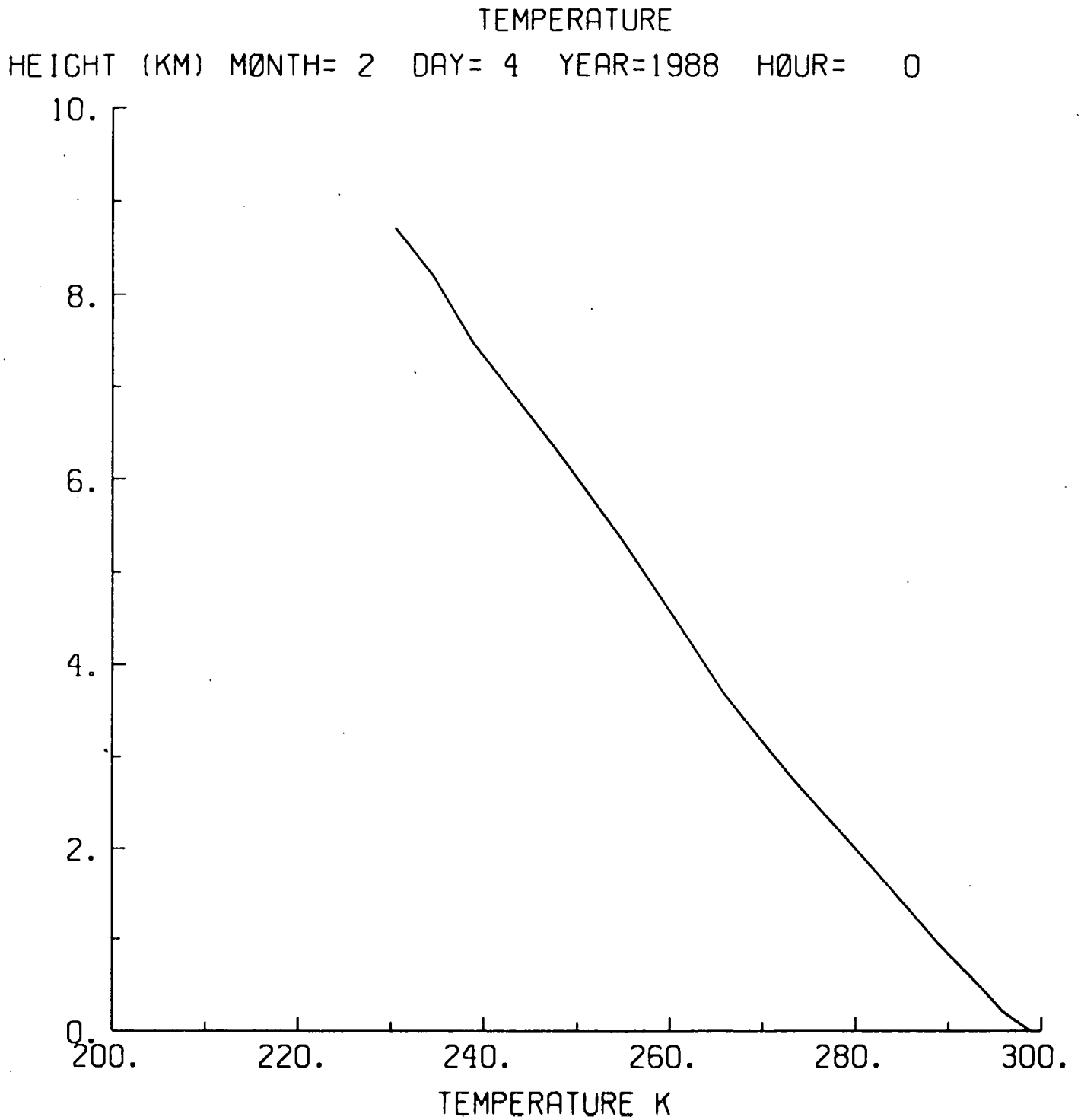

Figure 6: Vertical Profile of Temperature above the Mexico City Airport on February 3, 1988 at 6 pm local time

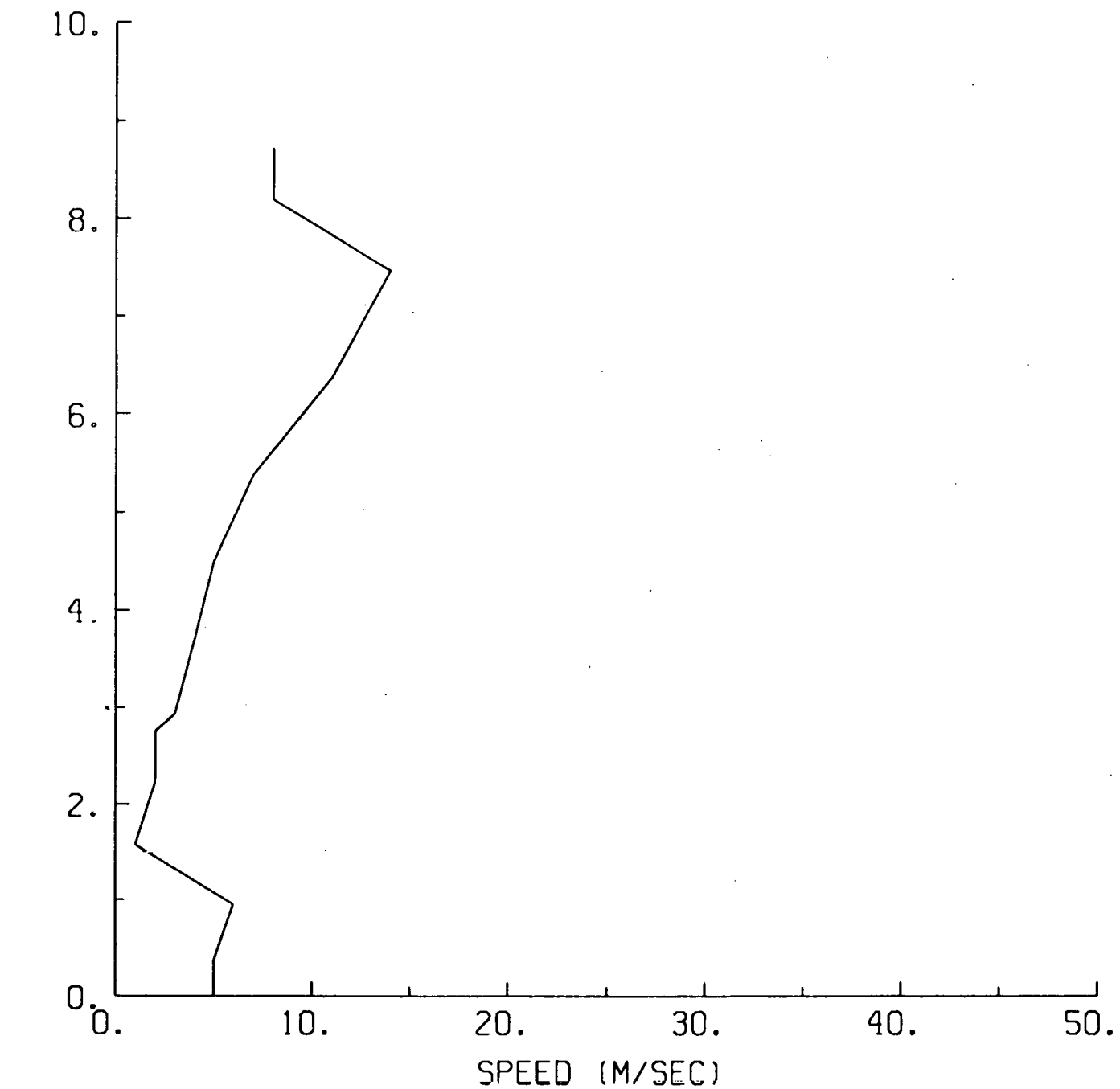

Figure 7: Vertical Profile of Wind Speed above the Mexico City Airport on February 3, 1988 at 6 pm local time

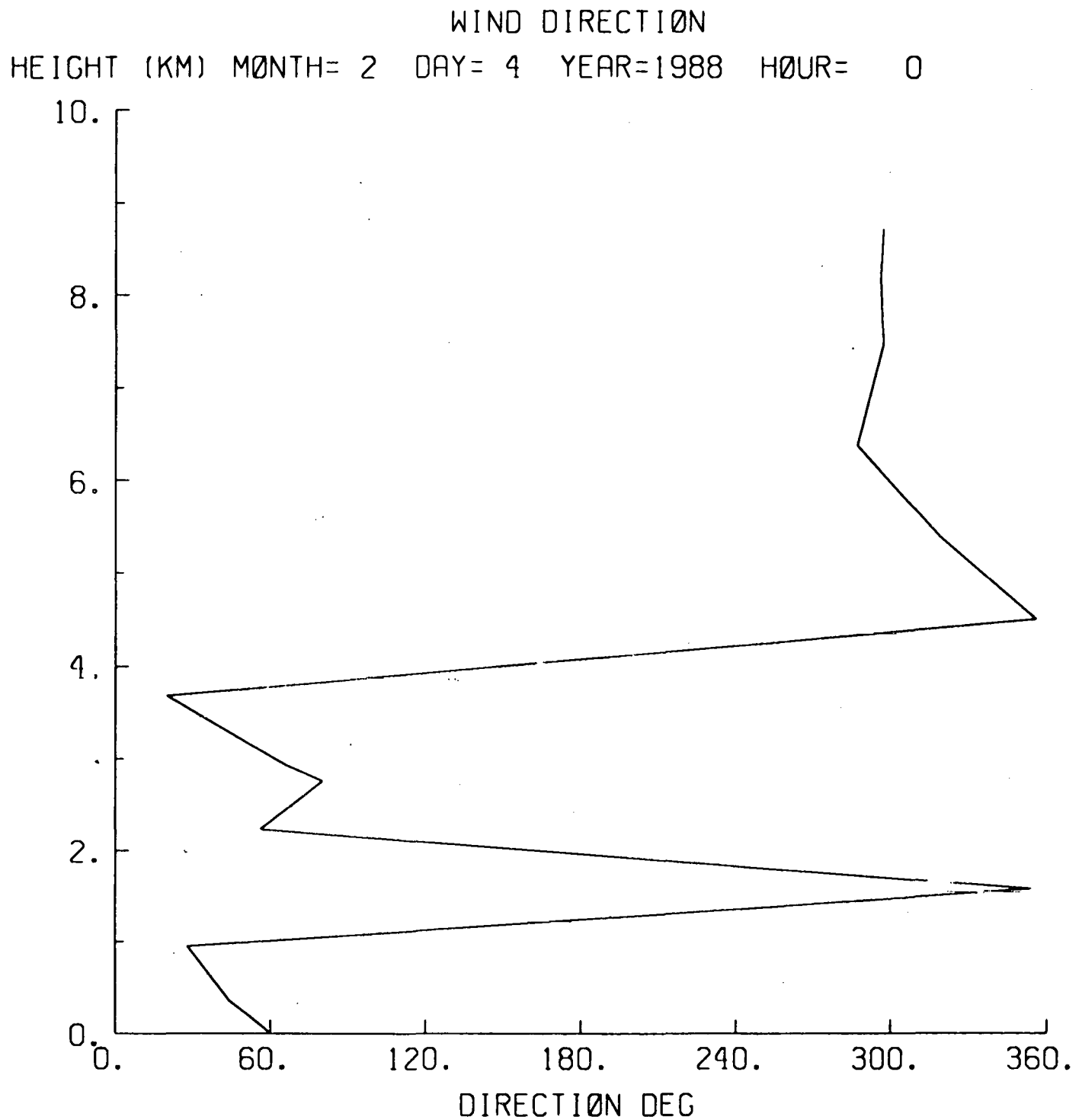

Figure 8: Vertical Profile of Wind Direction above the Mexico City Airport on February 3, 1988 at 6 pm local time

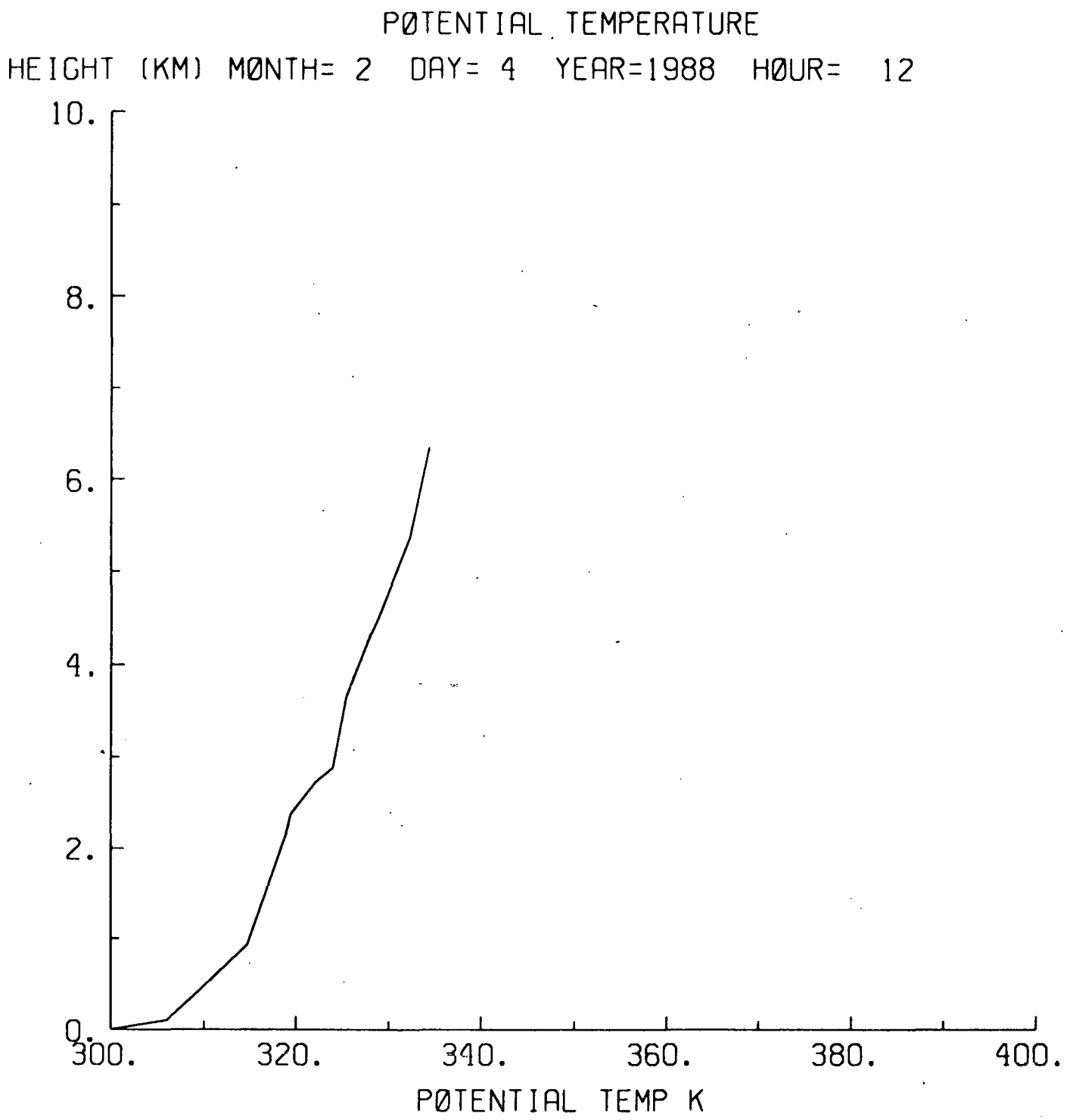

Figure 9: Vertical Profile of Potential Temperature above the Mexico City Airport on February 4, 1988 at 6 am local time

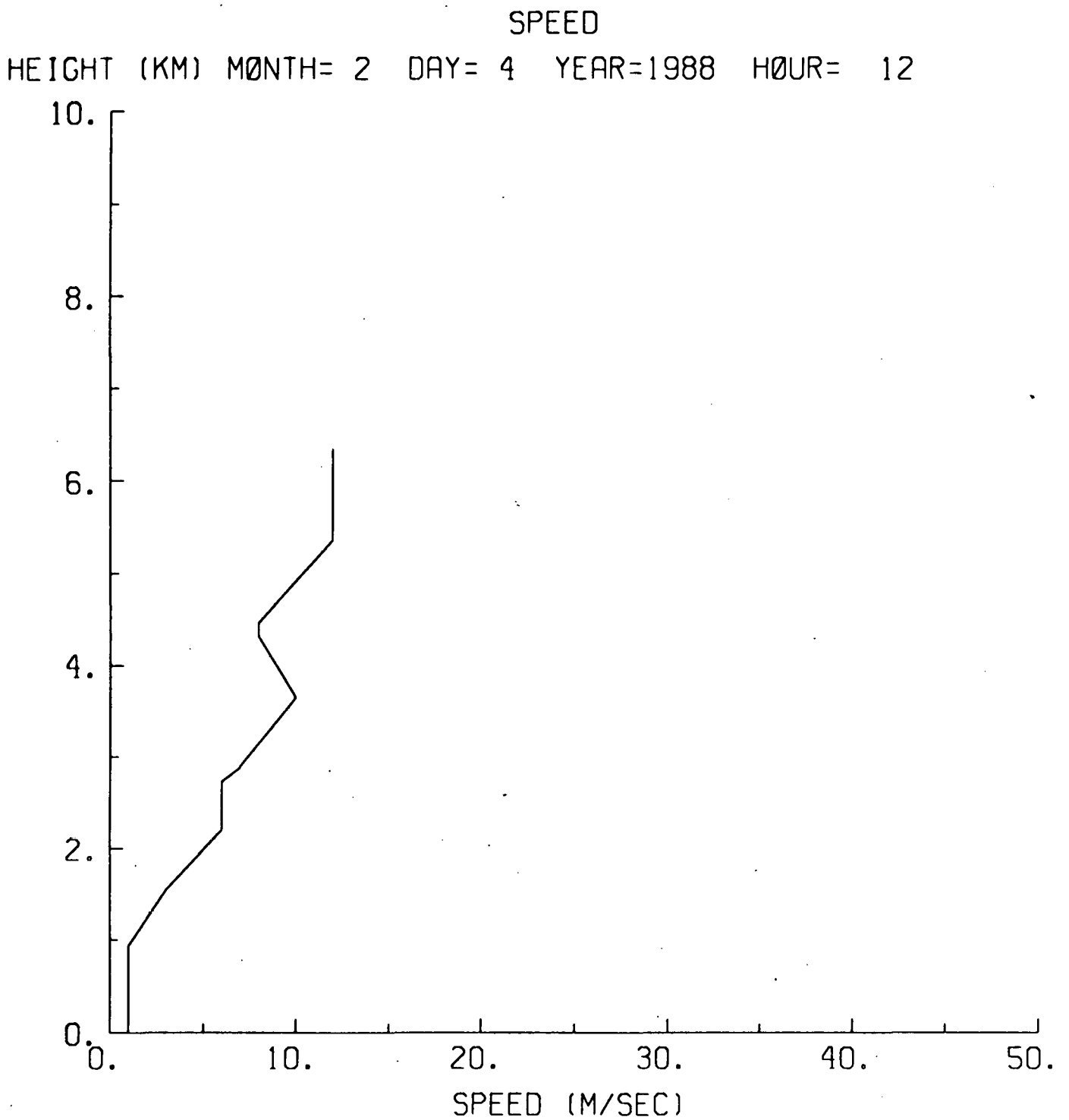

Figure 10: Vertical Profile of Wind Speed above the Mexico City Airport on February 4, 1988 at 6 am local time

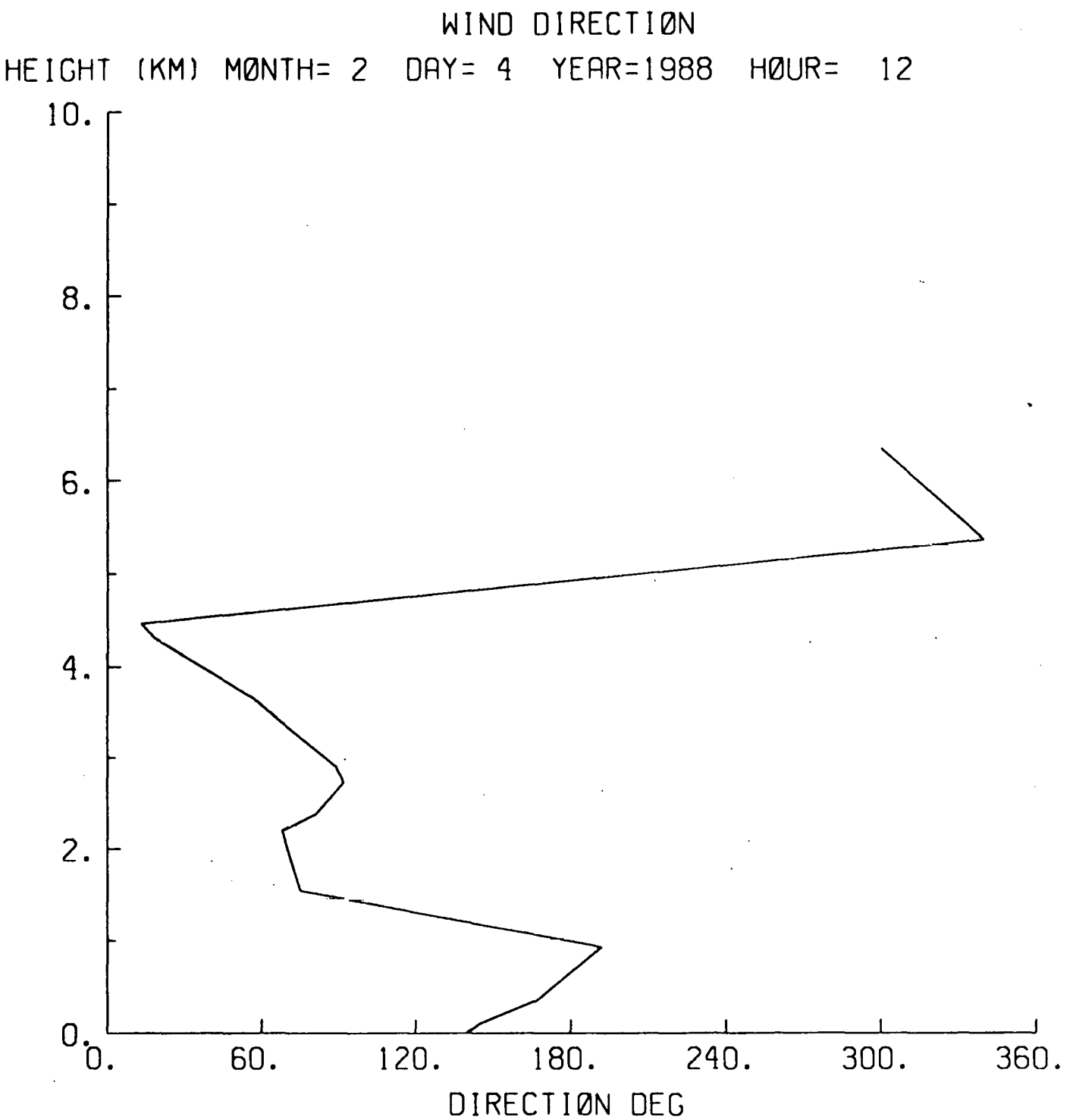

Figure 11: Vertical Profile of Wind Direction above the Mexico City Airport on February 4, 1988 at 6 am local time

MAJOR TOPOGRAPHIC INPUTS TO HOTMAC

- GROUND AND CANOPY ALBEDOS
- FRACTIONAL TREE COVERAGE
- CANOPY PARAMETERS
- TERRAIN AND GRID PARAMETERS
  - UTM COORDINATES - LATITUDE/LONGITUDE
- SOIL CONDUCTIVITY AND DENSITY
- WATER COVERAGE
- TERRAIN ELEVATIONS

Figure 12: Terrain Related Inputs to HOTMAC

Figure 13: Estimated Streamlines for Flow Surrounding the Great Salt Lake during Nighttime (4 am mst) in the Summer

number 4 in the lower central portion of figure 13.

The terrain is quite complex; the potential release point is in the center of a deep valley which drains toward the Great Salt Lake. To the east over a low pass lies another valley with another large lake, Utah Lake. Beyond Utah Lake is the massive Wasatch Range of mountains. To the west of the potential release point lies another valley which drains into the Great Salt Lake. The mountains and the large bodies of water combine to produce strong, terrain-driven, flows. During the night the cold air drains down the valleys towards the warmer waters of the Great Salt Lake. Figure 14 shows an afternoon stream flow analysis where the flows are reversed with warm air rising over the slopes and air from the now relatively colder lake waters spreading up the valleys.

One objective of the model analysis was to define the level of detail needed to represent the major features of the flow. We were interested in carrying out rapid analyses and yet achieving good results. A fine grid would allow a more detailed representation and permit a better description of the temperature gradients which drive the land-sea and mountain-valley wind systems. However, the computer time requirements go up rapidly as grid cell is diminished for the same domain. Since the time step is limited by the time it takes for a disturbance to cross a grid cell, the time step is inversely related to the grid size. Furthermore, the time to carry out a calculation is proportional to the number of grid cells. Consequently, the calculation time is inversely proportional to the cube of the horizontal grid cell size.

The domain is also of critical importance. In the Utah example there is frequently drainage from the Utah Lake valley into the valley of interest, which means that the slopes which influence both valleys must be included in the simulation.

To examine the effect of various grid sizes we carried out simulations with a variety of grid sizes for both the typical nighttime and afternoon conditions. Figure 15 displays a near midnight simulation with a 21 by 21 by 9 grid system, in which the last number is the number of levels in the vertical. Figure 16 displays the same situation with a 16 by 16 by 9 grid system while Figure 17 shows a 11 by 11 by 9 simulation. In each case the direction of the arrows represents the wind direction while the length of the arrow represents the wind speed. The contours are terrain contours. The domain represents the lower central portion of figure 13, with the Great Salt Lake at the top and Utah Lake in the lower right hand side of the domain. It is clear that 21 by 21 and 16 by 16 simulations provide reasonable representations of the general flow field, but that the 11 by 11 simulations were inadequate.

Figures 18 and 19 depict the afternoon simulations for the 21 by 21 by 9 and the 16 by 16 by 9 representations. The two figures differ by very little, but neither one represents the lake breeze effects which should be present. However, figure 20 which is a 16 by 16 by 16 simulation provides a much better depiction. Simulations with more horizontal grid cells failed to improve the simulations significantly. In these simulations the temperature profile was initially near

Figure 14: Estimated Streamlines for Flow Surrounding the Great Salt Lake during Daytime (2 pm mst) in the Summer

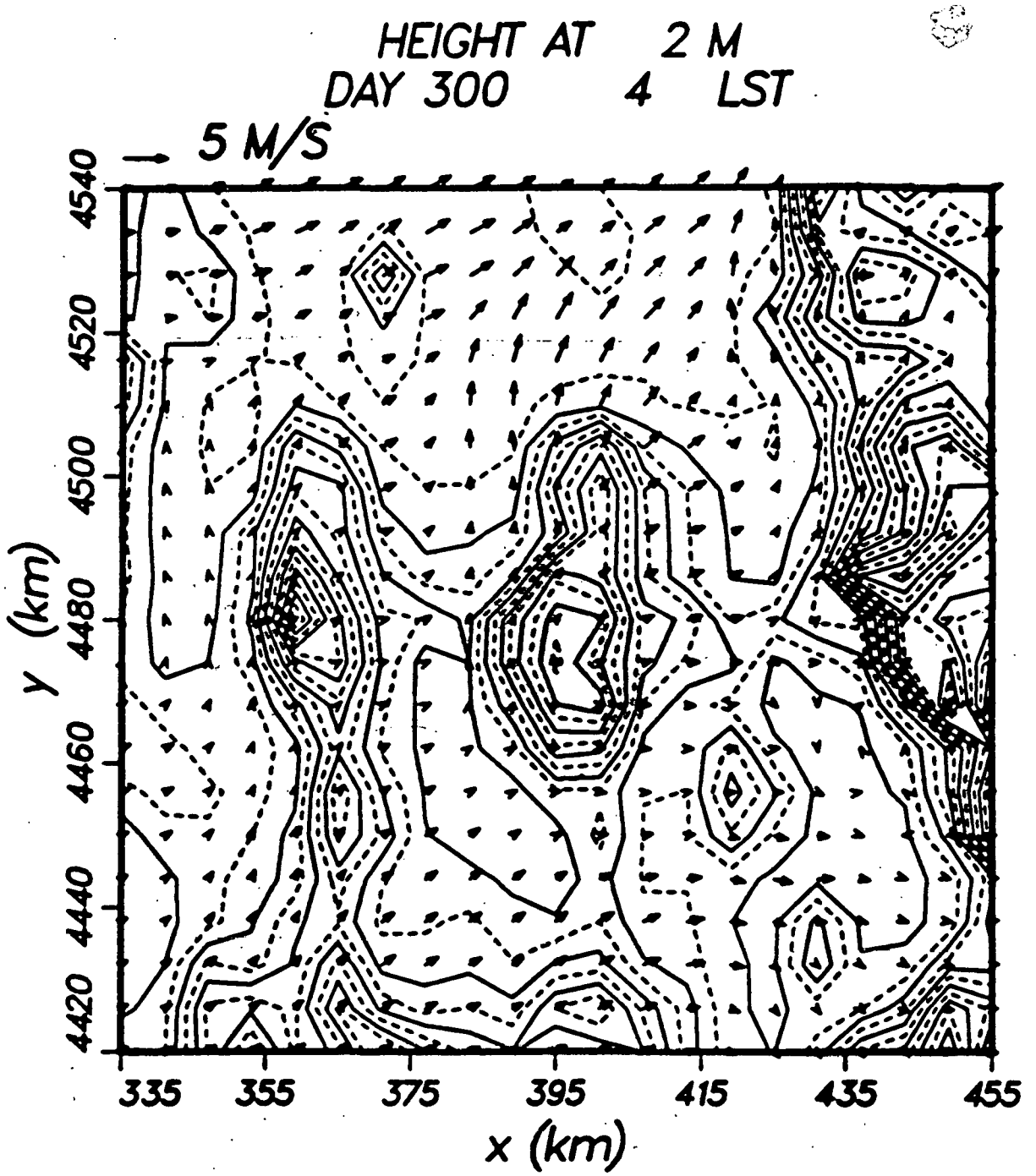

Figure 15: Modeled Wind Vector for Flow Surrounding Tooele Valley with a 21 x 21 x 9 array of cells during Nighttime

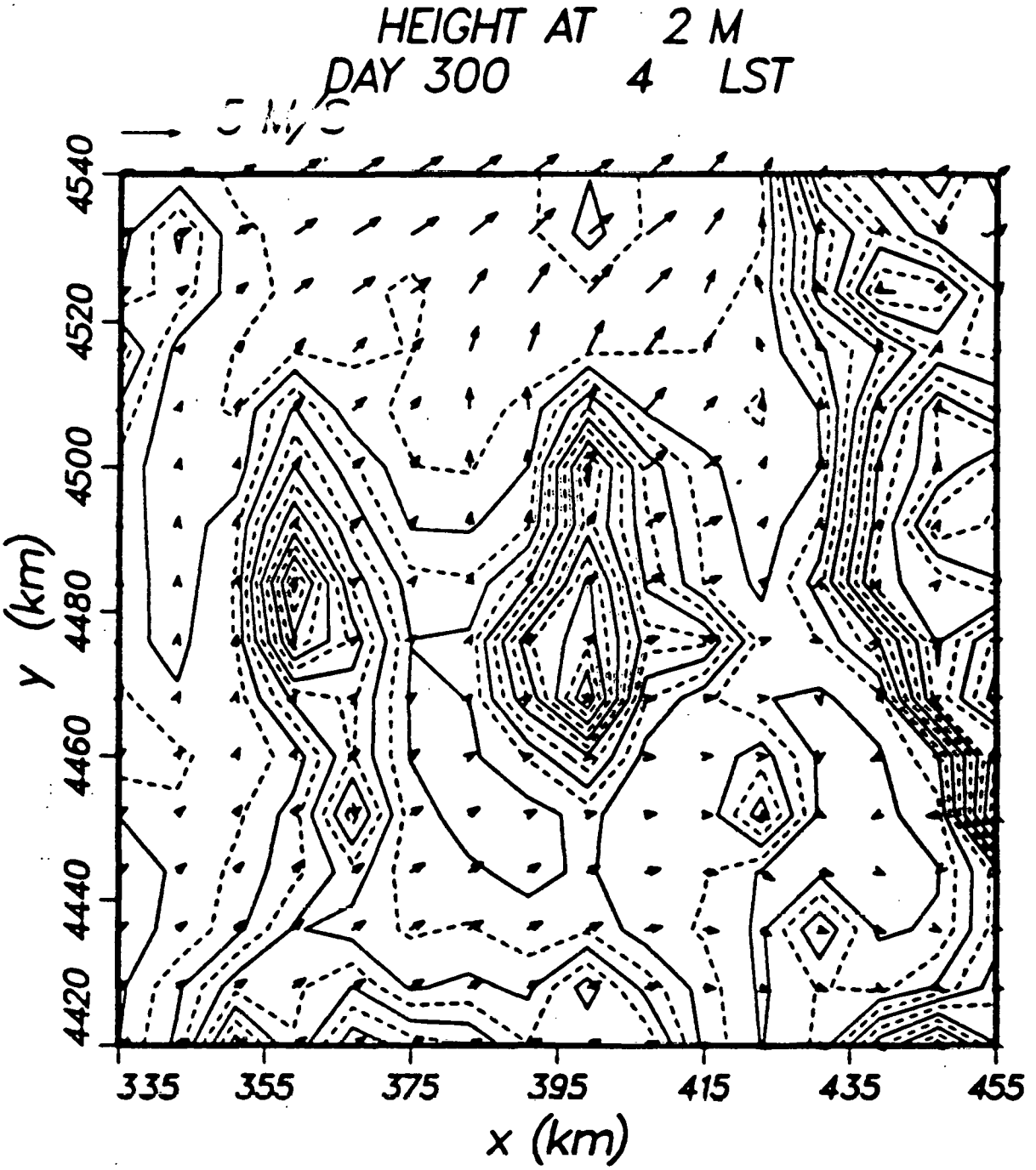

Figure 16: Modeled Wind Vector for Flow Surrounding Tooele Valley with a 16 x 16 x 9 array of cells during Nighttime

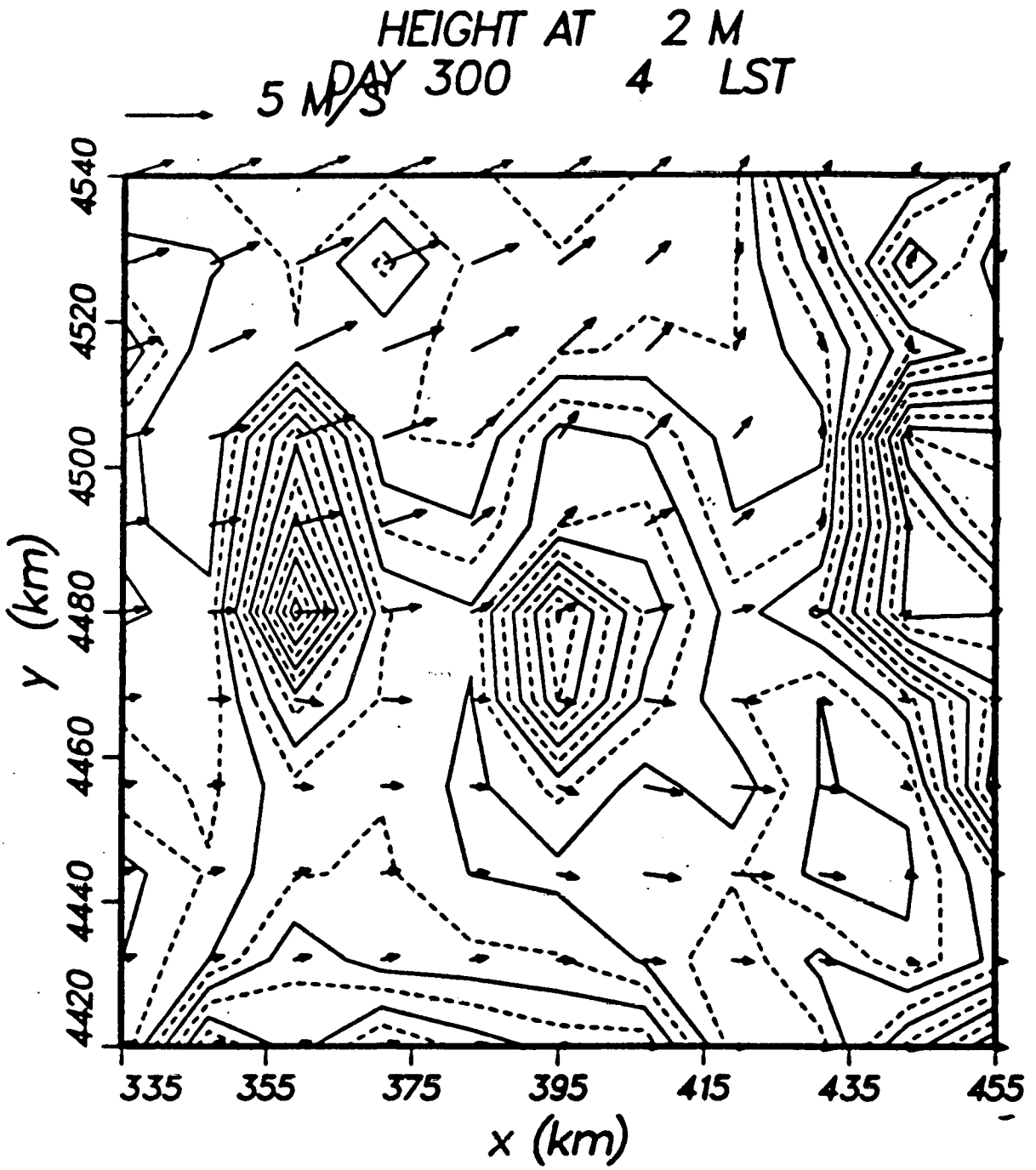

Figure 17: Modeled Wind Vector for Flow Surrounding Tooele Valley with a 11 x 11 x 9 array of cells during Nighttime

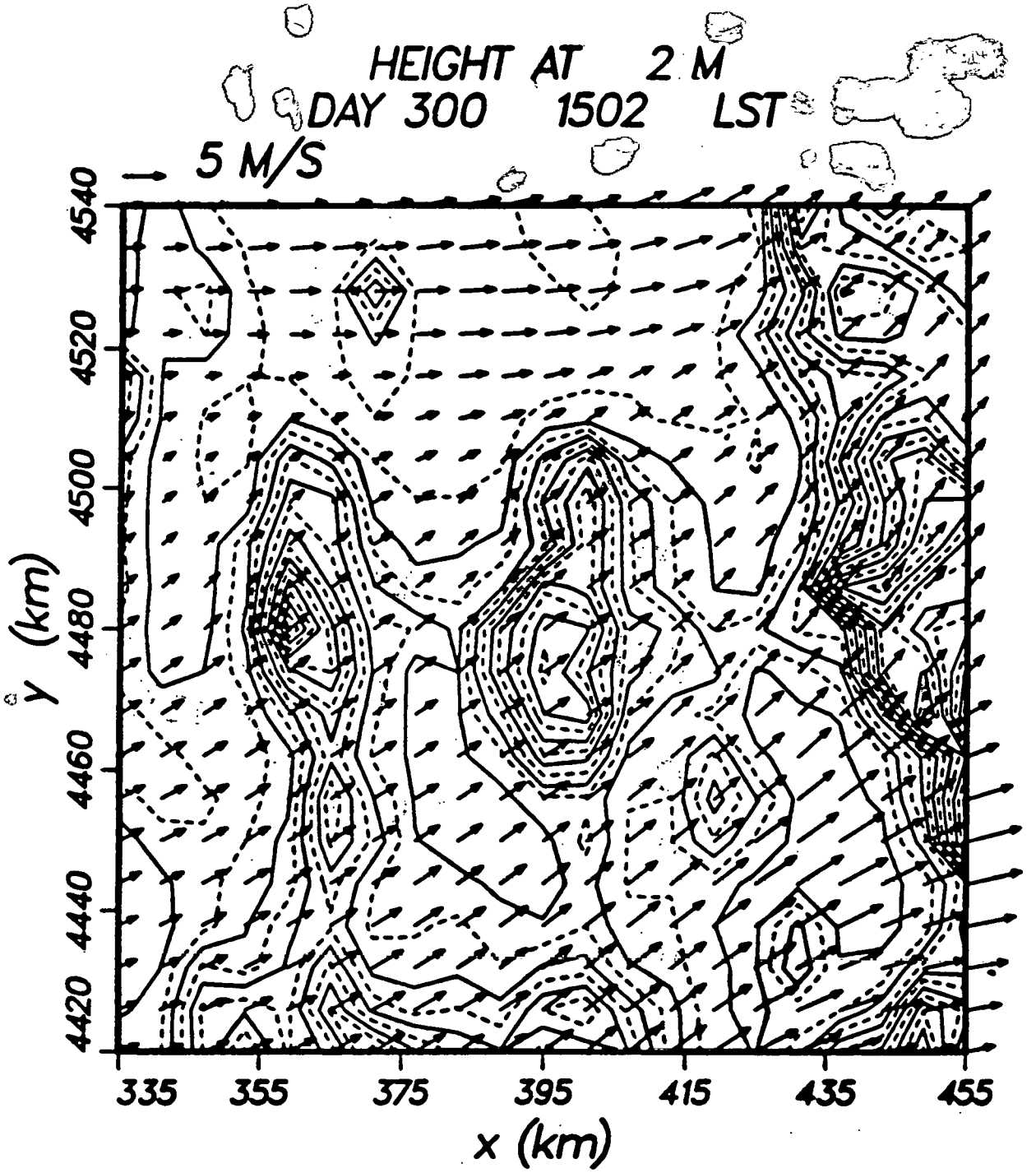

Figure 18: Modeled Wind Vector for Flow Surrounding Tooele Valley with a 21 x 21 x 9 array of cells during the Afternoon

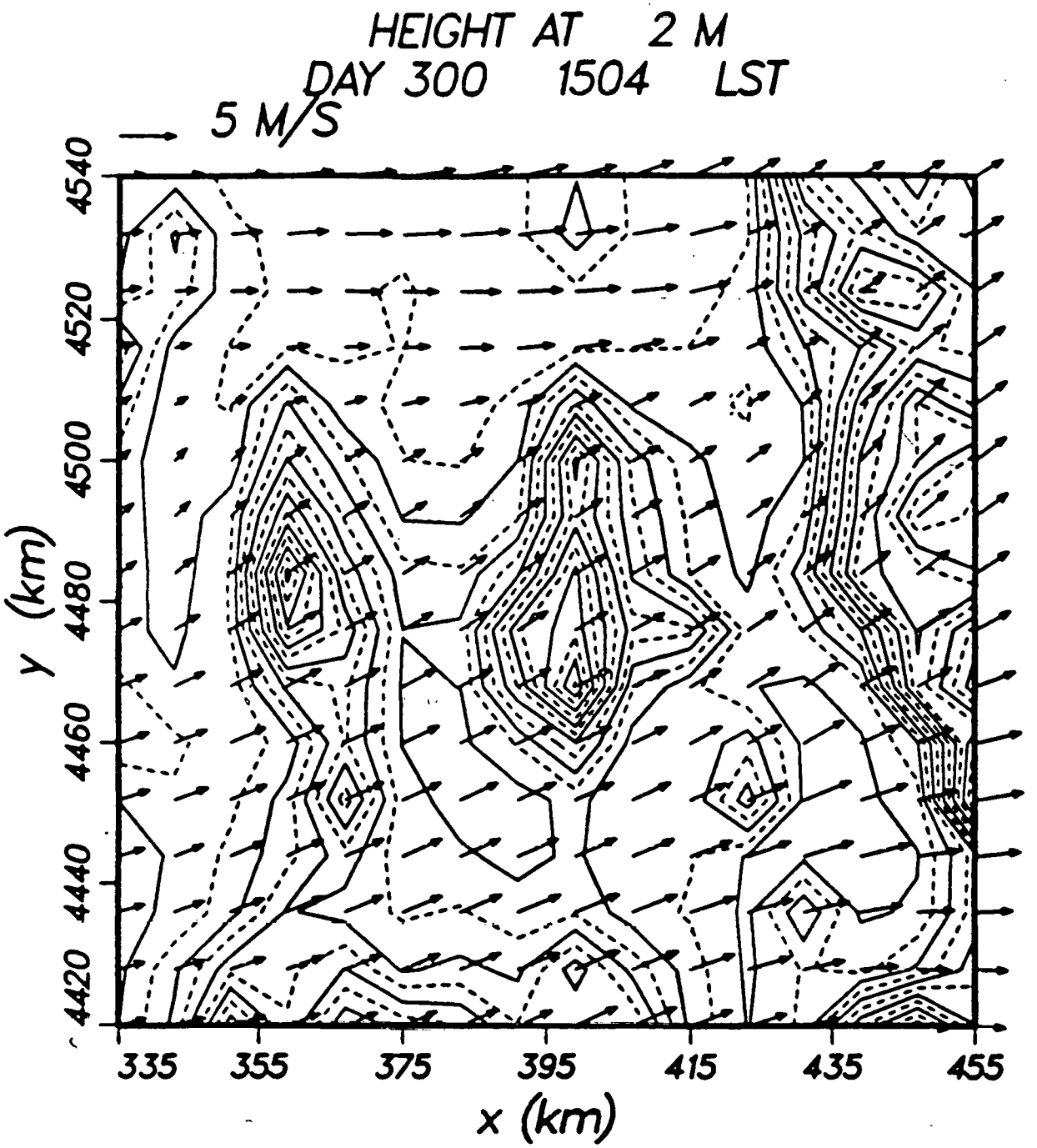

Figure 19: Modeled Wind Vector for Flow Surrounding Tooele Valley with a 16 x 16 x 9 array of cells during the Afternoon

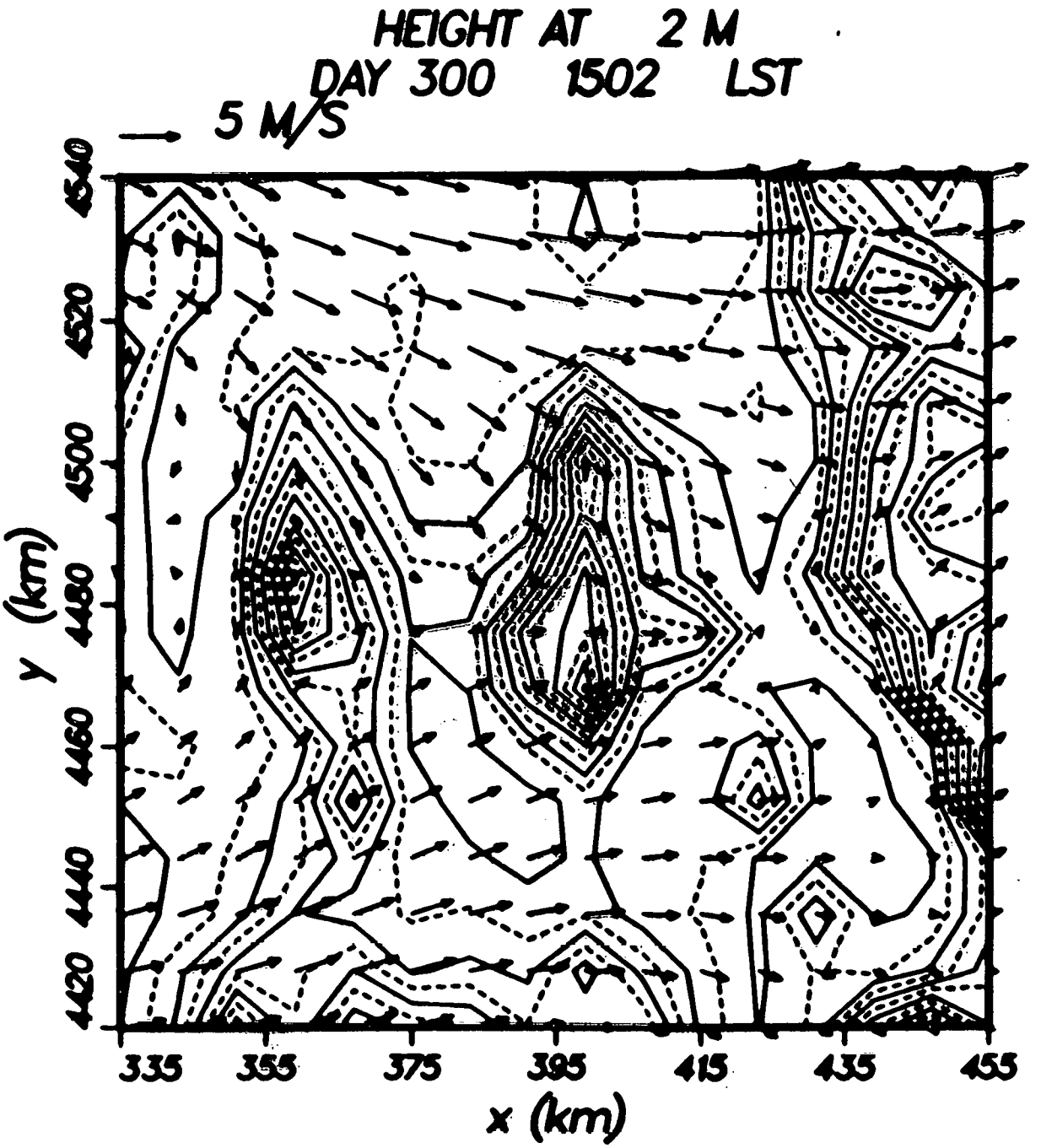

Figure 20: Modeled Wind Vector for Flow Surrounding Tooele Valley with a 16 x 16 x 16 array of cells during the Afternoon

neutral.

Figures 21 and 22 show early morning and late afternoon simulations with more realistic temperature profiles. In these cases, which are 16 by 16 by 16 representations the flows compare well with streamline analyses.

Another question which arose is what class of machine is required to produce reasonable simulations. Figure 23 displays a simulation carried out with a 32 bit add-in board in an IBM-AT while figure 24 displays the same simulation performed with a Cray super computer. The simulations are quite similar except for a small area near the western boundary of the simulation.

Comparison with measurements indicated that the inter valley flow was not very well represented. The simulations were improved by including more terrain to the east so that the mountain valleys which drain into the Utah Lake basin were included. Figures 25 and 26 show the morning and evening simulations for these cases. While the larger scale flow can be well represented with relatively few grid points, some small scale features will be lost. For example, in figure 25 one can see a low ridge which extends into the valley at 385 east and 4480 north. Measurements show that a small drainage flow from this ridge tends to deflect the valley flow to the eastern side of the valley. The simulations with this grid spacing fail to show this flow.

A better compromise between needed detail, the requirement to cover a large enough area to encompass the important flow features, and limited computer resources, is the use of a nested grid (Yamada and Bunker, 1989). In this technique a small area can be representative in great detail while maintaining sufficient overall coverage. Figure 27 shows an example of a nested grid application. Without the larger outer grid the flow direction on the southern boundary of the inner grid would be much different, because there would be no information about the ridge to the south of the boundary.

We have found that: (1) HOTMAC provides reasonable results, (2) requires less extensive inputs than to diagnostic models, (3) provides turbulence fields appropriate to advanced dispersion models, and (4) can be used on smaller computers for a variety of air quality and meteorology studies.

4 The Particle Transport Code RAPTAD

4.1 Model formulation

RAPTAD is a Monte Carlo random particle statistical diffusion code, developed by Ted Yamada (Yamada and Bunker,1989). Pseudo-particles are transported with instantaneous velocities that include the mean wind field and the turbulence velocities. The turbulence velocity is generated randomly consistent with the standard deviation of the wind at the particle location. The location of each pseudo-particle represents the center of mass of a concentration distribution for each puff. The total concentration at any point is obtained by adding

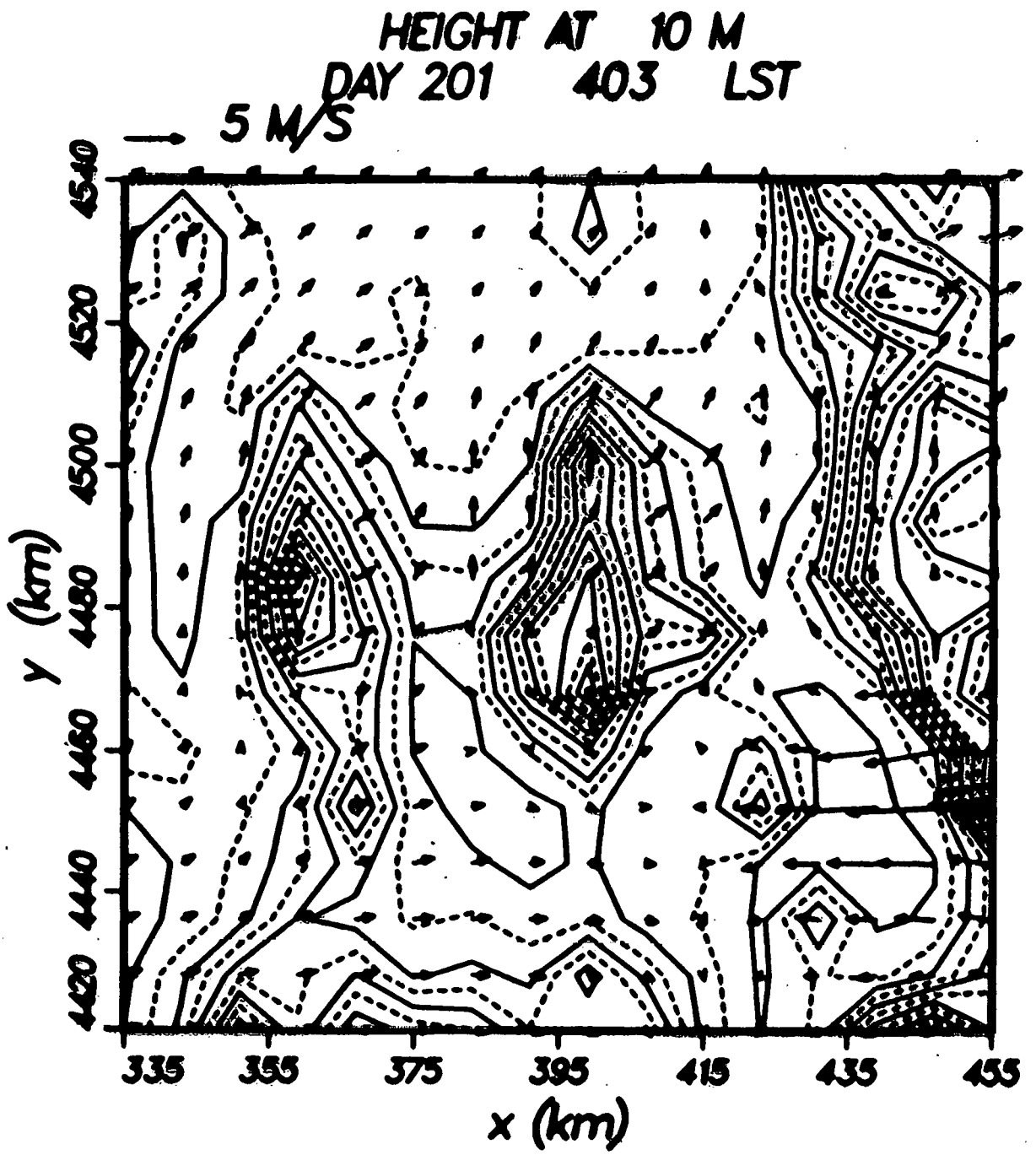

Figure 21: Modeled Wind Vector for Flow Surrounding Tooele Valley with a 16 x 16 x 16 array of cells during Nighttime with realistic temperatures

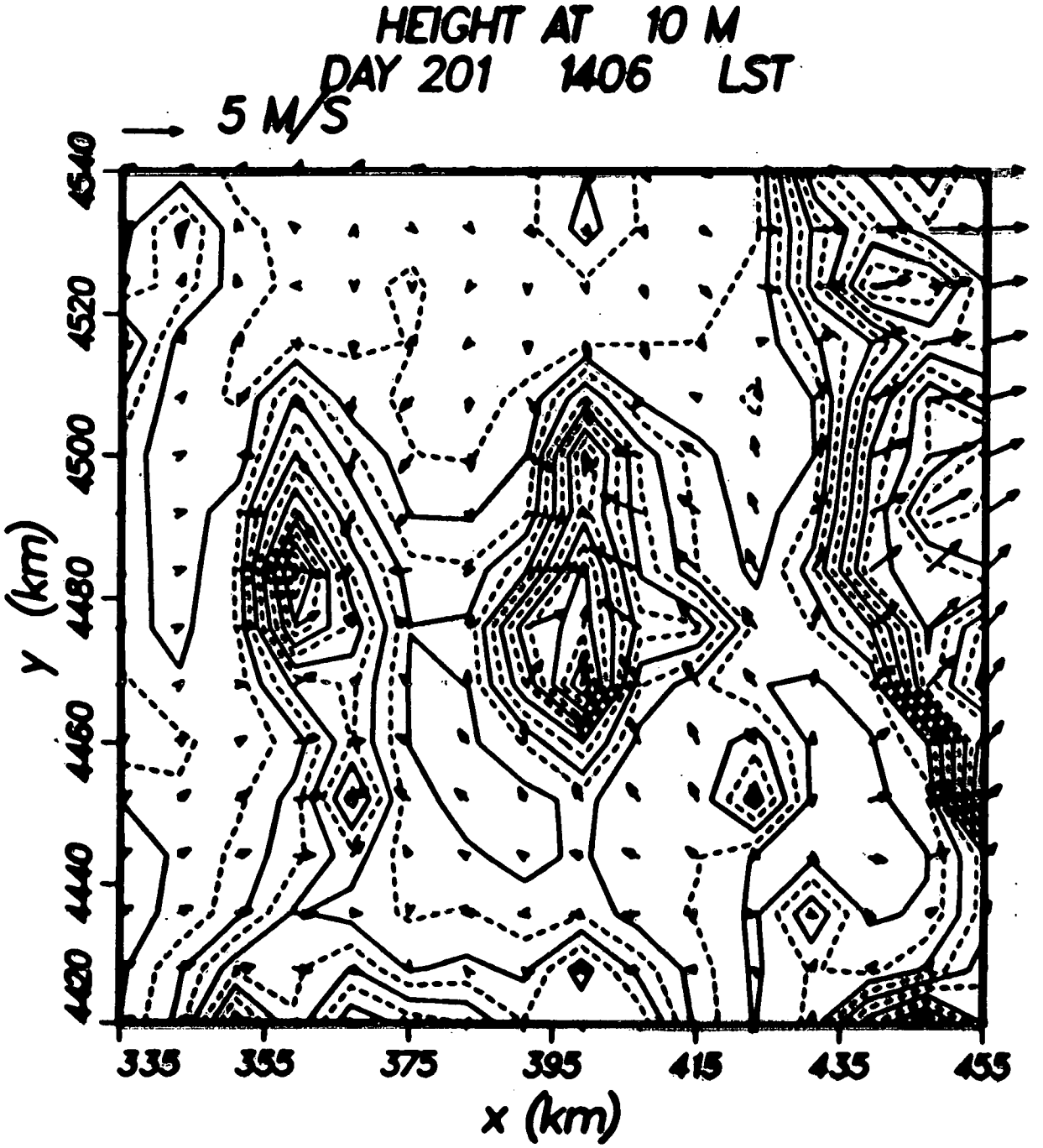

Figure 22: Modeled Wind Vector for Flow Surrounding Tooele Valley with a 16 x 16 x 16 array of cells during Afternoon with realistic temperatures

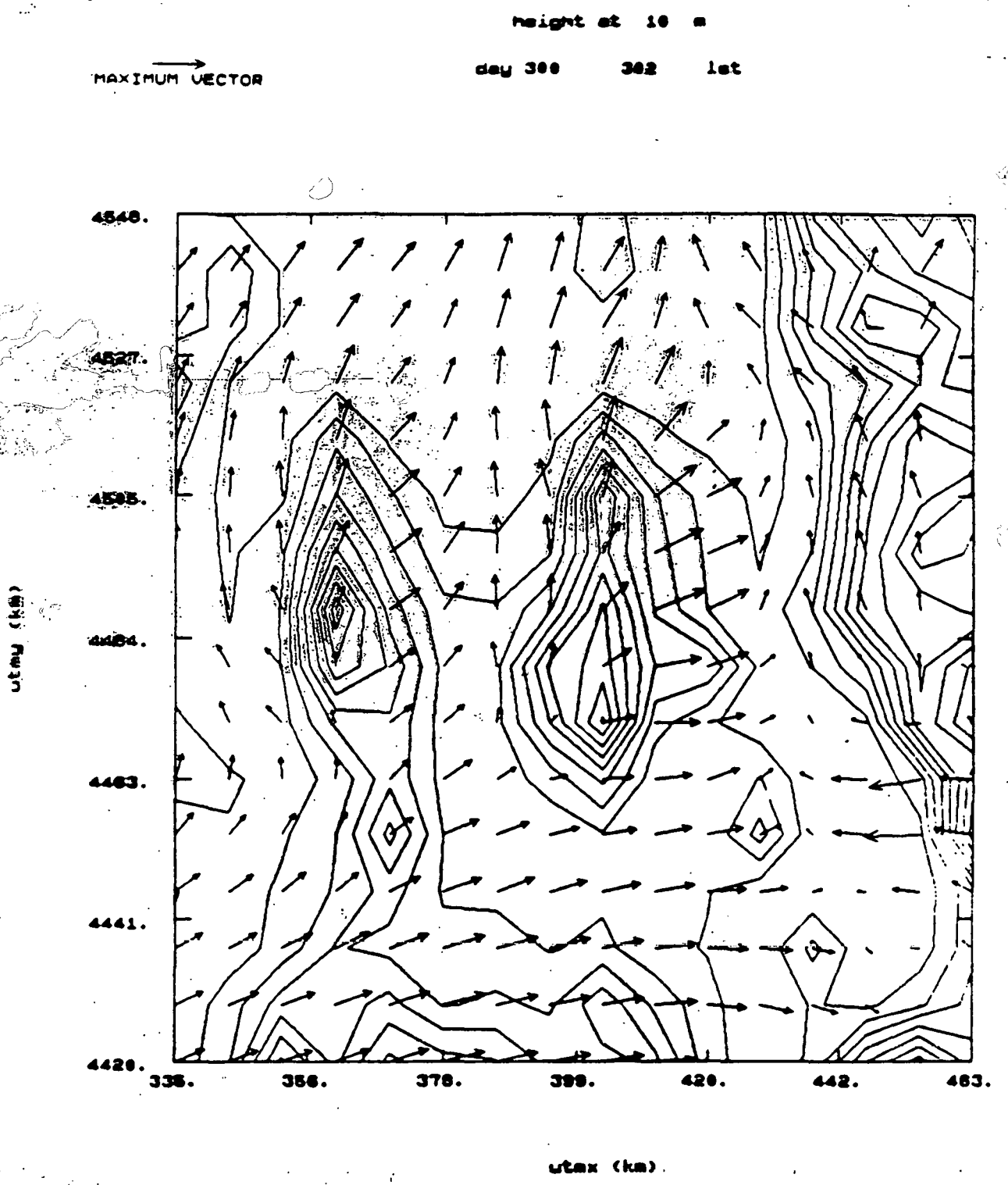

Figure 23: Modeled Wind Vector for Flow Surrounding Tooele Valley with a 16 x 16 x 16 array of cells during Nighttime with a microcomputer

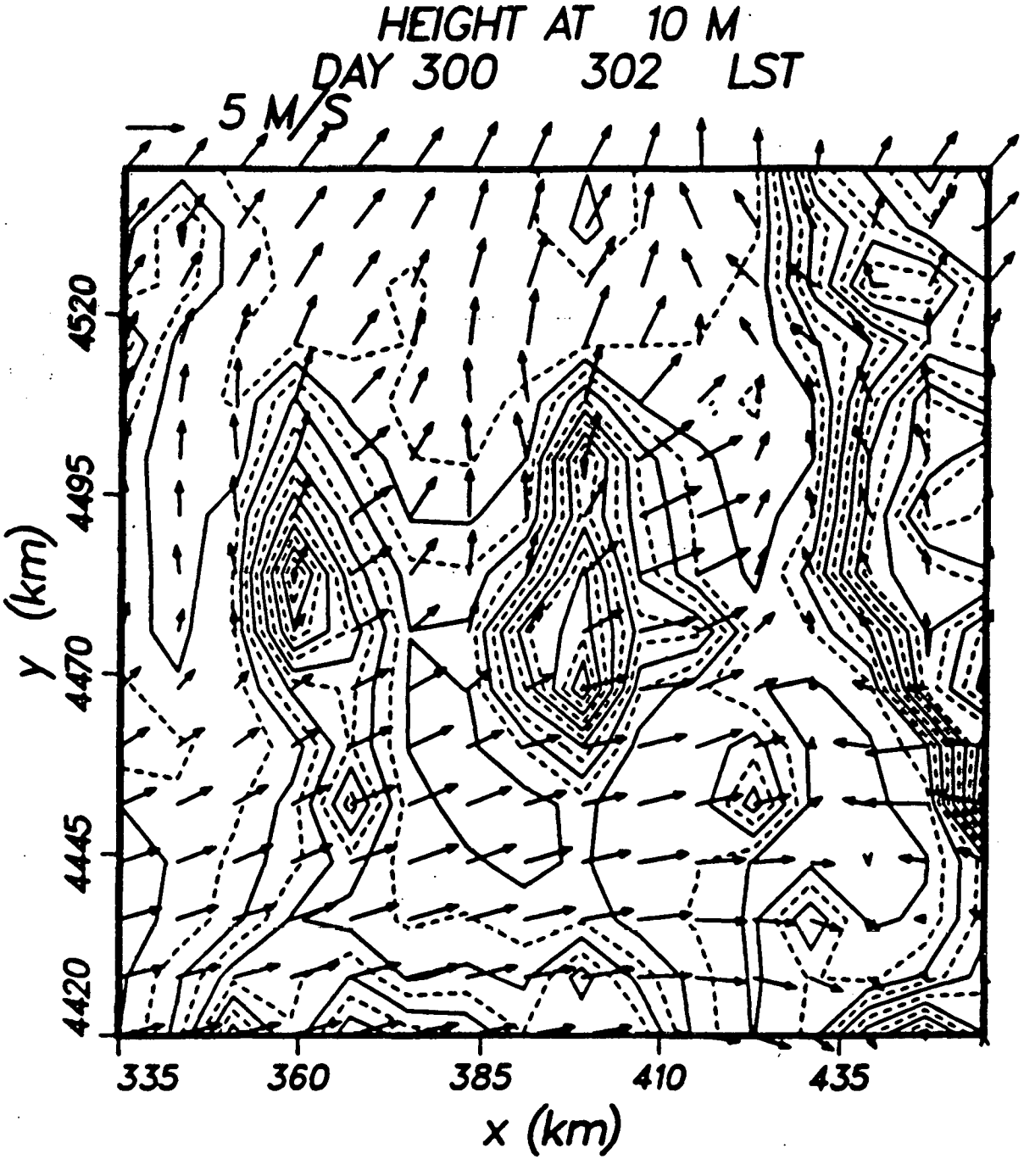

Figure 24: Modeled Wind Vector for Flow Surrounding Tooele Valley with a 16 x 16 x 16 array of cells during Nighttime with a super computer

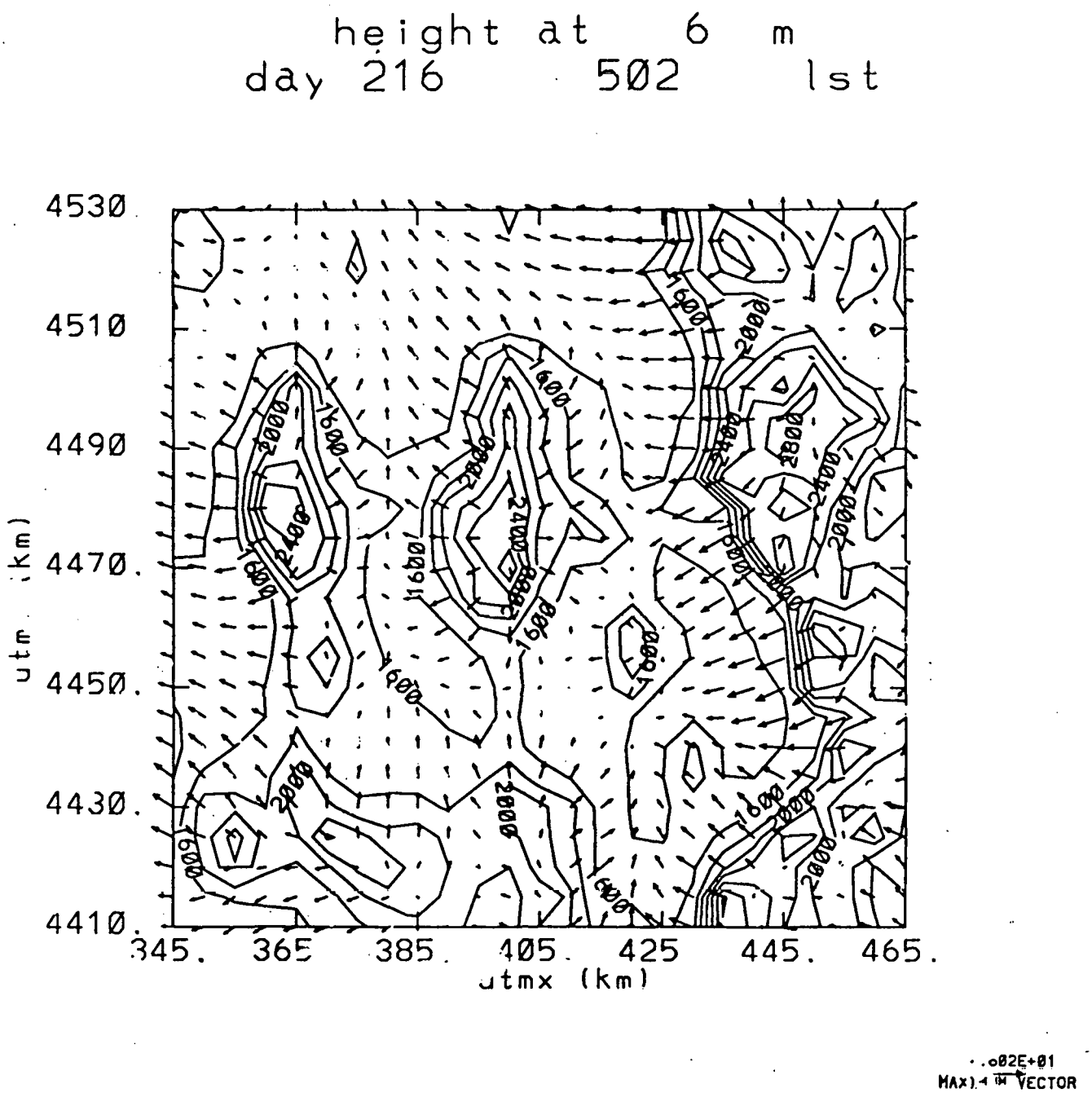

Figure 25: Modeled Wind Vector for Flow Surrounding Toocle Valley with a 25 x 25 x 16 array of cells during Nighttime with an increased domain

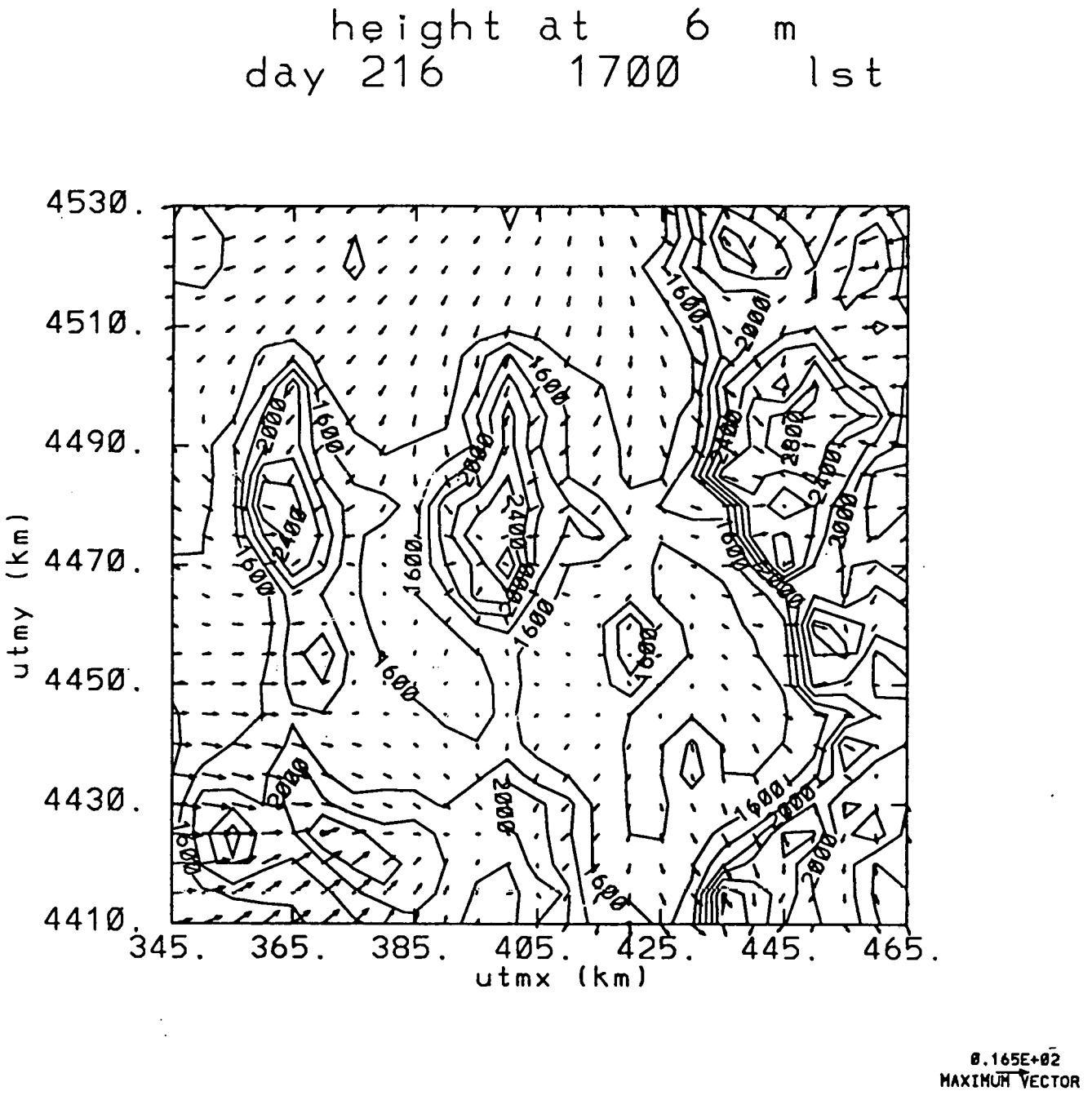

Figure 26: Modeled Wind Vector for Flow Surrounding Tooele Valley with a 25 x 25 x 16 array of cells during Afternoon with an increased domain

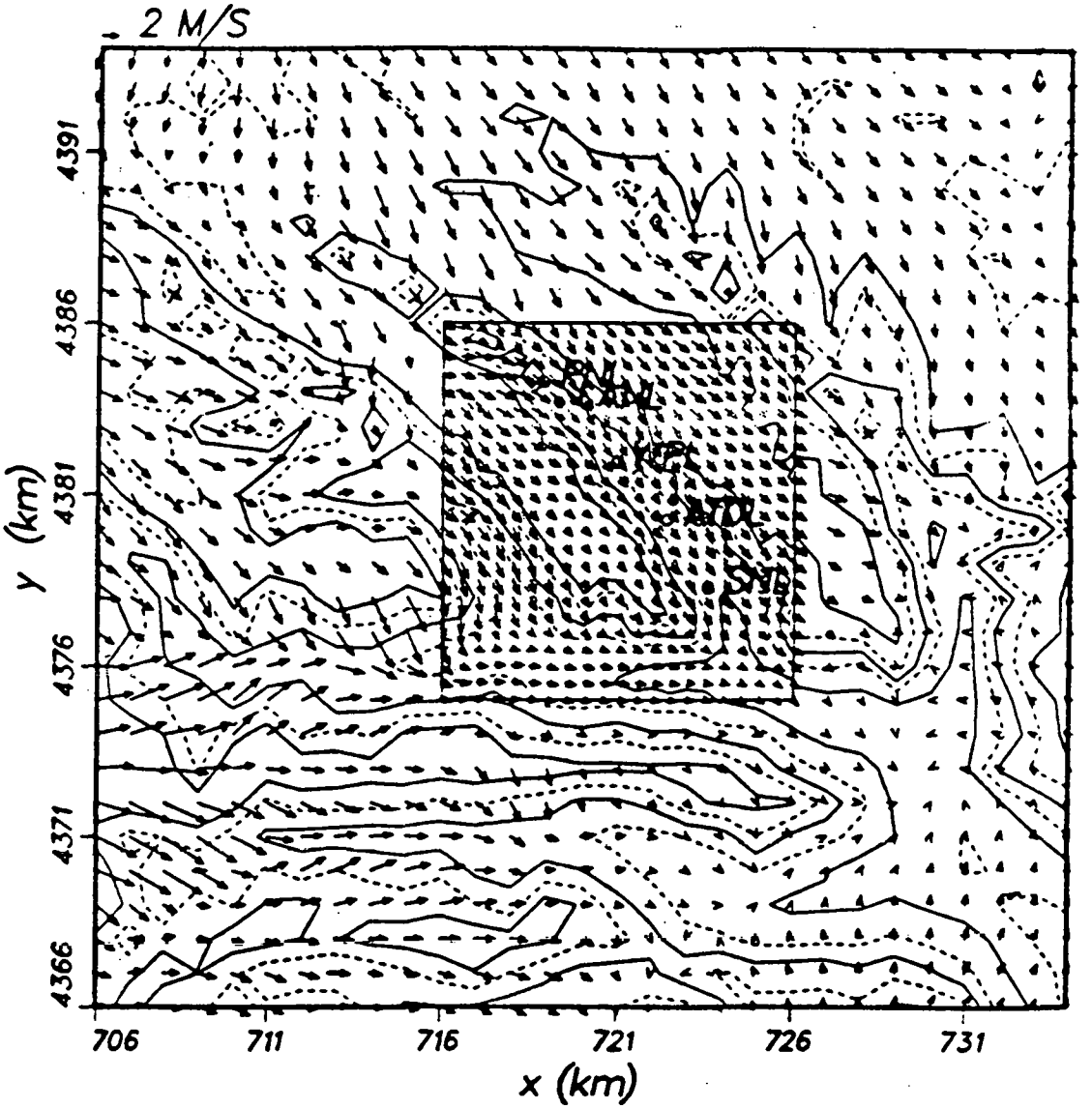

Figure 27: Modeled Wind Vector for a Colorado Canyon with a nested grid at 5 am at a height of 14 meters above the ground

the concentration contributions of each puff at that point (a kernel method).

Other particle transport codes produce concentrations by counting particles within a sampling volume. The computed concentration level could vary considerably depending upon the size of the sampling volume and number of particles used in the computation. For example, if the sampling volume is very small, the concentration distribution becomes excessively variable in space. On the other hand, if the sampling volume is too large, the concentration distribution will be over smoothed. The kernel method avoids this difficulty and provides smooth concentration distributions with relatively few particles.

The first step is to calculate the positions and turbulence history of a group of pseudo-particles that represent the emissions from a release. Locations of particles are computed from:

$$x_i(t + \Delta t) = x_i(t) + U_{pi}\Delta t \tag{17}$$

where

$$U_{pi} = U_i + u_i \tag{18}$$

$$u_i(t + \Delta t) = a u_i(t) + b\sigma_{u_i}\zeta + \delta_{i3}(1 - a)t_{Lx_i}\frac{\partial}{\partial x_i}(\sigma_{u_i}{}^2) \tag{19}$$

$$a = \exp\left(-\frac{\Delta t}{t_{Lx_i}}\right) \tag{20}$$

and

$$b = (1 - a^2)^{1/2} \tag{21}$$

In the above expressions U_{pi} is the particle velocity in the x_i direction, U_i is the mean velocity, u_i is the turbulence velocity, ζ is a random number from a Gaussian distribution with zero mean and unit variance, t_{Lxi} is the Lagrangian integral time scale for the velocity u_i, σ_{ui} is the variance of the velocity fluctuation u_i, and δ_{i3} is the Dirac delta. The last term on the right hand side of equation 19 was introduced by Legg and Raupach (Legg and Raupach, 1982) to prevent the accumulation of particles in low-energy areas. The mean velocity U_i and vertical velocity variance σ_i are obtained from the output of HOTMAC.

The Monte Carlo kernel method requires that a functional form for the distribution kernel be chosen and that parameters that describe the width, breadth, and depth of the distribution be calculated. Various functional forms can be assumed to express the concentration distribution in the puff. One of the simplest ways is to assume a Gaussian distribution where variances are determined as the time integration of the velocity variances encountered over the history of the puff. The concentration level at a given time and space is determined as the sum of the concentrations each puff contributes. The concentration χ at

(X, Y, Z) is estimated by using the following expression:

$$\chi(X,Y,Z) = \frac{Q\Delta t}{(2\pi)^{3/2}} \sum_{k=1}^{N} \frac{1}{\sigma_{x_k}\sigma_{y_k}\sigma_{z_k}} \exp\left(-\frac{1}{2}\frac{(X_k - X)^2}{\sigma_{x_k}{}^2}\right) \bullet \exp\left(-\frac{1}{2}\frac{(y_k - Y)^2}{\sigma_{y_k}{}^2}\right) \bullet \left\{\exp\left(-\frac{1}{2}\frac{(z_k - Z)^2}{\sigma_{z_k}{}^2}\right) + \exp\left(-\frac{1}{2}\frac{(z_k + Z - 2z_g)^2}{\sigma_{z_k}{}^2}\right)\right\} \tag{22}$$

where (x_k, y_k, z_k) is the location of the k^{th} particle; σ_{xk}, σ_{yk}, and σ_{zk} are standard deviations of a Gaussian distribution; and z_g is the ground elevation. The variances are estimated based on Taylor's homogeneous diffusion theory (Taylor, 1921). For example σ_y is obtained from

$$\sigma_y{}^2 = 2\sigma_v{}^2 \int_o^t \int_o^\zeta R(\zeta) d\zeta dt = 2\sigma_v{}^2 t_{Ly} \left(t + t_{Ly} \exp\left(-\frac{t}{t_{Ly}}\right) - t_{Ly}\right) \tag{23}$$

where a correlation function $R(\zeta) = \exp\left(\frac{-\zeta}{t_{Ly}}\right)$ is used. Equation 23 is approximated by

$$\sigma_y = \sigma_v t \qquad t \leq 2t_{Ly} \tag{24}$$

and

$$\sigma_y{}^2 = 2t_{Ly}\sigma_v{}^2 t \qquad t > 2t_{Ly} \tag{25}$$

Although the turbulence field is not normally homogeneous, we assume the theory can be applicable over a short time period, such as an integration time step. Therefore,

$$\sigma_y(t + \Delta t) = \sigma_y(t) + \sigma_v \Delta t \qquad t \leq 2t_{Ly} \tag{26}$$

and

$$\sigma_y{}^2(t + \Delta t) = \sigma_y{}^2(t) + 2t_{Ly}\sigma_v{}^2 \Delta t \qquad t > 2t_{Ly} \tag{27}$$

are used. Similar relations are used for the x and z directions. The standard deviations σ_u, σ_v, and σ_w at each particle location are obtained by interpolating grid values of a computation grid volume in which a particle is located.

Figure 28 depicts a situation in which the system can be used and it illustrates the problems with other systems. The figure depicts a nighttime circum-

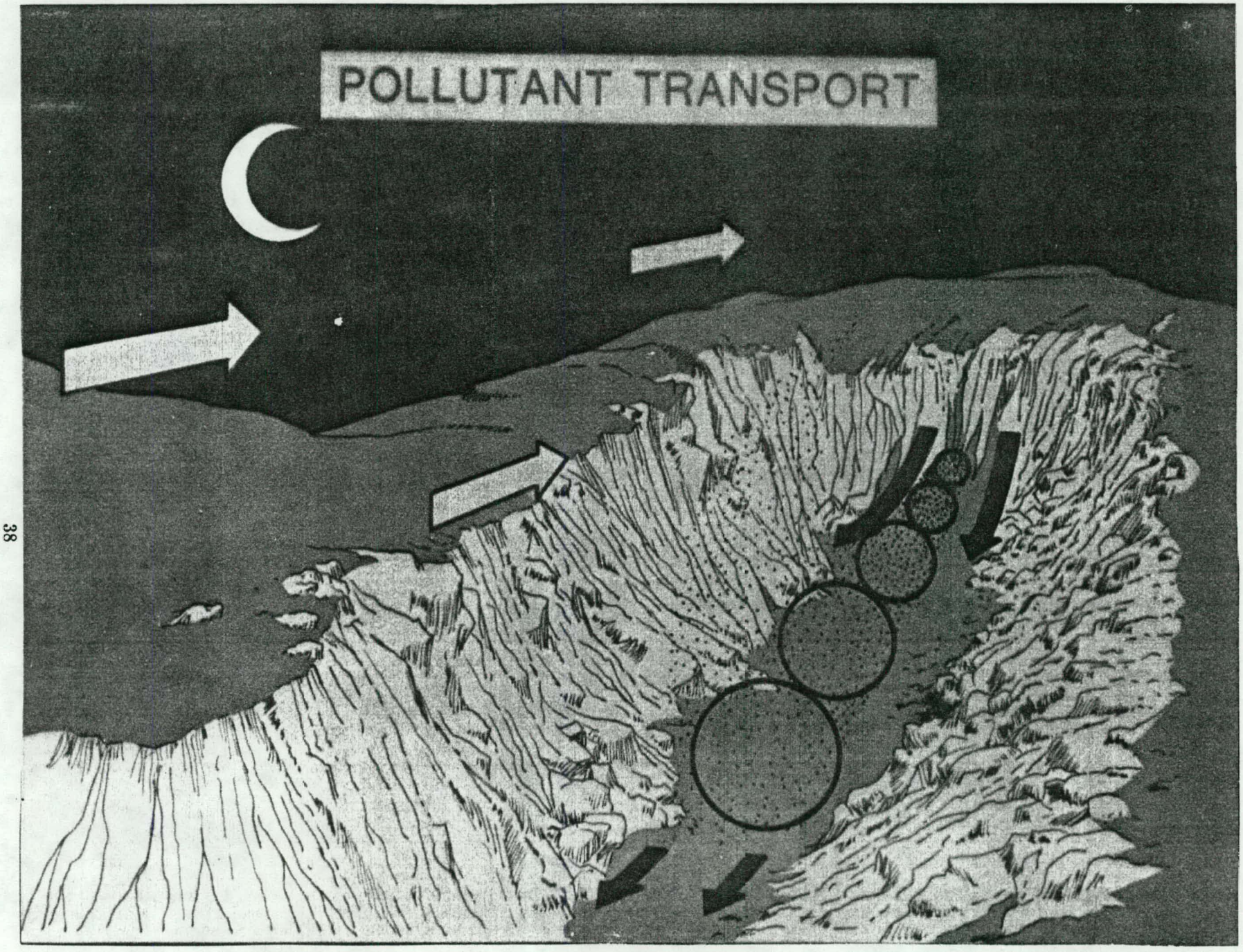

Figure 28: Illustration of Aspects of Dispersion in Complex Terrain

stance in which a release has been made near the upper end of the canyon. The upper level flow is up canyon while the lower level flow is down canyon. The red dots represent pseudo-particle positions while the circles represent Gaussian puffs as described by Gaussian puff models. At intermediate point in the canyon, some of the material will have diffused upward and reached the up canyon flow and begun drifting back towards the canyon rim. The Gaussian puff model which uses only the mean wind field will not reflect this change in direction for some of the pollutants. Figure 29 shows what various models would be expected to predict for pollutant profiles at an intermediate point. The Gaussian puff with transport defined by the mean wind misses the up canyon flow. The random particle model with fixed cell sizes shows a noisy pattern. The Monte Carlo Kernel method shows a smooth realistic concentration profile.

Figure 30 shows the pseudo-particle positions during a very similar release in a California valley. The release point was near PMCH and most of the material drifted down valley, but a significant portion traveled generally up valley.

4.2 Model usage

Figure 31 summarizes the input required for RAPTAD. The input includes an index which indicates which of the HOTMAC wind fields is to be used. It also includes the duration of the simulation, the time step, and parameters which control the number of particles released. In addition the source location, release starting time, source rate, height, and duration must be specified. The model permits release of a specified number of pseudo-particles every time step or release of pseudo-particles every few time steps. The time step is usually chosen to be on the order of 10 seconds so that a pseudo-particle experiences relatively constant wind and turbulence fields over the distance it travels in a single time step.

We have compared the HOTMAC-RAPTAD simulations to tracer releases in a number of circumstances. As was described in the HOTMAC section the system has been used to describe the behavior of releases from a point southwest of Salt Lake City in Utah.

The simulations included both a nighttime and a daytime experiment. The first experiment examined was conducted on August 3, 1987, with a 1-hour release beginning at 2200 MST. Relatively high tracer concentrations were measured for 7 hours.

The second case examined was a 1-hour release begun at 1000 MST on August 7, 1987. In this case, tracer concentrations were insignificant after 3 hours. The two cases were chosen because they represented extremes in dispersion for low-wind cases. During each of the tracer experiments, sulfur hexafluoride was released at a rate of approximately 50 g/s for 1 hour. One-hour samples were collected at each of approximately 65 sites. Sample sensitivity was approximately 10 ppt. However, SF_6 was found in places and times that could not have been associated with the tracer release. In addition some potential sources

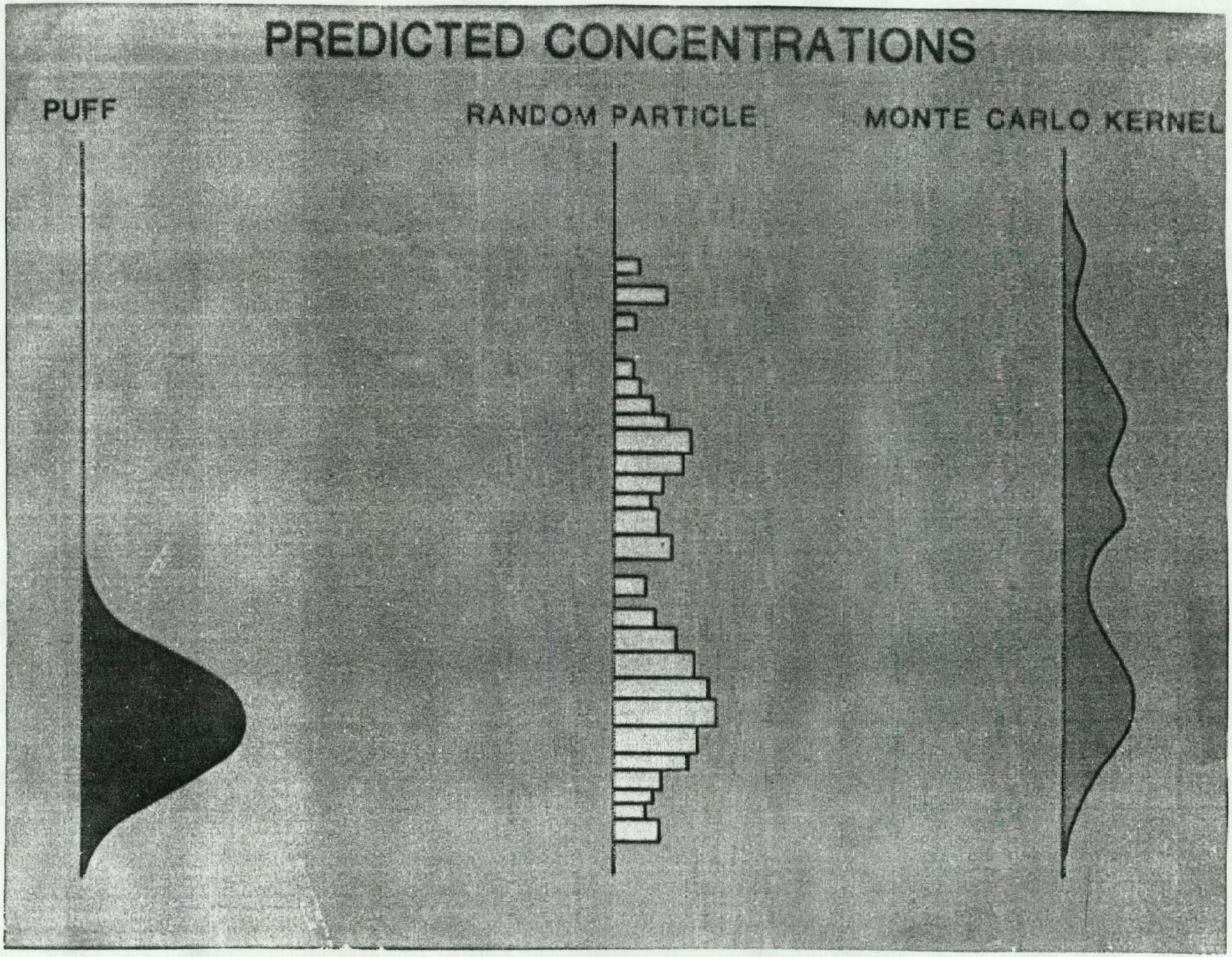

Figure 29: Pollutant Concentration Profiles Produced by Various Models

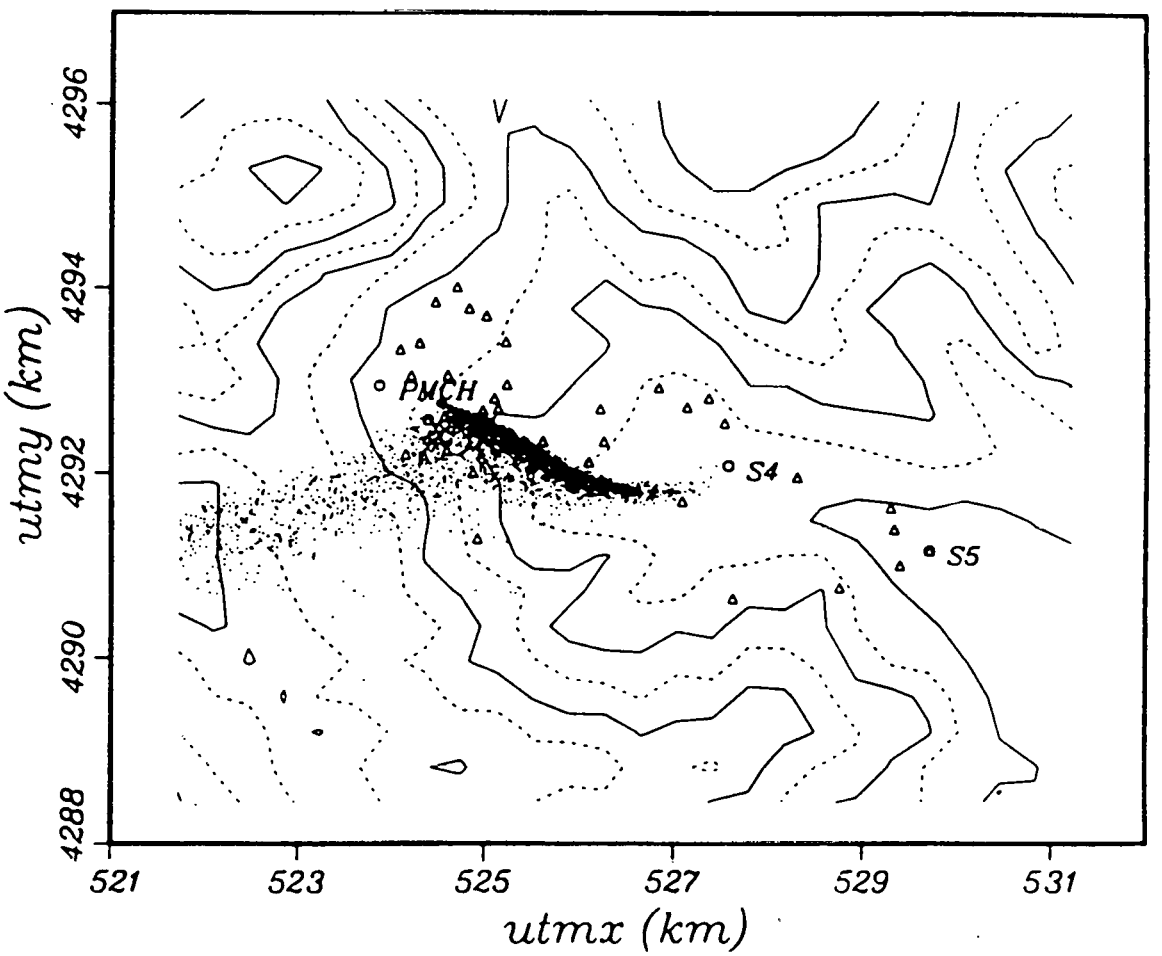

Figure 30: Pseudo-particle Positions during a Release in California

RAPTAD INPUT

- STARTING WIND FIELD
- DURATION
- TIME STEP
- PARAMETERS CONTROLLING NUMBER OF PARTICLES RELEASED
- SOURCE LOCATION (UTM)
- STARTING TIME
- SOURCE SIZE, HEIGHT, AND DURATION

Figure 31: RAPTAD Input

of SF_6-like material were identified. During nighttime conditions these sources could have contributed concentrations of a few hundred ppt, while much lower values would be expected during the daytime. The periods and samplers described in this section were chosen to define the primary areas and times of tracer impacts on the monitoring network.

The tracer behavior was much different in the two cases. During the nighttime release high concentrations, defined as 700 to 9000 ppt, persisted for several hours. For the daytime release, the concentrations were much lower, 80 to 350 ppt, and were quickly diminished to levels comparable to those produced by other sources. Tethersonde wind profiles suggested that the wind above the site was changing rapidly at about the time of the release. After the release the wind settled down to southeast to south for the lowest 50 meters as opposed to a southwest to west direction before the release. Figure 32 reports a representative tethersonde profile after the release. Tethersondes represent very short-term measurements, so that the differences could relate to fluctuations in winds rather than in trends for the mean wind. Above 200 meters the wind was from the north. The low-level winds as shown in figure 33 are 1-hour-averaged values for 0100 to 0200 MST and display a combination of nocturnal drainage flow-level and a land breeze near Great Salt Lake. The simulations were initialized with a 0.2 m/s wind from the west at 1800 MST. At 2200 hours after the temperature structure had developed, the model was reinitialized with a wind of 3 m/s from 160 degrees. The initialization is accomplished by comparing the winds at the measurement site at 10 meters above the ground and adding a system-wide wind component sufficient to bring the winds at the measurement site to the desired values. The added wind is uniform in the vertical direction except near the surface where a log plus linear profile is used in accordance with similarity theory. The horizontal variation of the added wind is obtained by scaling it inversely to the computational depth to satisfy mass consistency. The winds are nudged to northerly at 5 m/s above 2300 meters msl and to a minimum at 1800 meters. No nudging is performed on the winds below 1800 meters msl. Figure 34 shows the modeled 6-meter height wind fields for 0102 MST. Generally, the modeled winds show a similar pattern to that of the measured winds. Figure 35 shows the modeled vertical profiles at the tethersonde site for the simulation time of 0102 MST. The modeled profile is similar to the observed one (Figure 32) except that the modeled winds exhibit a much deeper surface layer.

The daytime case is a much simpler situation with winds from 310 degrees at 3 m/s. The tethersonde wind profile was relatively simple with some increase in wind speeds above 2500 meters msl. There was a very large difference between the modeled nighttime and modeled daytime turbulence profiles, as shown in figures 36 and 37. The turbulence directly influences the dispersion of the plume. The model requires no stability categorization to correctly describe the major differences between daytime and nighttime plume behavior.

Generally, two kinds of model-observation comparisons were performed. First,

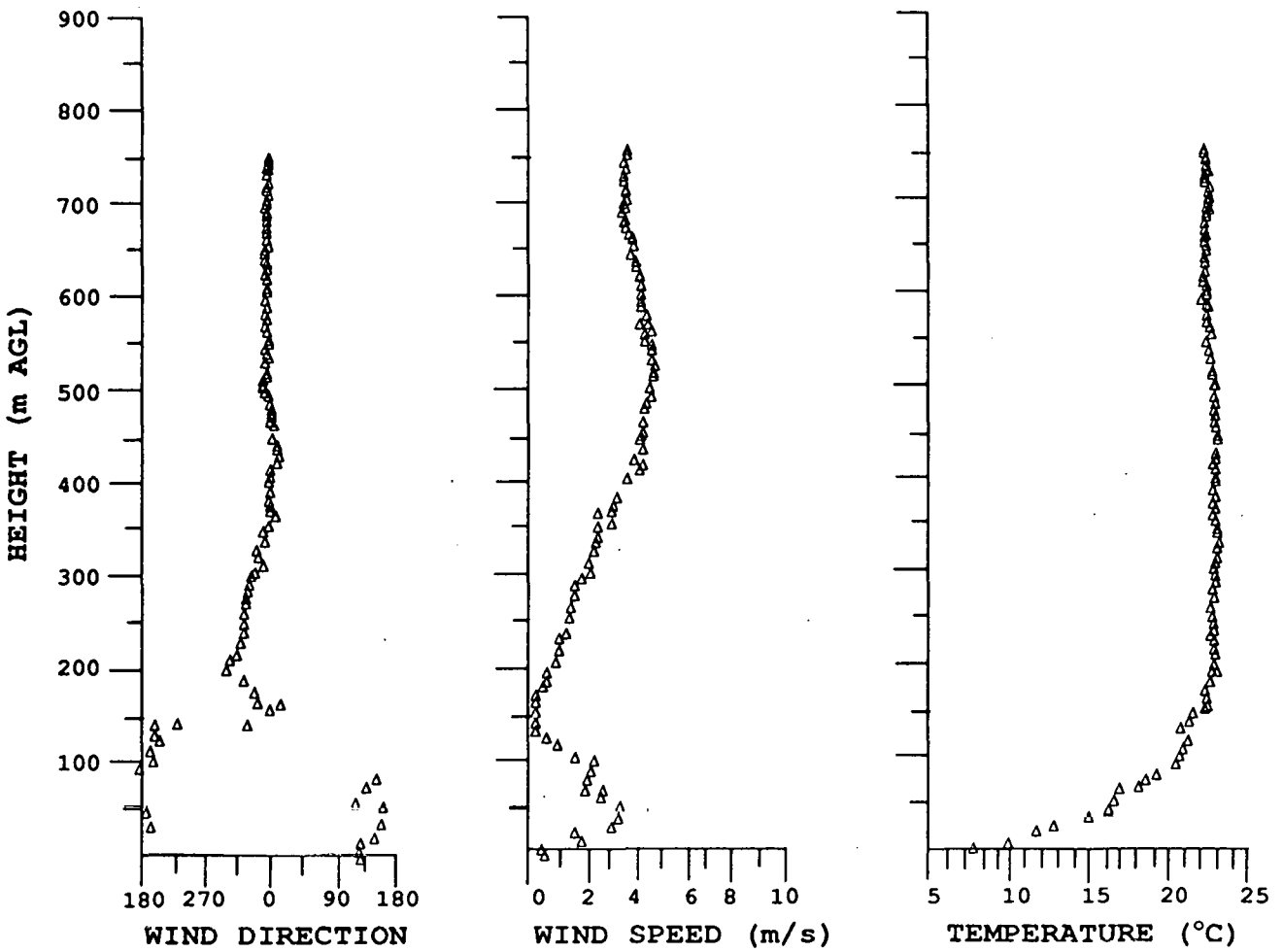

Figure 32: Tethersonde Profiles Measured during the Transport of the Nighttime Release

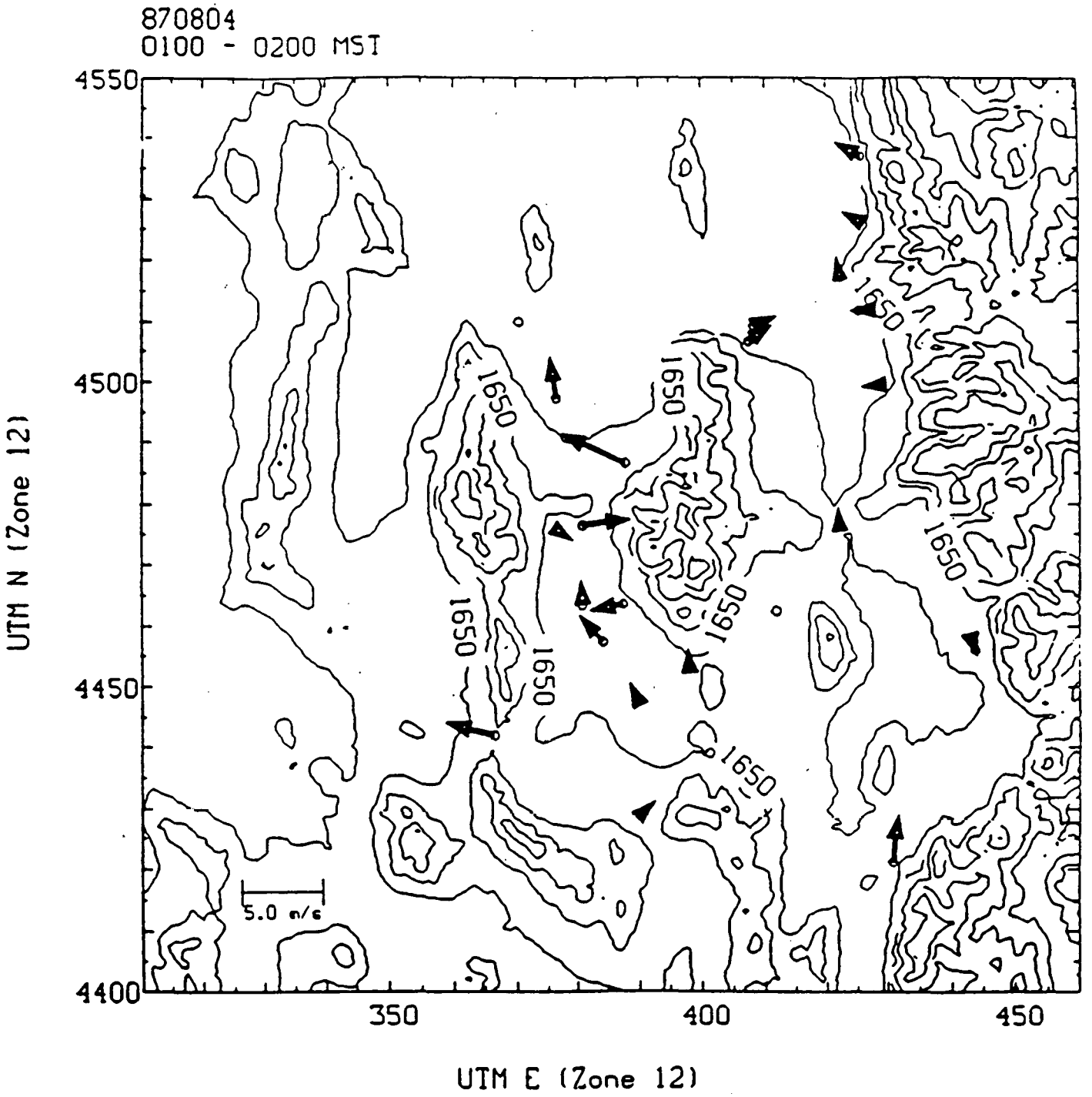

Figure 33: Low-level Winds during Transport of the Nighttime Release

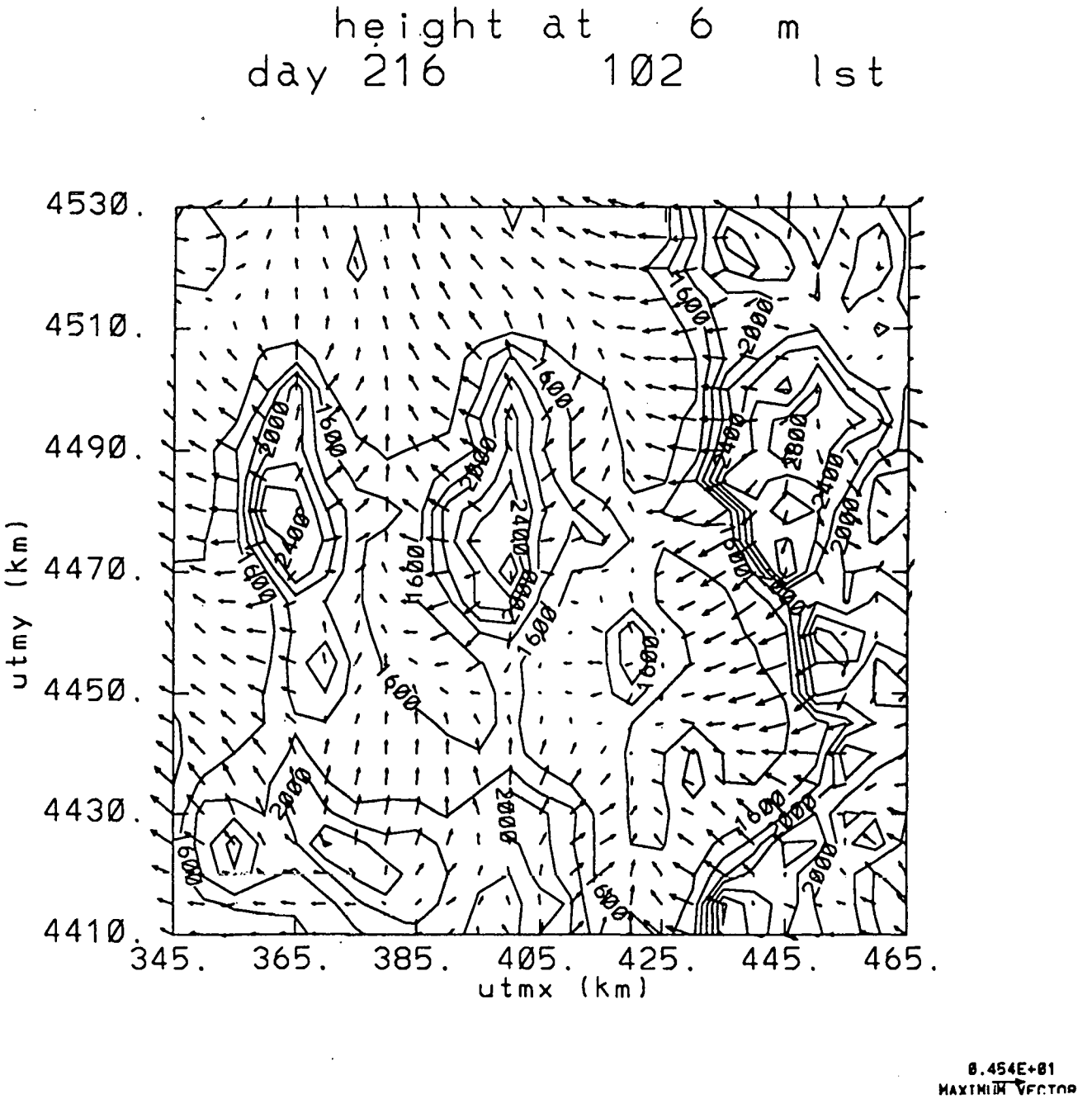

Figure 34: Modeled Low-level Winds during Transport of the Nighttime Release

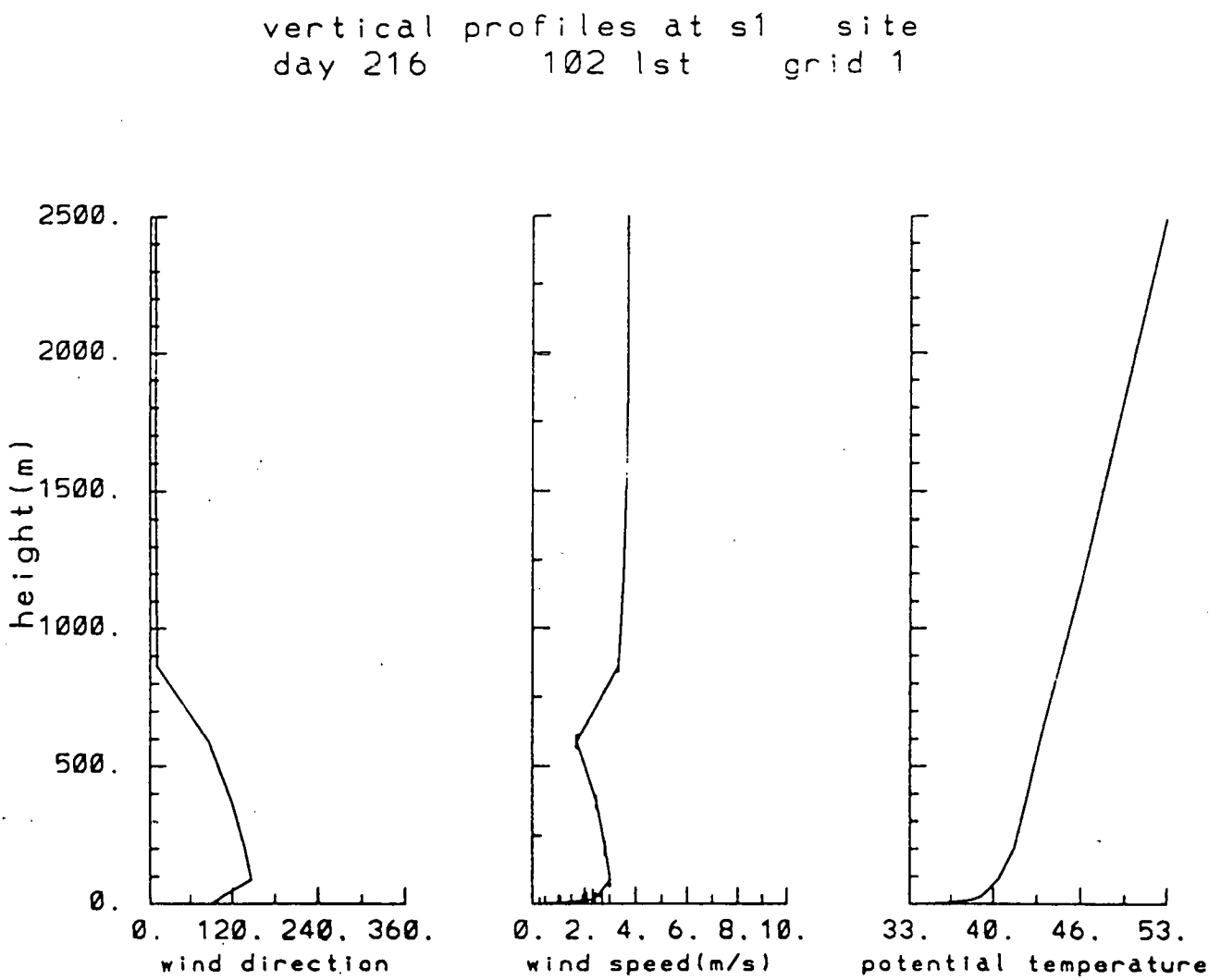

Figure 35: Modeled Vertical Profiles of the Nighttime Release

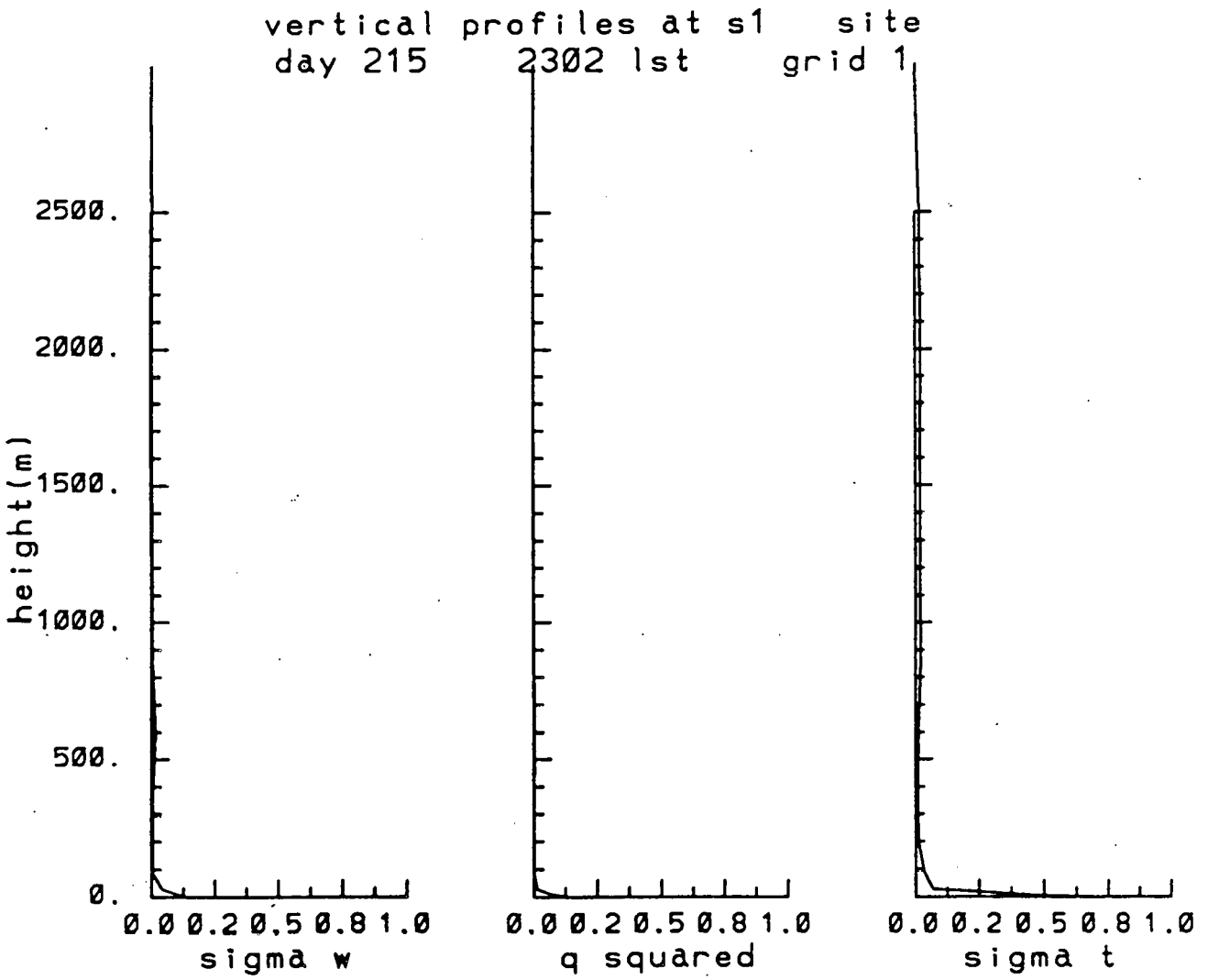

Figure 36: Modeled Turbulence Profiles during of the Nighttime Release

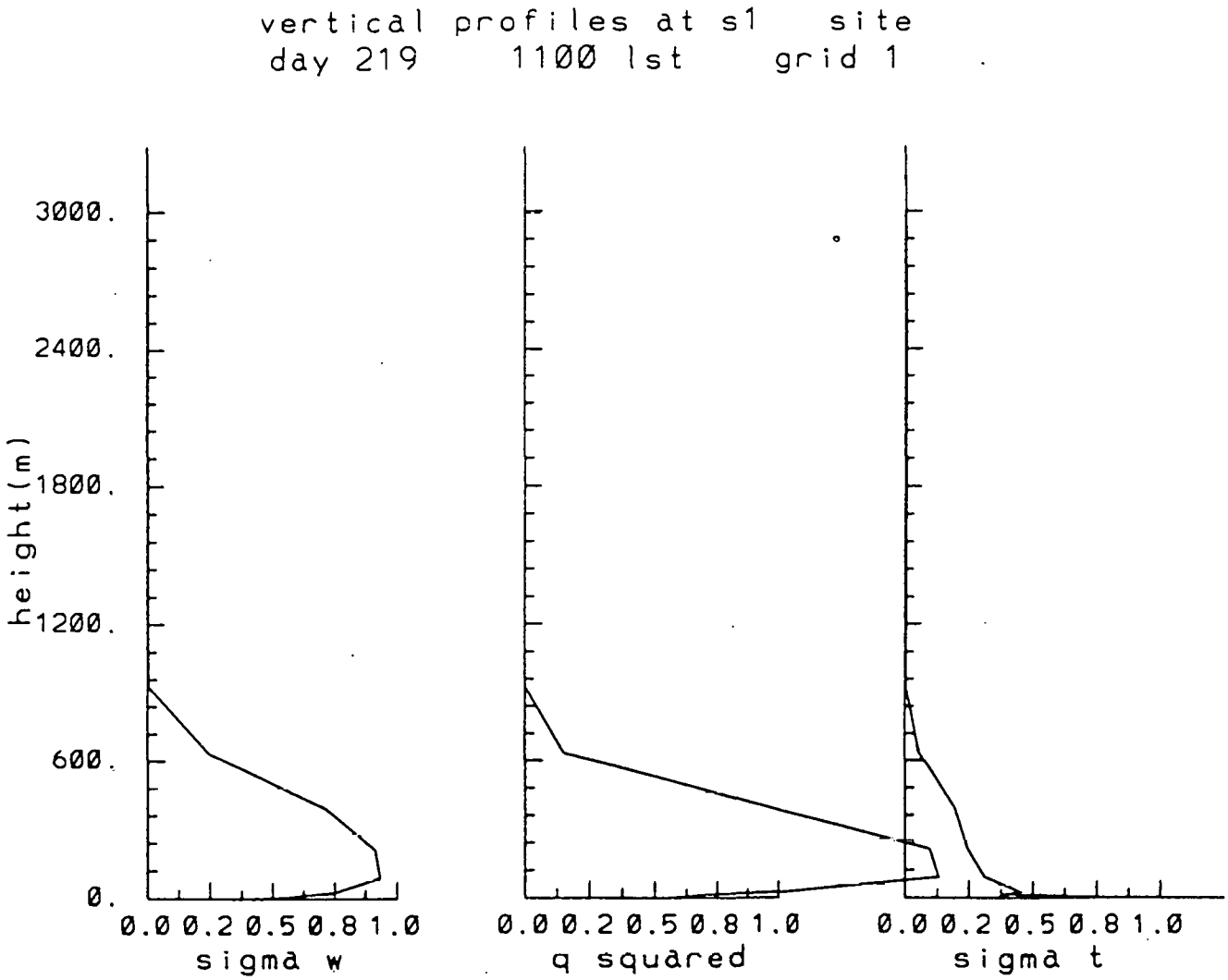

Figure 37: Modeled Turbulence Profiles during the Daytime Release

contour plots on the same scales and with the same contour intervals were prepared for both the observed data and the predicted data. The predictions were obtained by constructing a plume following grid, which included a 15 x 15 array of sampling sites for each hour. The area overlain by the sampling grid was constructed from the southernmost particle position minus 3 times the maximum calculated north-south standard deviation. The northern boundary was the northernmost particle position plus 3 times the maximum calculated north-south standard deviation. The east and west boundaries were chosen similarly. The plume concentrations were interpolated to an 80 x 80 grid, which included all of the hourly plume grids. Figure 38 reports the contours (solid lines) of the observed concentrations for the third hour of the nighttime release. The dashed lines are terrain contours based on the model's terrain grid and the pluses are sampling stations where the tracer concentrations were measured. A few stations on higher terrain were added to more realistically confine the plume. Concentration contours are 700, 3000, 7000, and 9000 ppt and were chosen to define the principal features of the observed data. The asterisk denotes the release point. Note that there are relatively few sampling locations within the concentration contours, consequently the position of the contours is poorly defined. The observations at the locations within the contours are very much higher than the values outside of the contours. Many more samplers would have been required to precisely define the plume widths. The sample density is adequate to demonstrate that a long plume occurred because there are at least 3 well-separated locations with high concentrations. However, in the cross-wind direction, there is typically only 1 point with high concentrations so that the actual plume width could have been anything from near zero width to the distance between the points on either side of the point within the contours. Another factor that complicates the interpretation of the concentration contours is the possibility of non plume SF_6 material, which could be up to a few hundred ppt in concentration.

Figure 39 reports the modeled tracer concentrations for the same hour. The modeled results fail to show the swing back to east near the south side of South Mountain, which is evident in the observed results. The modeled results appear to extend further back toward the source and show a narrower plume than does the observed plume, however these perceived differences are most likely artifices of the contouring package and the very sparse sampling array. One notable feature shared by both the model results and the observed data is a relatively long plume and a plume that starts near the source. Figure 40 reports SF_6 concentrations calculated with a Gaussian plume model for the same hour with E-stability and 3 m/s winds from 160 degrees. The Gaussian plume misses the concentrations near the source and it shows no deflection by the terrain.

The second type of comparison is the station time concentration profile. For this comparison, sampling locations were picked that included the highest concentrations found over the first 7 hours. The sites are marked with numbers in Figure 38. Those sites marked with numbers with a prime are simulated sites

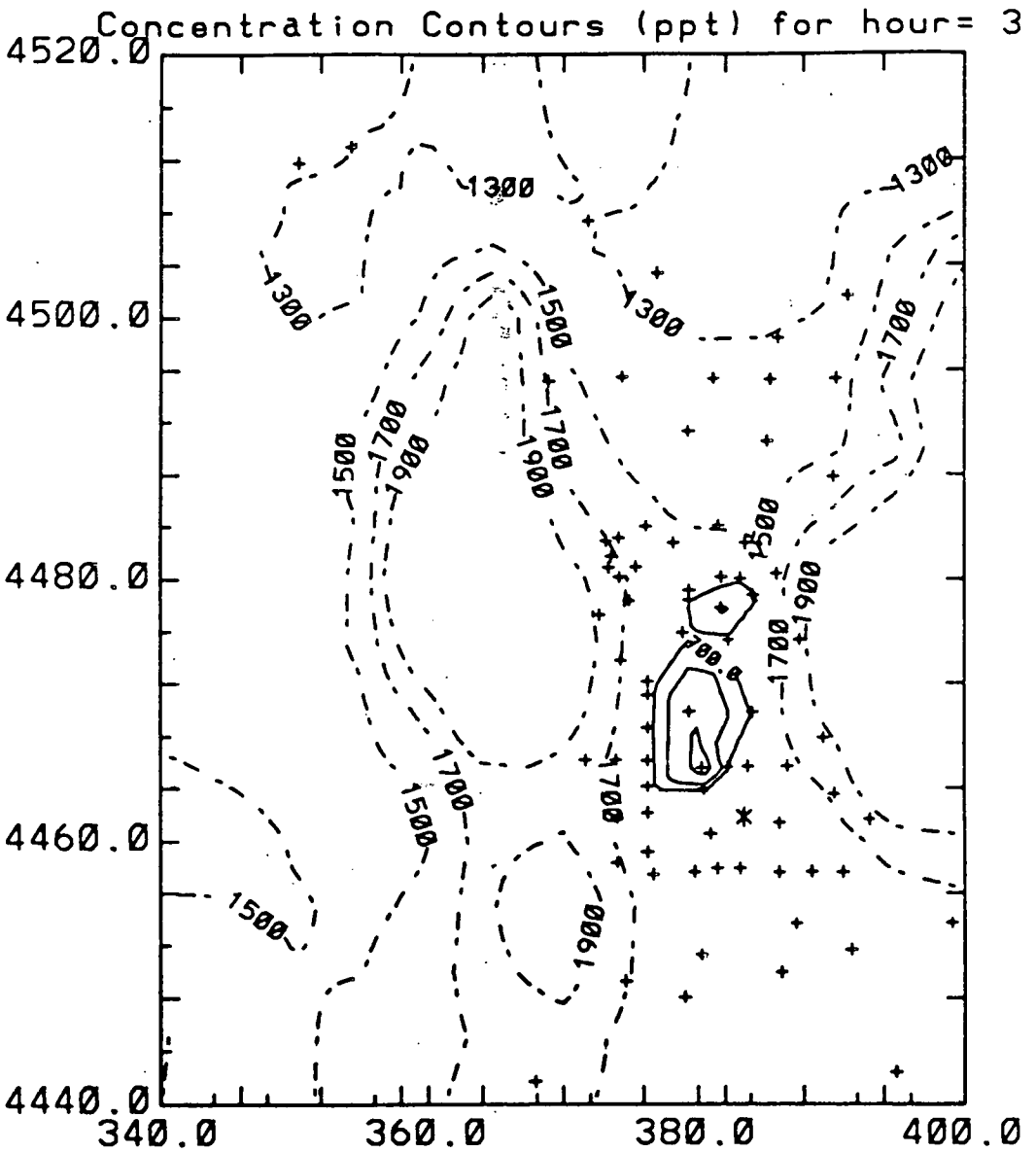

Figure 38: Observed Tracer Concentrations during the third hour of the Nighttime Release

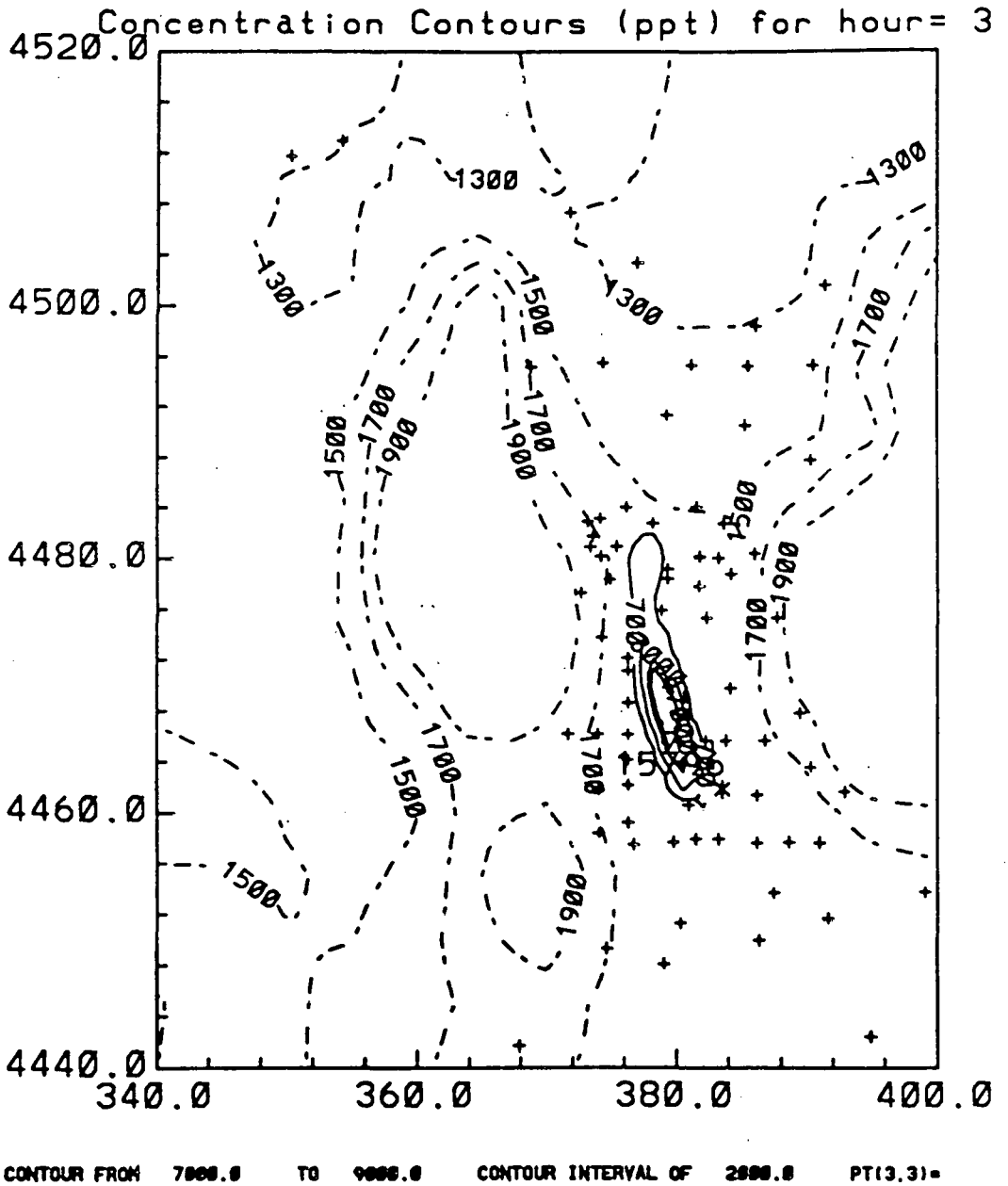

Figure 39: Modeled Tracer Concentrations during the third hour of the Nighttime Release

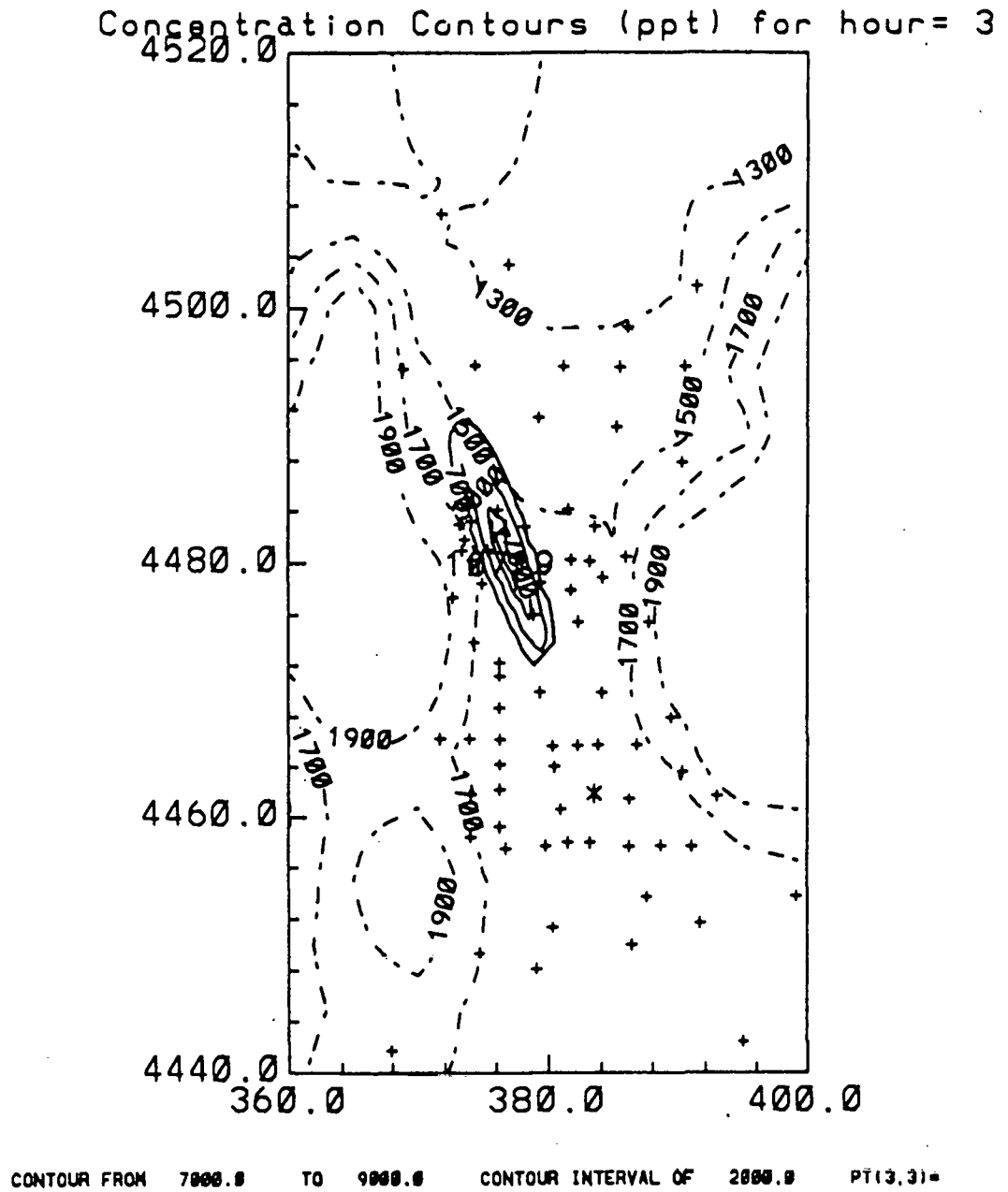

Figure 40: Tracer Concentrations Modeled with a Gaussian Plume during the third hour of the Nighttime Release

used when the simulated plumes differed significantly from the observed plume. Figure 41 shows an example for the station at site 1. The concentrations are reported in parts per trillion and the observed data is denoted by asterisks. In all cases the data are 1-hour averages. For the modeled concentrations, values less than the threshold of 10 ppt are reported as 10 ppt.

Figure 42 reports a comparison between measured and modeled concentrations at site 1 for a Gaussian puff model. The Gaussian puff model shows a much different time behavior, because it does not treat the effects of the wind profile, and therefore gives poor results. Site 1 is approximately 10 km north-northwest of the release site. Both the modeled and observed calculations suggest that the concentrations can persist for hours despite the fact that the duration of the release was only a single hour. It would be most inappropriate to treat these plumes with a Gaussian puff model, because the change in wind speed near the ground plays an important role in the time-concentration profiles.

For site 2 the modeled plume missed the site and produced less than 10 ppt concentrations. Site 2 is 18 km almost due north of the release site and represents the area where the plume was diverted east around South Mountain. Model calculations for a site 6.4 km west of site 2 showed a behavior similar to the observed behavior at site 2. The center of the modeled plume was approximately 20 degrees different from site 2. The Gaussian puff model missed the site by a wider margin and produced no significant concentrations at the site.

Site 3 is about 17 km north of the release site and is just 1.6 km southeast of site 2 and is also associated with the deflection around South Mountain. Once again the modeled concentrations are negligible at this point. Modeled concentrations for a point 7.4 km west of site 3 were similar to the observed concentrations at site 3. The observed concentrations at sites 2 and 3 displayed differences which suggest that the plume was narrow with large fluctuations.

Figure 43 compares the modeled and observed concentrations for site 4, which is approximately 22 km north-northwest of the release point. In this case the modeled plume is fairly similar to the measured plume. The Gaussian model as shown if figure 44 gave non background concentrations for this site but it showed much different behavior with only a single hour showing concentrations above background. Of the five sites examined, the Gaussian model gave above background values at only sites 2 and 4. Model calculations for site 5, which is 42 km from the release site, showed behavior similar to the observations, although the modeled concentrations were somewhat lower than the observations. Figure 45 reports the observed concentrations for the second hour of the daytime release. In this case the concentration contours are drawn for levels of 80, 120, 200, and 350 ppt. Figure 46 reports the modeled concentrations for the second hour. The results are similar in view of the large uncertainties posed by the limited number of samplers.

The highest predicted and measured concentrations occur for site 1, which is 6.5 km from the release site with a bearing of 128 degrees. Figure 47 displays the behavior for site 1. The model shows similar behavior to the measurements,

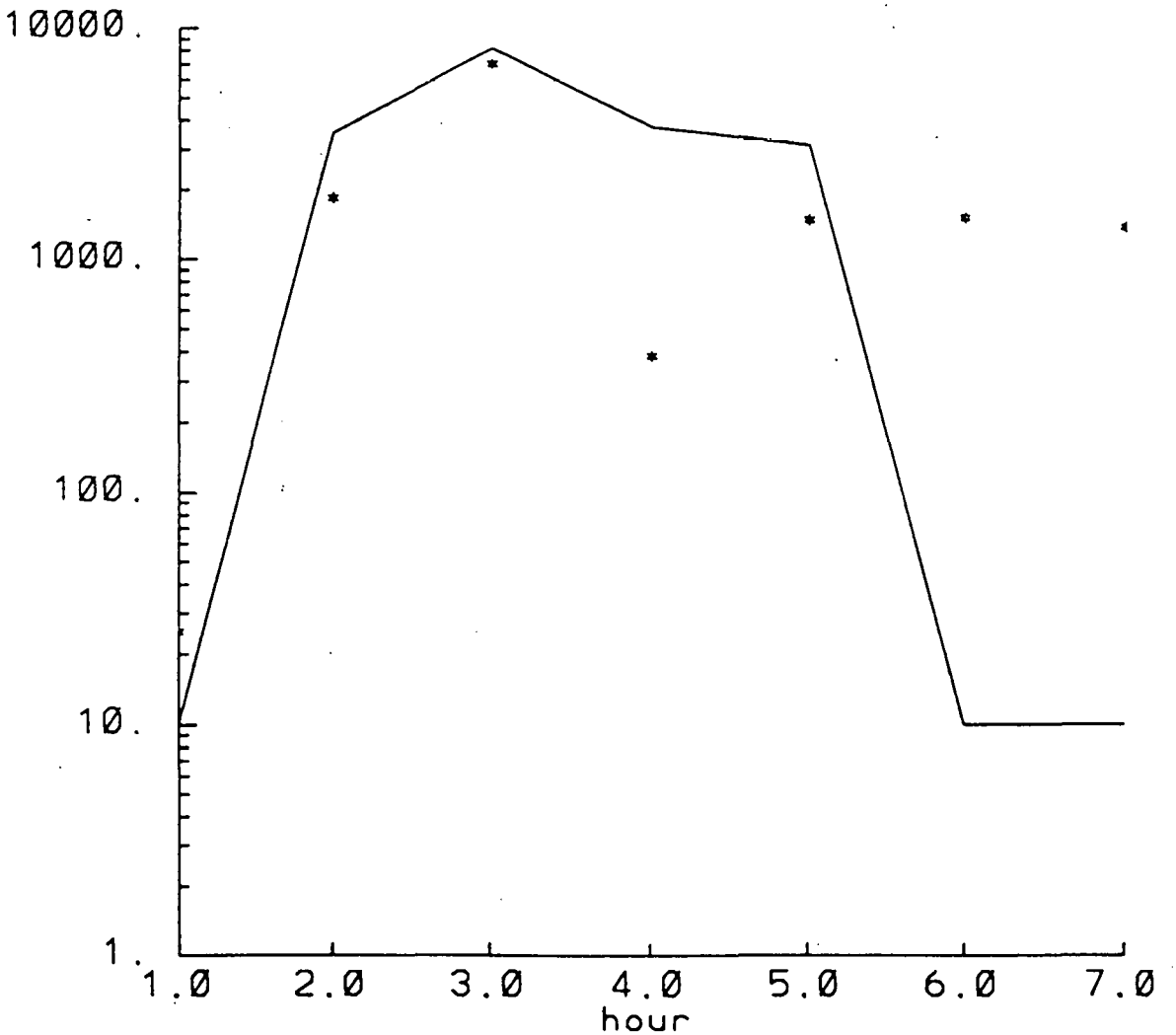

Figure 41: Tracer Concentrations at site one during of Nighttime Release

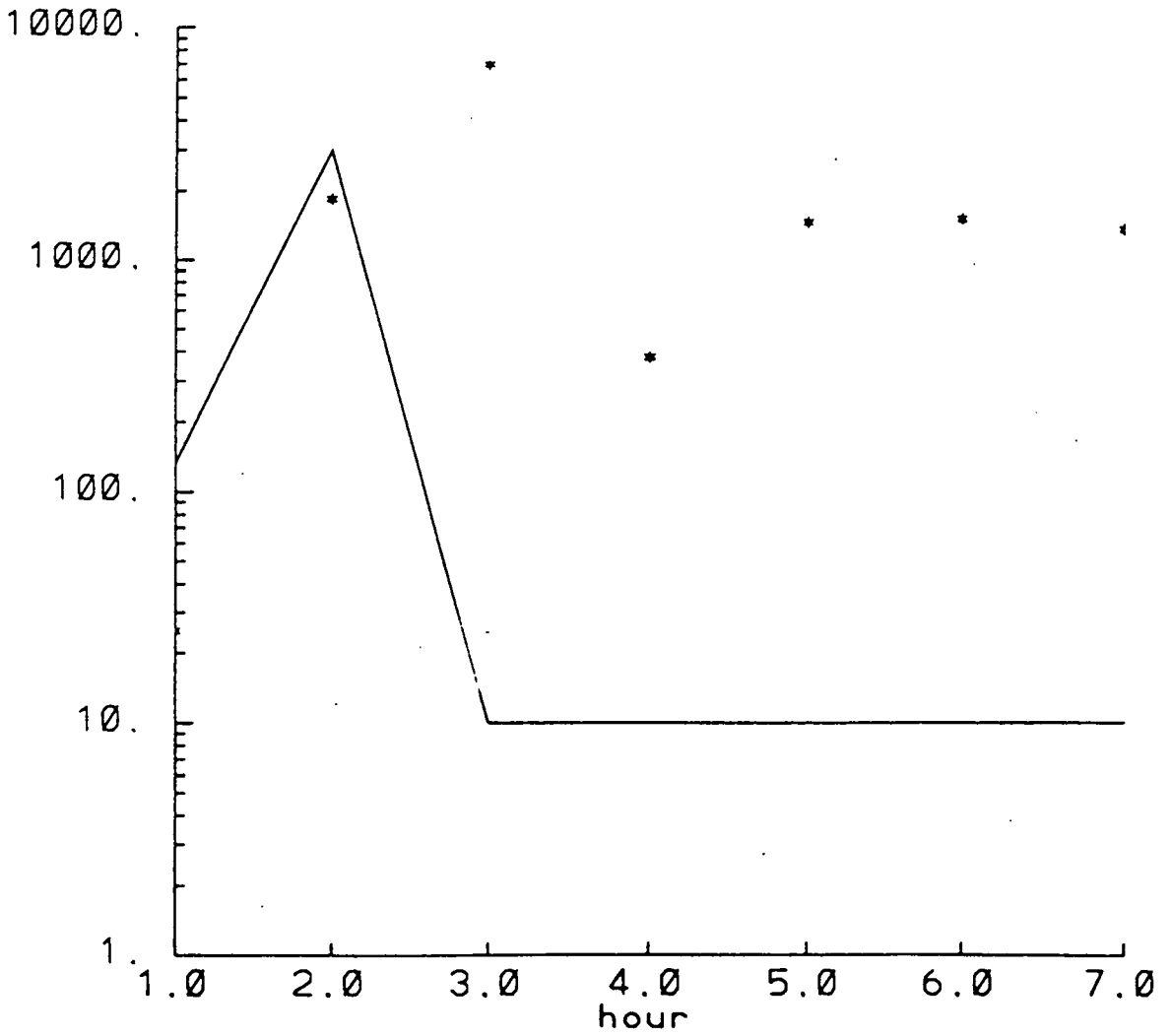

Figure 42: Tracer Concentrations Modeled with a Gaussian Plume at site one during of Nighttime Release

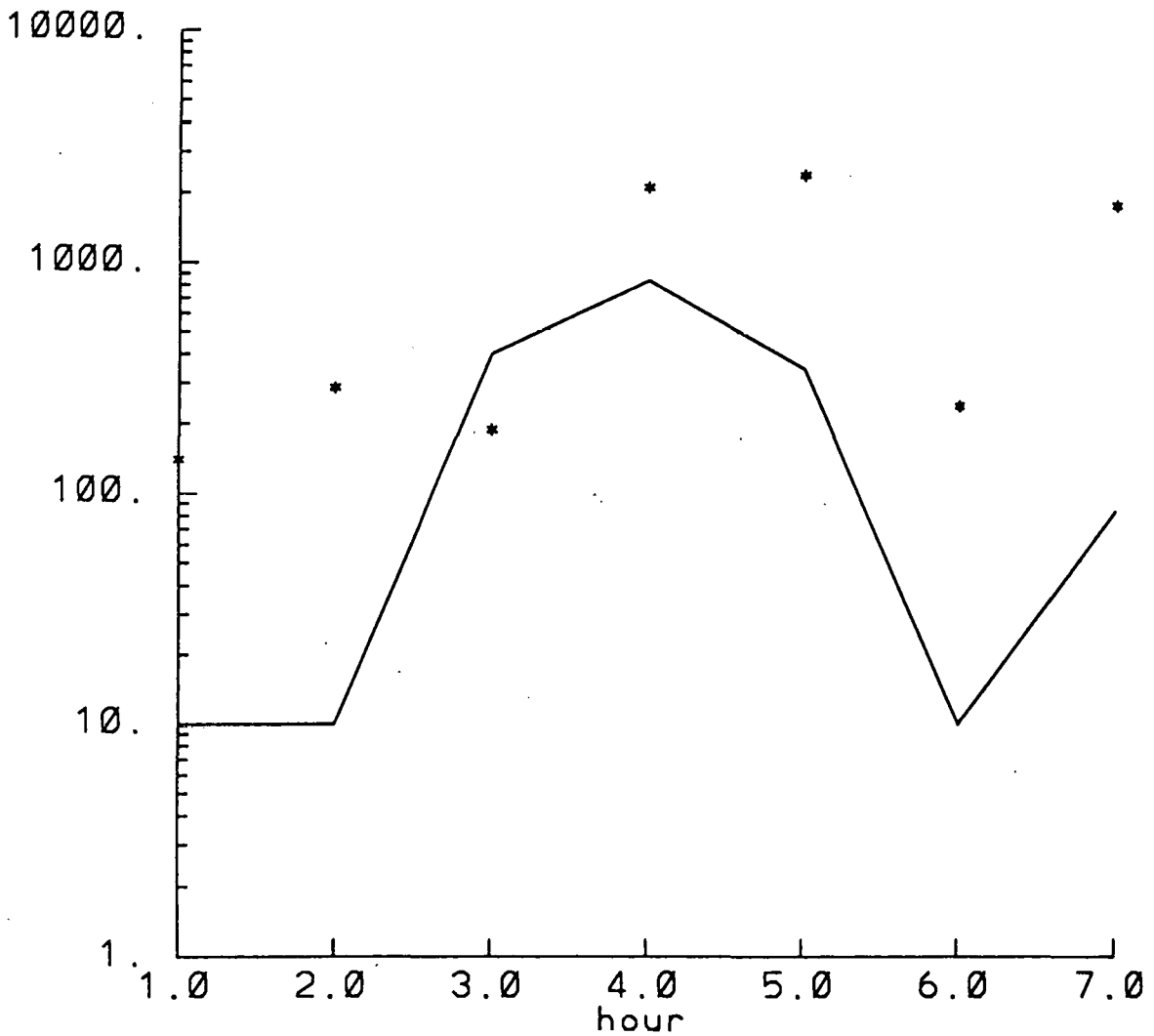

Figure 43: Tracer Concentrations at site four during the Nighttime Release

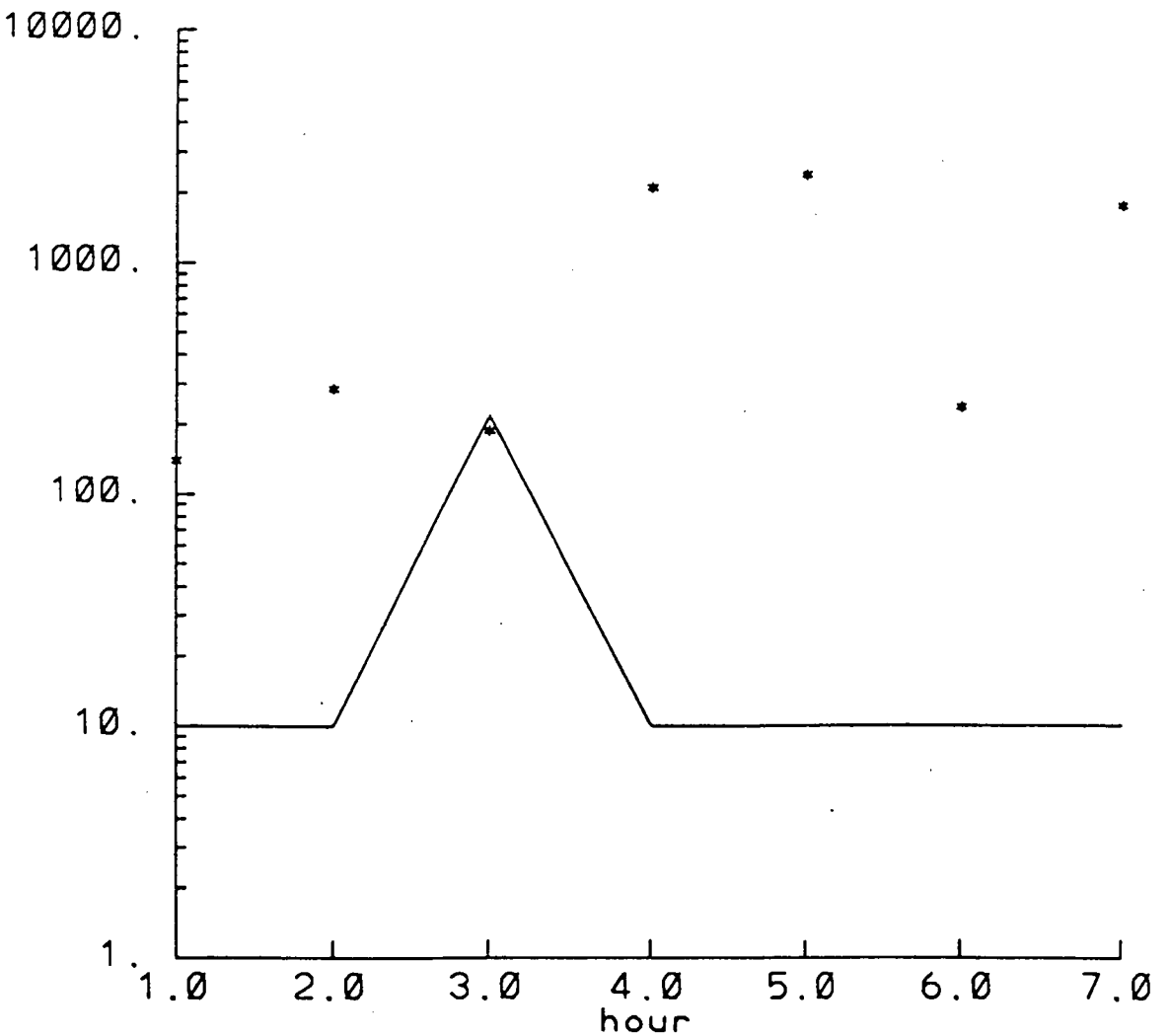

Figure 44: Tracer Concentrations at site four Modeled with a Gaussian Plume during the Nighttime Release

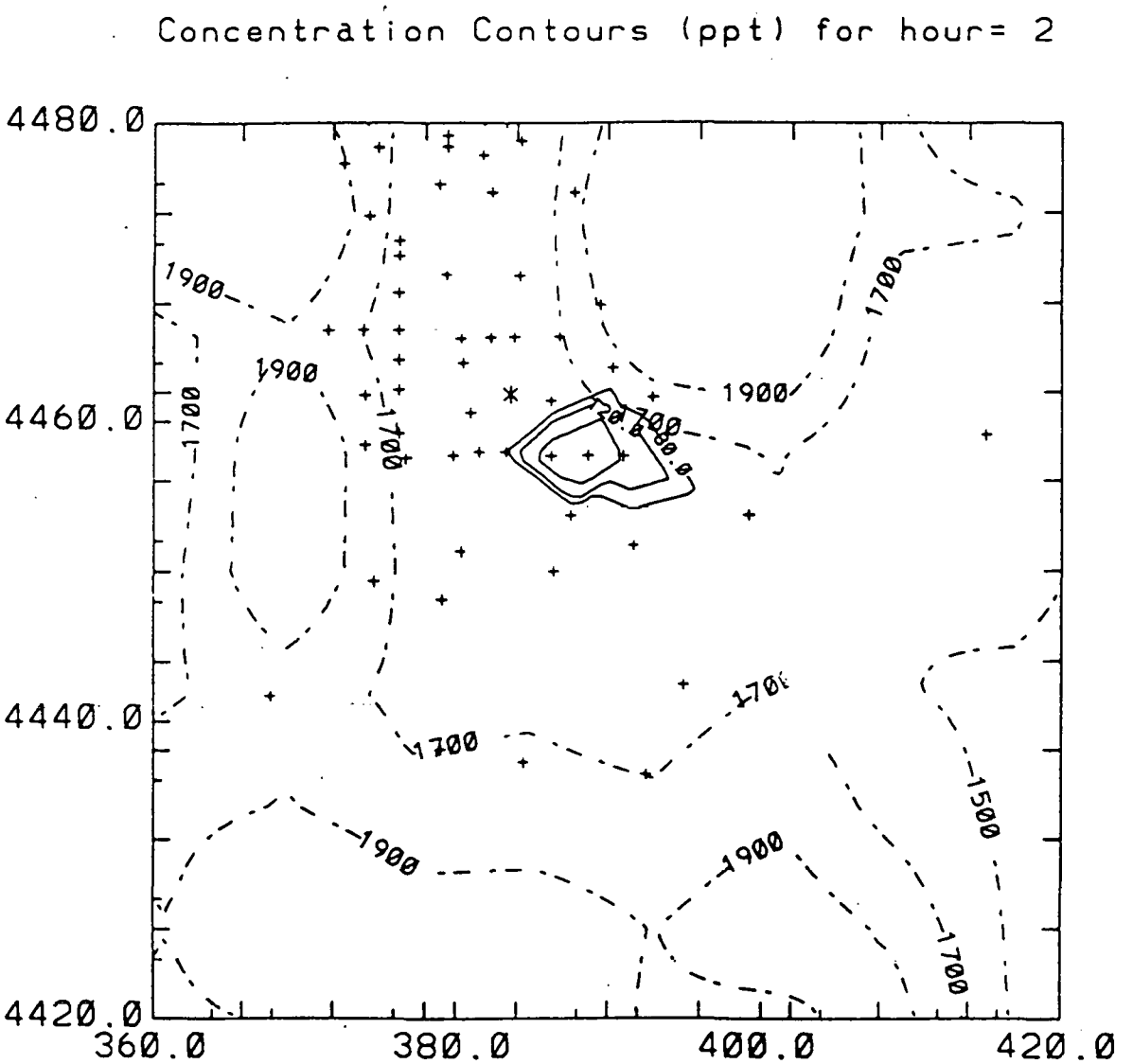

Figure 45: Observed Tracer Concentrations during the second hour of the Daytime Release

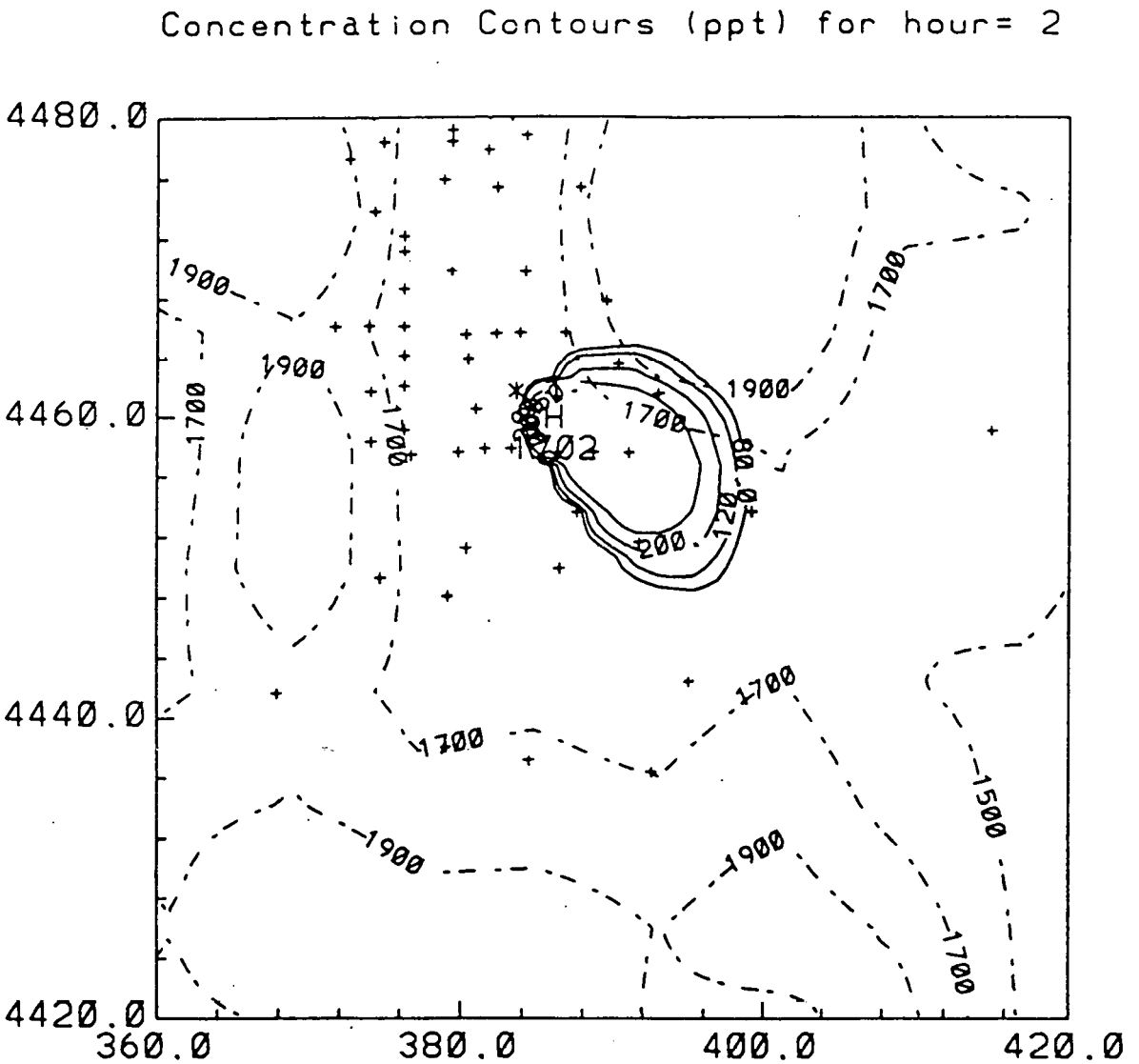

Figure 46: Modeled Tracer Concentrations during the second hour of the Daytime Release

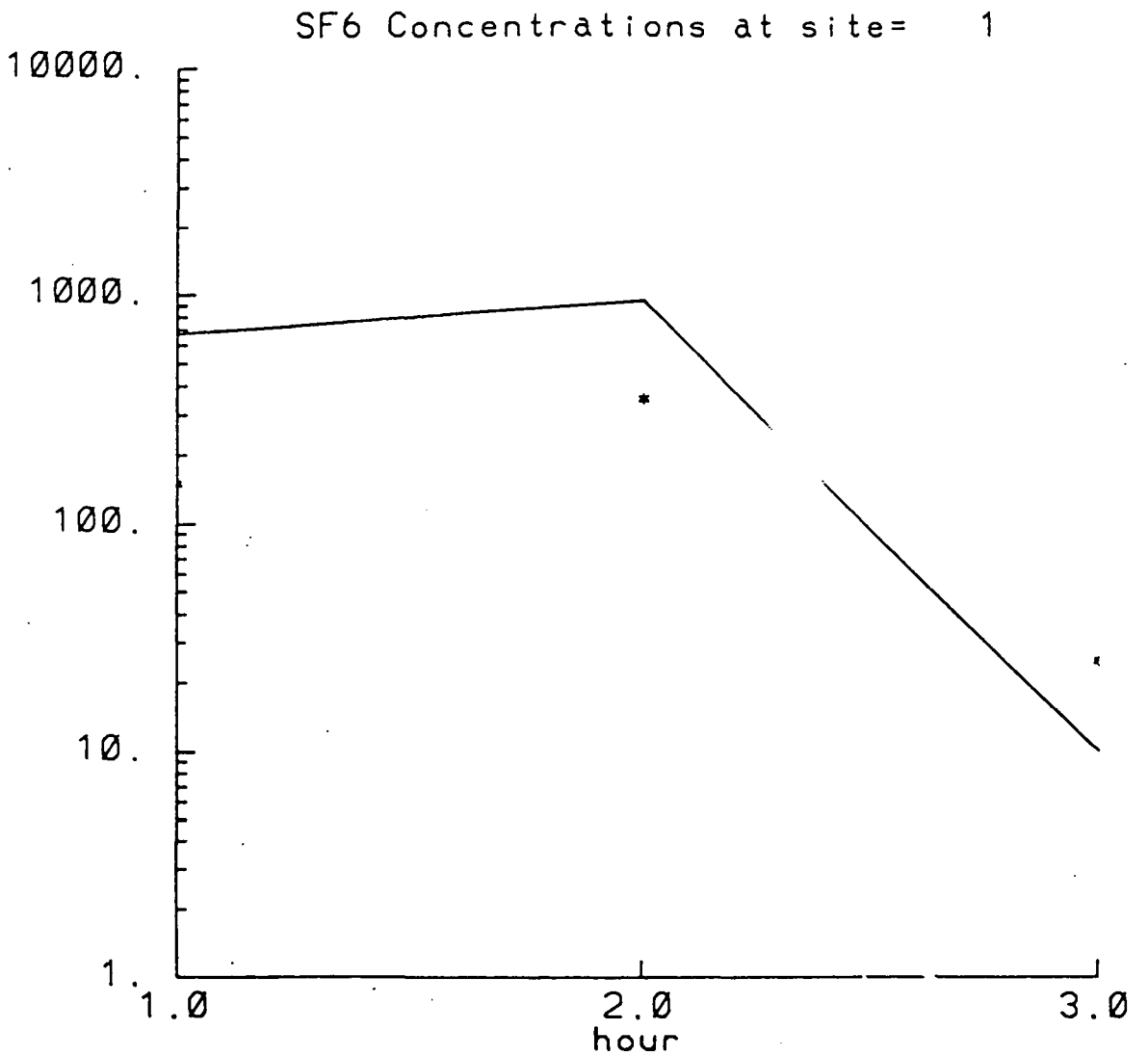

Figure 47: Tracer Concentrations at site one during the Daytime Release

although it appears to over-predict slightly.

5 Atmospheric Chemistry Model, ATMOS

5.1 Model formulation

The chemistry model is more flexible than the other components, of the system because it is basically a formal structure in which differing sets of chemical equations can be solved. The important part of the model is not the structure, but instead is the particular set of equations which are solved within the structure. At present the system uses a LaGrangian box formulation in which a homogeneous mix of gases is exposed to time-dependent solar radiation fluxes and is supplemented by new source material and diluted by background air. The dilution rates and the rate of addition of source material is defined by RAPTAD as is the position of the box.

A more elaborate system in which multiple boxes will be used with exchange between boxes is currently being written. The multiple box system is much more complicated because the boxes no longer drift with the wind but instead cover the entire domain over which RAPTAD pseudo-particles are found. Consequently, advection and diffusion from one box to another must be calculated. Thus the multi box system has all of the complexities of the Eulerian system with the additional complexity that the box boundaries move with time. However, it has the computational advantage that only the domain in which pollution is found at any time must be considered. This feature means that the early evolution of a plume can be much better described because the cells are much smaller at early times than at later times.

5.2 Model usage

The most important features of the atmospheric chemistry model are provided by the particular set of chemical equations, species, and radiation fluxes which are used in a given application. Figure 48 summarizes past applications with the significance of each application.

In the Tokyo application the principal focus was linked meteorology and chemistry for an aged plume which travelled in excess of 120 kilometers. In the Rio De Janeiro case the interest was in the role of oxygenated fuels and their impact on peroxyacetylnitrate and other photochemical species.

The Denver Brown Cloud study was more relevant to the situation of Mexico City in several respects. First, Denver is at relatively high altitude. Second, the sources in the Denver study included more older cars which are more representative of those in Mexico City, and third the period of interest was in the wintertime which is also important in Mexico City.

PHOTOCHEMICAL MODEL
PAST APPLICATIONS

A. DENVER BROWN CLOUD

1. High altitude chemistry
2. Wintertime photochemistry
3. Wintertime secondary particulates (nitrates)

B. RIO DE JANIERO

1. Extensive gasohol and neat ethanol fuel usage
2. Enhanced aldehyde emissions
3. Enhanced photochemical production of peroxyacetylnitrate (PAN)

C. TOKYO - JAPANESE ALPS

1. Long range transport and impact of urban plume
2. Aged urban plume

Figure 48: Summary of Past Applications of the Photochemistry Model

The objectives of the Denver Brown Cloud Study were to: (1) demonstrate the occurrence of wintertime photochemistry, (2) demonstrate the influence of snow cover on wintertime photochemistry, and (3) begin to combine meteorological and chemical tools to provide a more realistic description of atmospheric processes. The approach was to select two weekdays on which relatively clear skies had prevailed during brown cloud episodes. The characteristics of the days selected are summarized in figure 49.

Once the days were selected they were modeled with HOTMAC which was modified to include snow cover and urban heat release. RAPTAD was then used to describe the stable pollutant concentration field associated with a disk source designed to represent the mobile sources during a weekday in Denver. The source was chosen to be a disk of radius 18 km with a depth of 20 meters.

RAPTAD was used to define where on the horizontal domain the most pollutants were located at each hour. Once these points were chosen concentrations were calculated for samplers at these sites. The resulting concentrations were used to define dilution rates and initial conditions for the chemistry model.

The characteristics of the photochemical box model are summarized in figure 50. Figure 51 summarizes the model parametrization which was used.

5.3 Dry day simulations

The simulations were initialized with a late afternoon sounding on the preceding day. Figure 52 displays the wind field at 1200 mst at a height of 1766 meters above the terrain. At this height the wind fields are very similar to the initial field excepts for some areas near the southern boundary. Figure 53 displays the wind fields at 28 meters above the surface at 6 mst. The circle indicates the source area used in the particle simulations. Figure 54 displays the winds at 12 mst. The winds near Denver have developed the light southwesterly character observed at the time. Figure 55 plots the simulated carbon monoxide concentrations for near ground level samplers moving at the approximate plume centers. The point marked O is an observation. Figure 56 reports estimated NO and NO_2 concentrations in the urban plume.

5.4 Snow day simulations

The snow day simulations were initialized with 5 meter per second winds from 280 degrees, slightly north of westerly. By 600 mst the winds near Denver had been significantly modified as shown in figure 57. The winds changed slightly during the day as can be seen in figure 58 which reports the winds at 12 mst. The simulation of emissions began at 7 mst. Figure 59 displays projections of pseudo-particle locations on the surface at 9 mst. The large circle represents the idealized Denver source region, while the small circles represent sampling locations chosen to correspond to the heaviest pseudo-particles concentrations for each hour of the simulation. Figures 60 through 62 display the particle

DENVER BROWN CLOUD STUDY

	November 22, 1978	December 8, 1978
Sky:	Clear and sunny	Clear and sunny
Daytime temperatures:	21 to 59 deg. F.	-8 to 16 deg. F.
Winds:	Light, westerly and southerly	Light, westerly and southerly
Snow cover:	None	Extensive

Figure 49: Characteristics of Brown Cloud Days Chosen for Study

PHOTOCHEMICAL BOX MODEL

DESCRIPTION OF MODEL

Mechanism largely from Atkinson with Seinfeld corrections

Independent photolysis rates (not ratioed to jNO_2)

NH_4NO_3 formation included

VARIABLE WITH TIME

Photolysis rates

Emission rates

Dilution rate

Temperature

Figure 50: Characteristics of the Photochemical Box Model

PHOTOCHEMICAL MODEL
SPECIES INPUT LUMPING SCHEME

A. ALKANES - propane, alkane

B. OLEFINS - ethylene, propene, butene

C. AROMATICS - benzene, toluene, xylene

D. ALDEHYDES - formaldehyde, acetaldehyde, RCHO

E. OXYGENATES - acetone, methyl ethyl ketone

Figure 51: Summary of Photochemistry Model Parameterizations

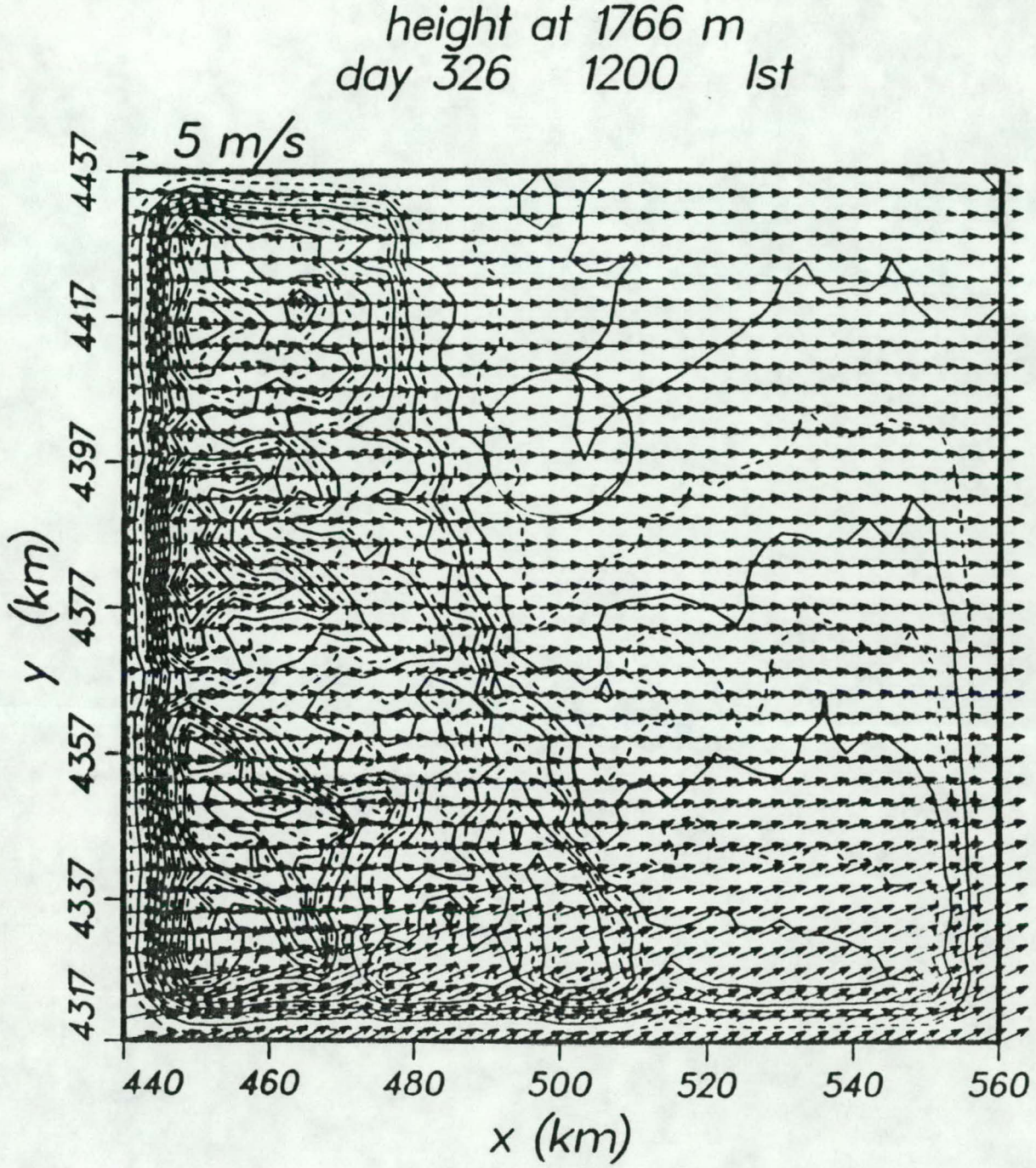

Figure 52: Upper-level Wind Fields during the Dry Day

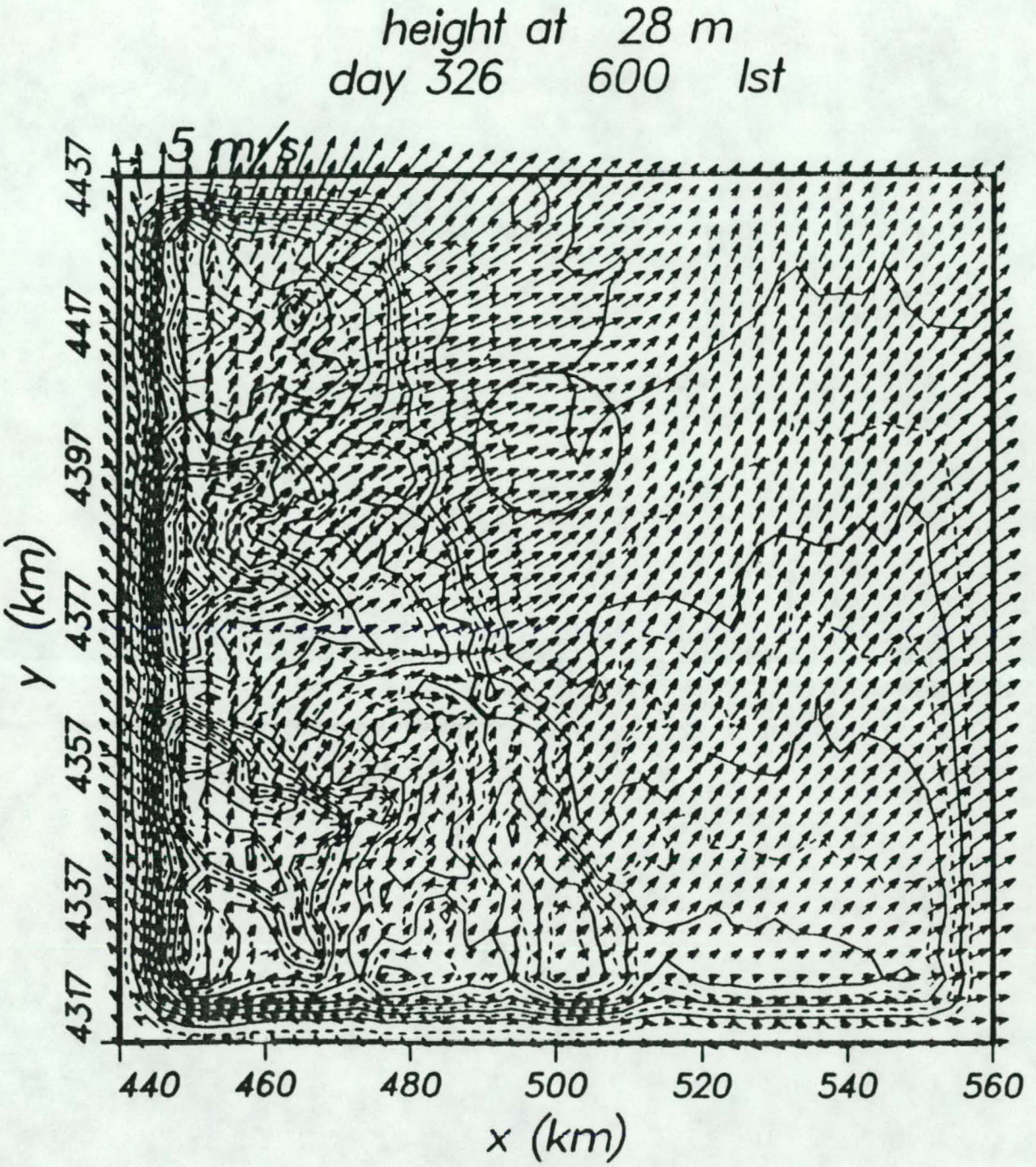

Figure 53: Low-level Wind Fields at 6 am during the Dry Day

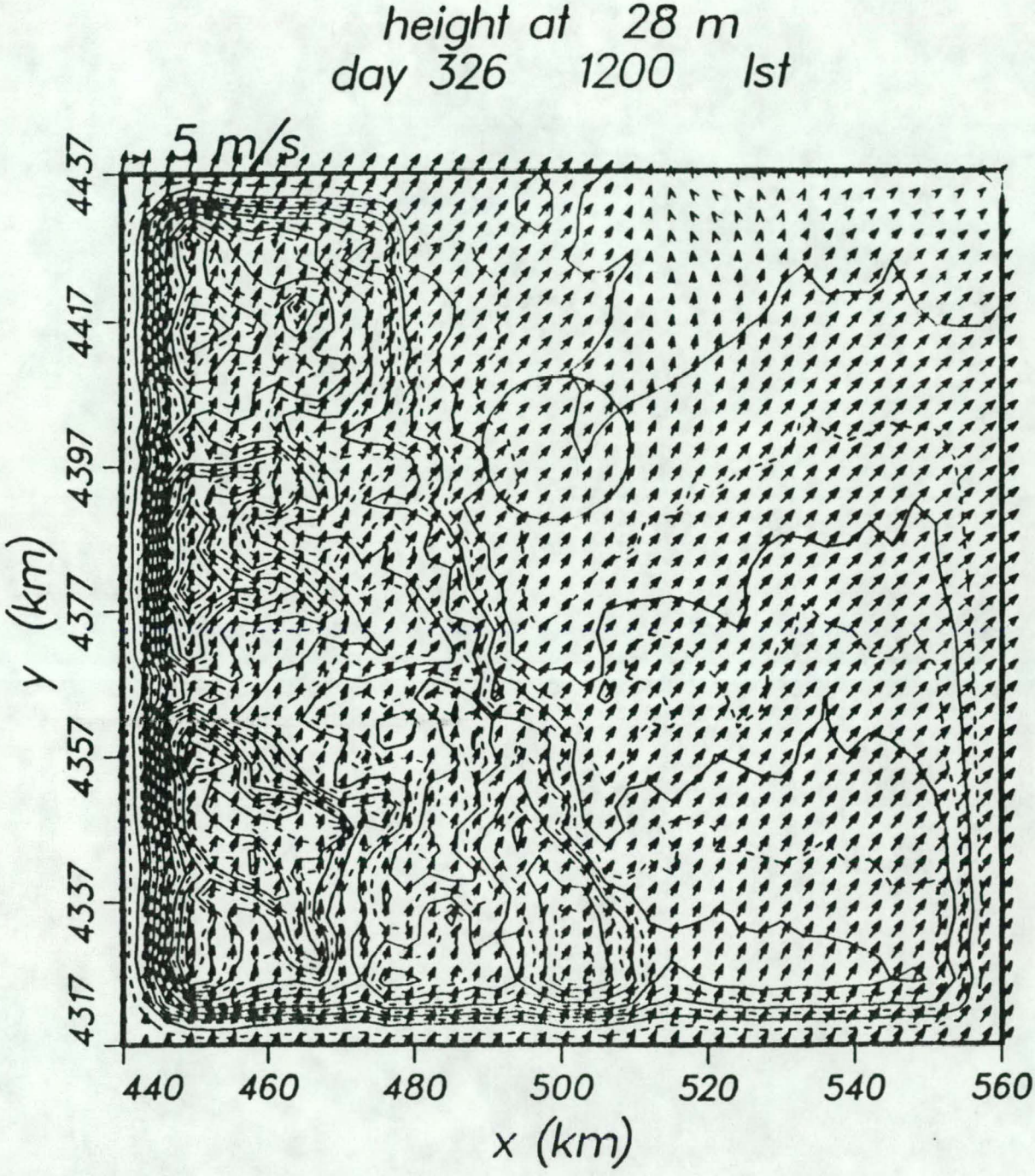

Figure 54: Low-level Wind Fields at 12 noon during the Dry Day

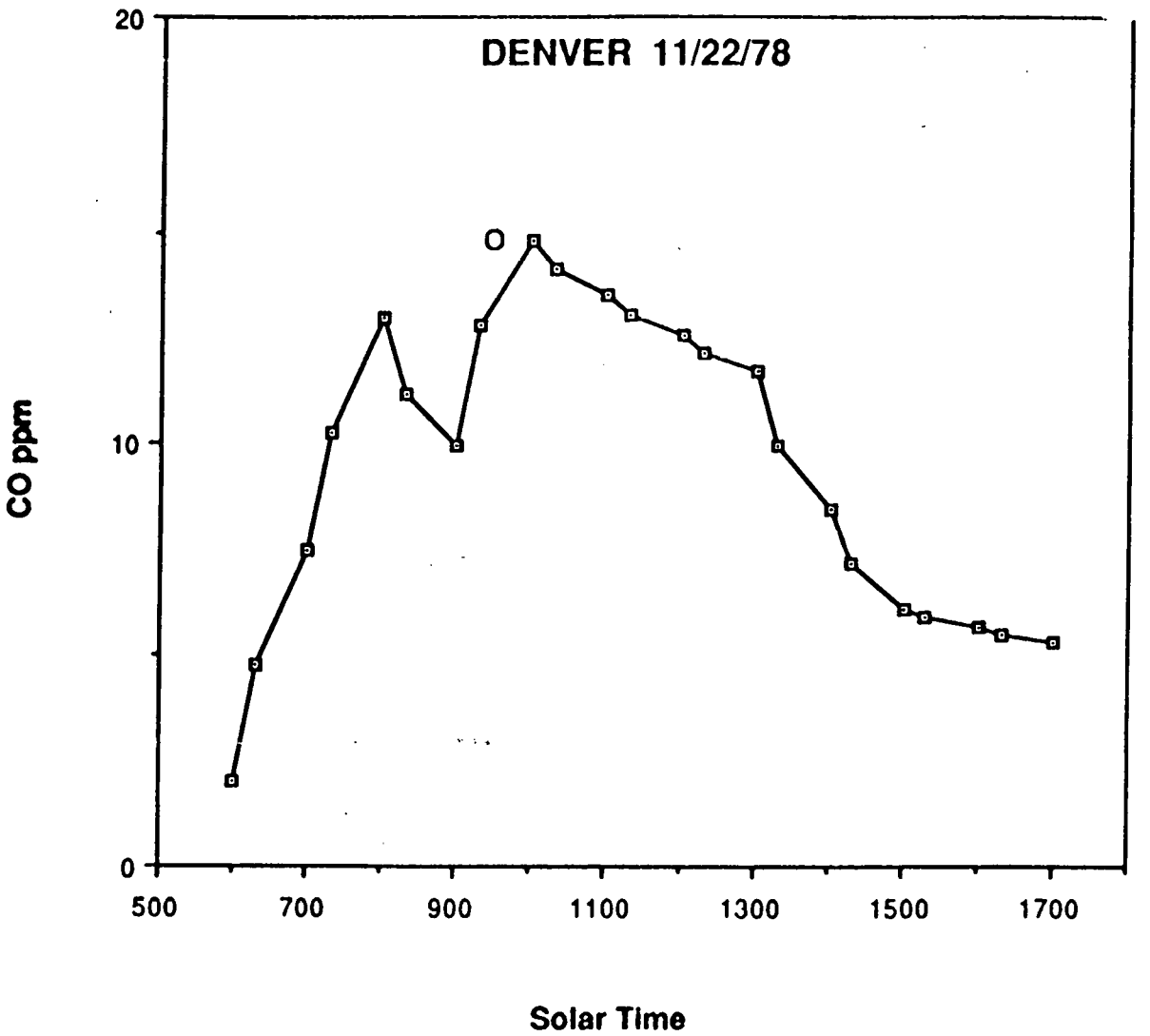

Figure 55: Modeled Carbon Monoxide Concentrations on the Dry Day

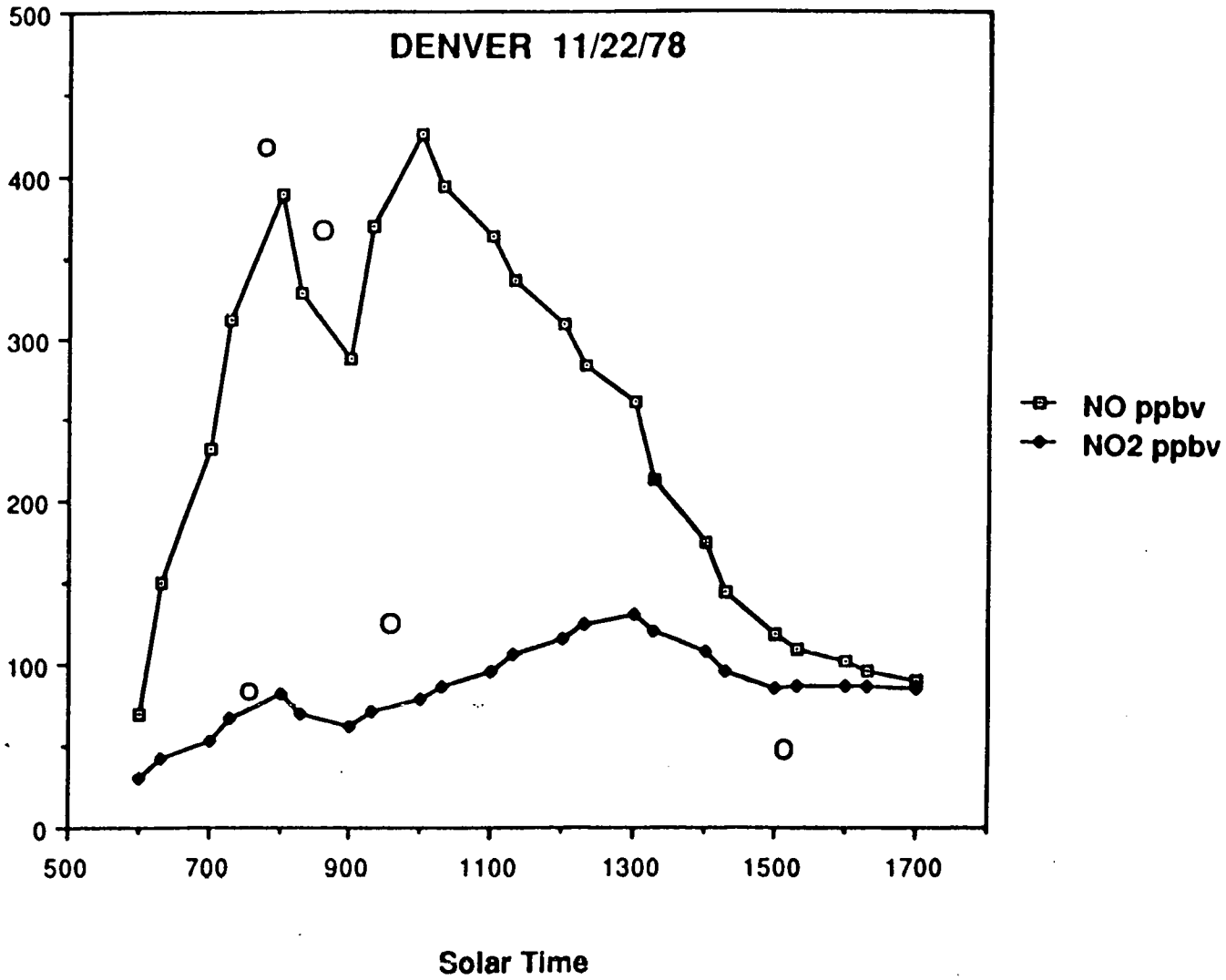

Figure 56: Modeled NO and NO_2 Concentrations on the Dry Day

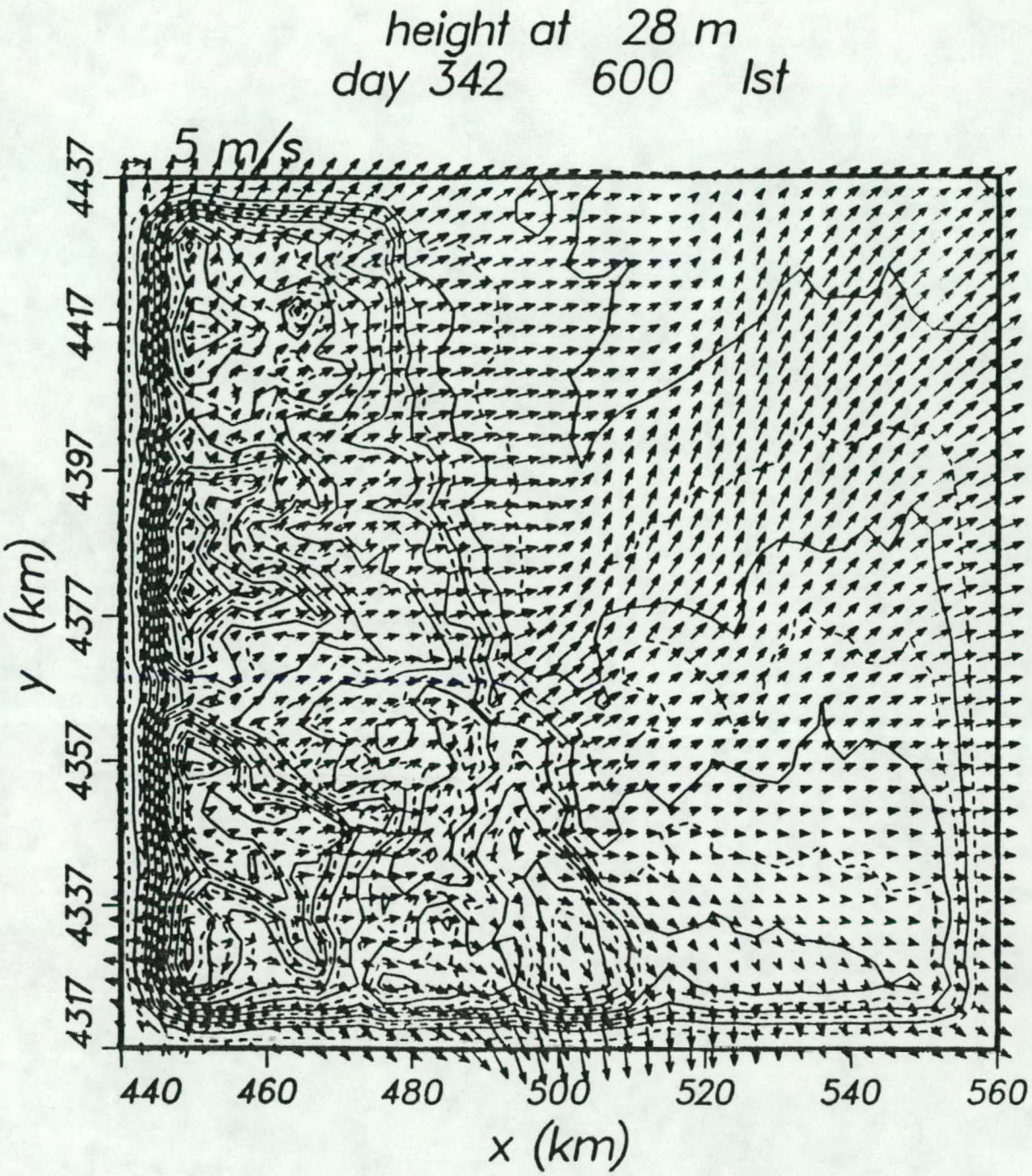

Figure 57: Modeled Low Level Winds at 6 am on the Snow Day

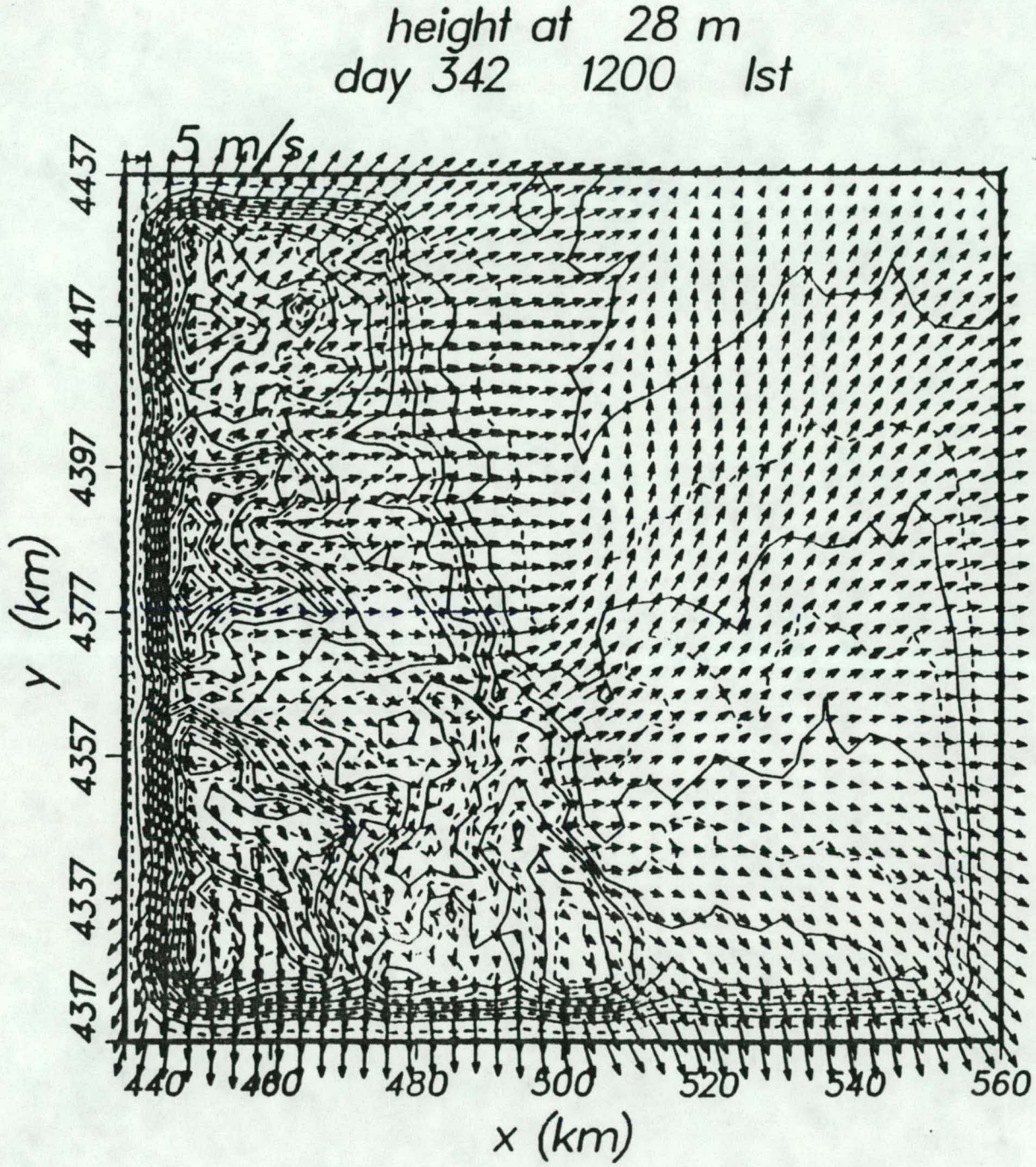

Figure 58: Modeled Low Level Winds at 12 noon on the Snow Day

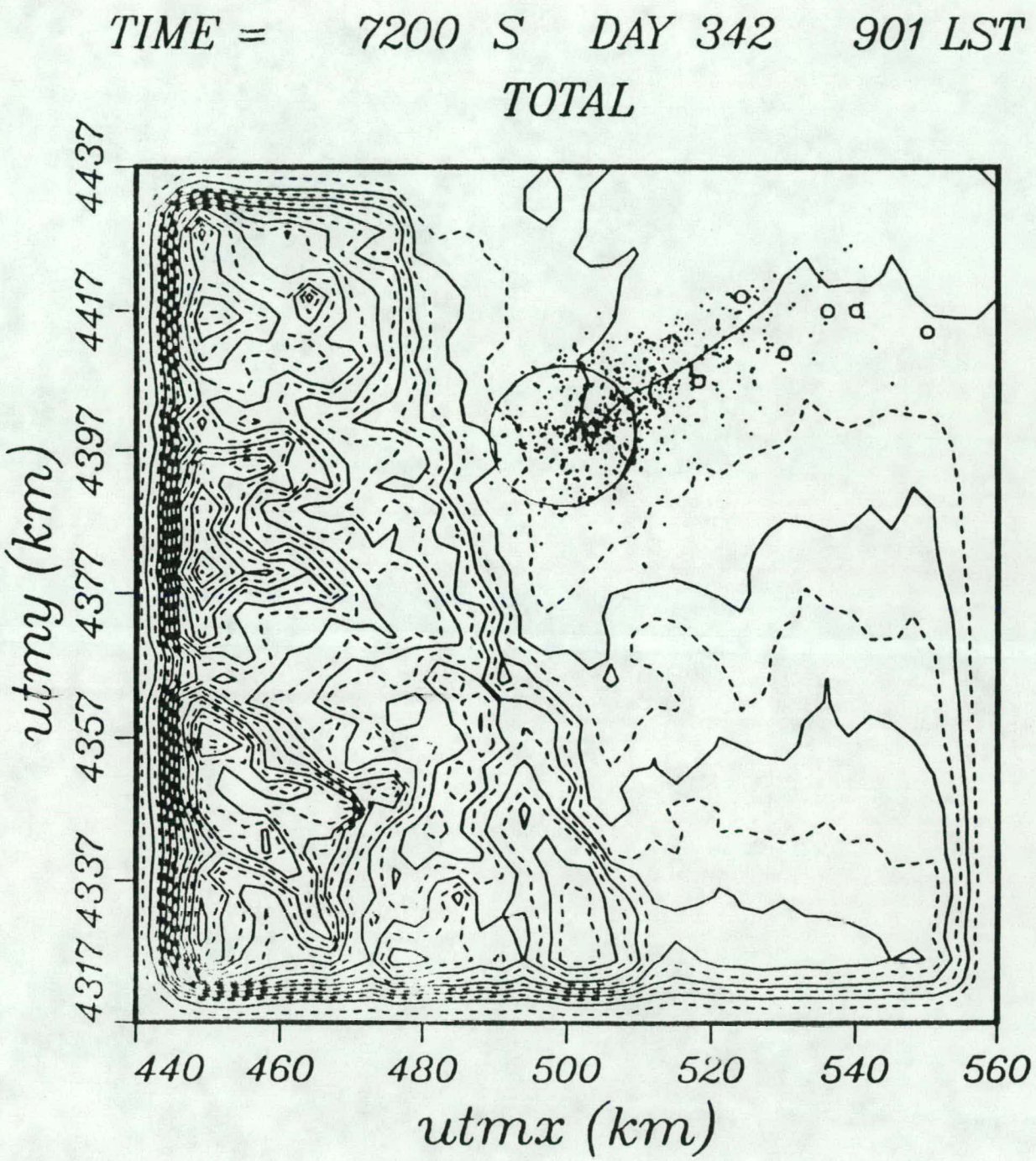

Figure 59: Pseudo-particle Positions at 9 am on the Snow Day

locations for subsequent times. Figure 63 shows the predicted NO and NO_2 concentrations at each time based on the samples estimated for each of the aforementioned sample locations. In each case the concentration for the hour is that associated with the sample site which had the highest concentration of pseudo-particles in its vicinity. Figure 64 reports modeled NO and ozone concentrations, with O denoting the observed ozone concentration.

5.5 Comparison of photochemistry on the two days

Figure 65 reports the calculated photochemical intensity on the two days. Despite a slightly lower sun angle, the snow day, December 8^{th}, had significantly higher photochemical intensity. The higher intensities were reflected in increased production of photochemical species. Figure 66 reports a comparison between ozone on the two days, while figures 67 and 68 report PAN and photochemical nitrate values for the two days respectively. The general behavior of a rapidly increasing nitrate between 8 am and 2 pm is consistent with the measurements (Wolff, et al., 1981). However, the measurements reported 18 micrograms per cubic meter mean value for 8-9 December which would be higher than the model predictions. The calculated nitrate values are limited by a very conservative assumed ammonia source term.

6 The Visibility Model, LAVM

The visibility model produces two types of outputs: (1) numerical indices, and (2) simulated photographs. The numerical indices include parameters such as plume visual range, plume contrast, blue-red ratio, and color contrast. The model is designed to make estimates in either of two situations: (1) plume calculations where the concentrations are variable along a line-of-site, and (2) uniform haze calculations where the haze may vary vertically but not horizontally. The model has several major components which are summarized in figure 69. The original model (Williams et al, 1980, and Nochumson et al, 1982) used a simple Gaussian dispersion model, but a version has been developed that uses RAPTAD solutions. Chemistry in the model is very limited, and draws upon separate photochemical calculations to derive conversion times and size distributions.

There are two rather different situations to which the model can be applied. The simplest situation is a uniform haze wherein the composition of the haze is known and the model merely calculates the radiative transfer within the atmosphere and constructs the appropriate outputs. The radiative transfer is treated with a technique developed by Braslau and Dave (Braslau and Dave, 1980) which solves radiative transfer through a plane parallel atmosphere. In LAVM only absorption, Mie and Rayleigh scattering are treated. The second case of interest is the coherent plume. In this case there are several steps: (1)

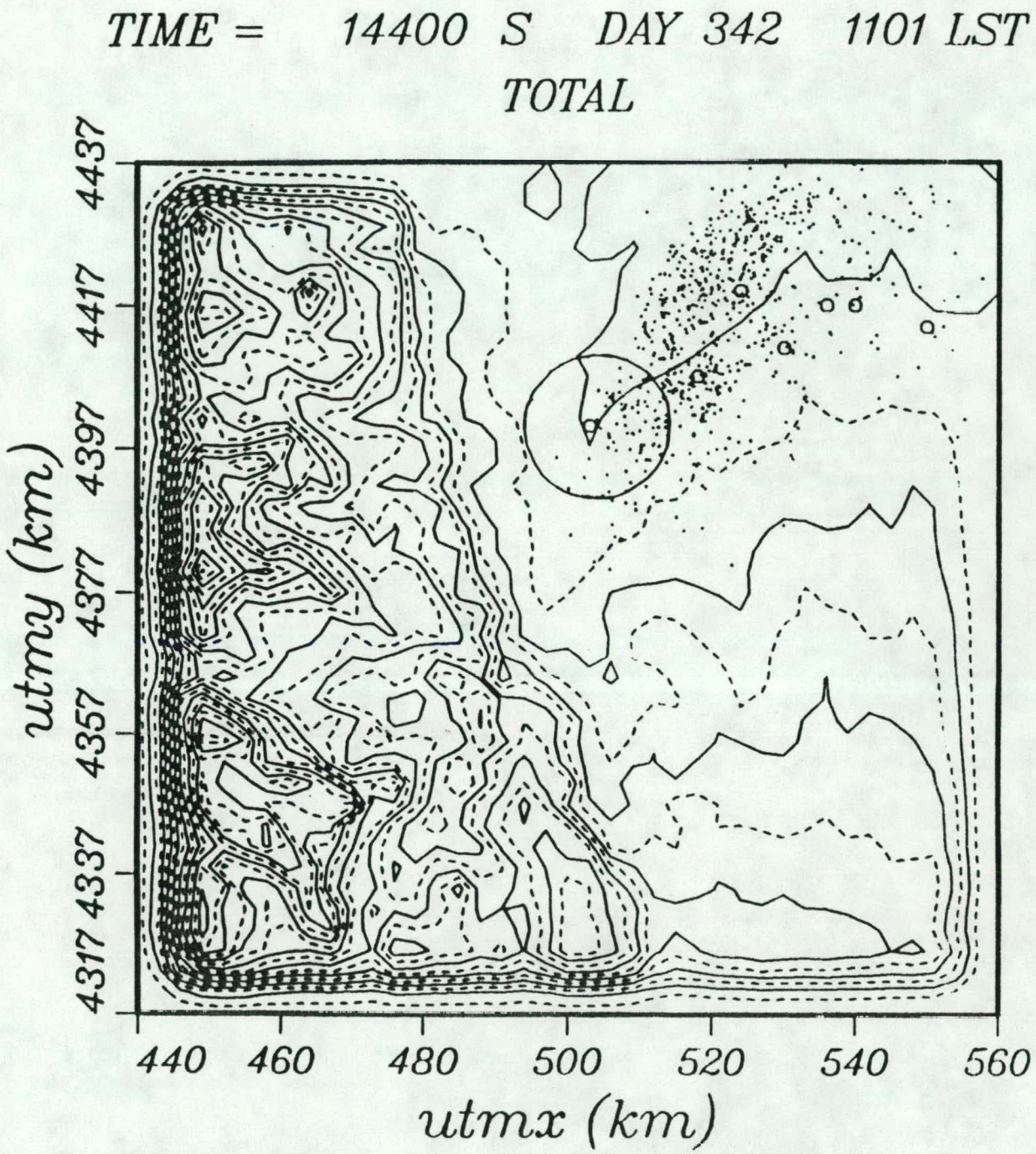

Figure 60: Pseudo-particle Positions at 11 am on the Snow Day

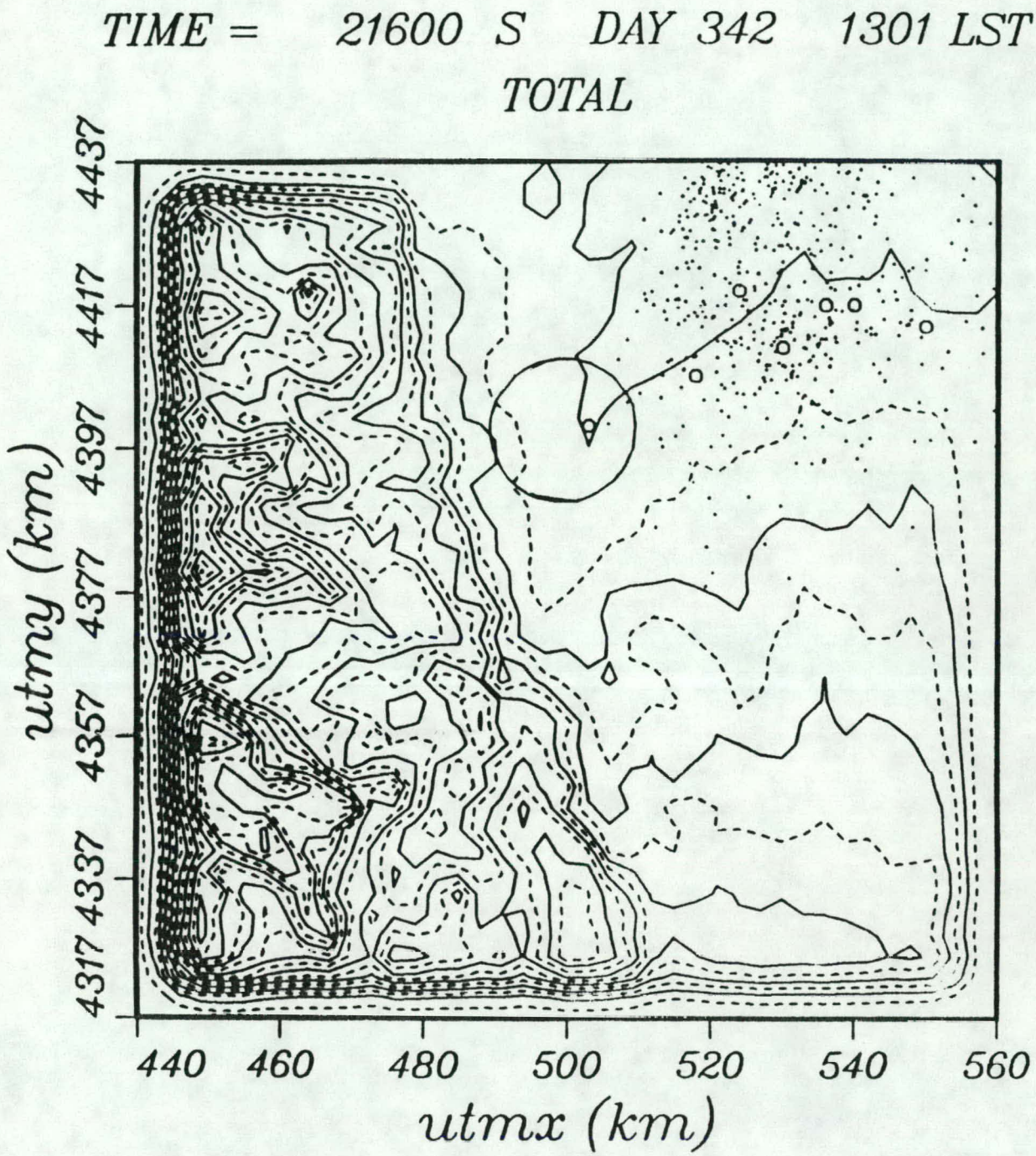

Figure 61: Pseudo-particle Positions at 1 pm on the Snow Day

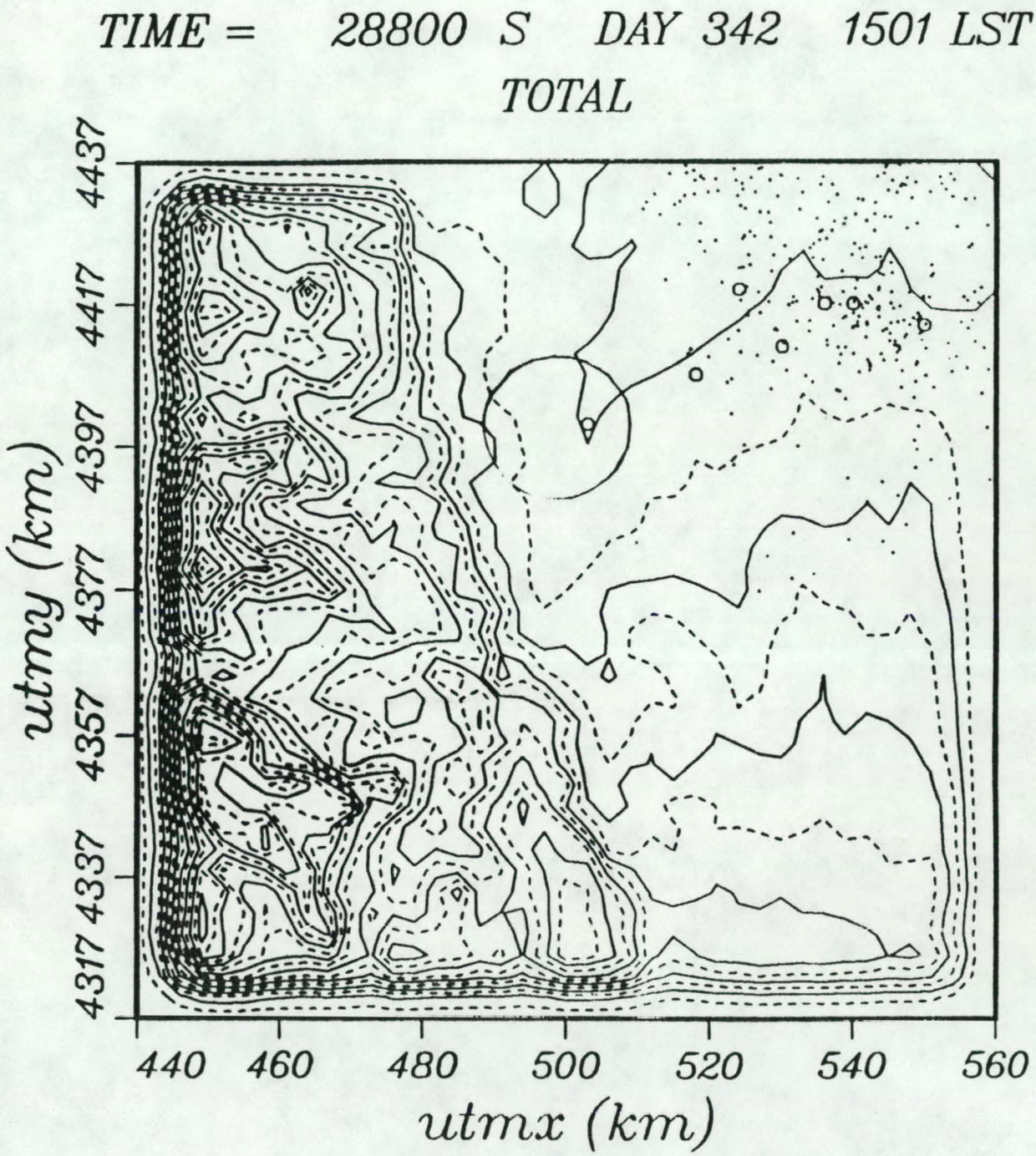

Figure 62: Pseudo-particle Positions at 3 am on the Snow Day

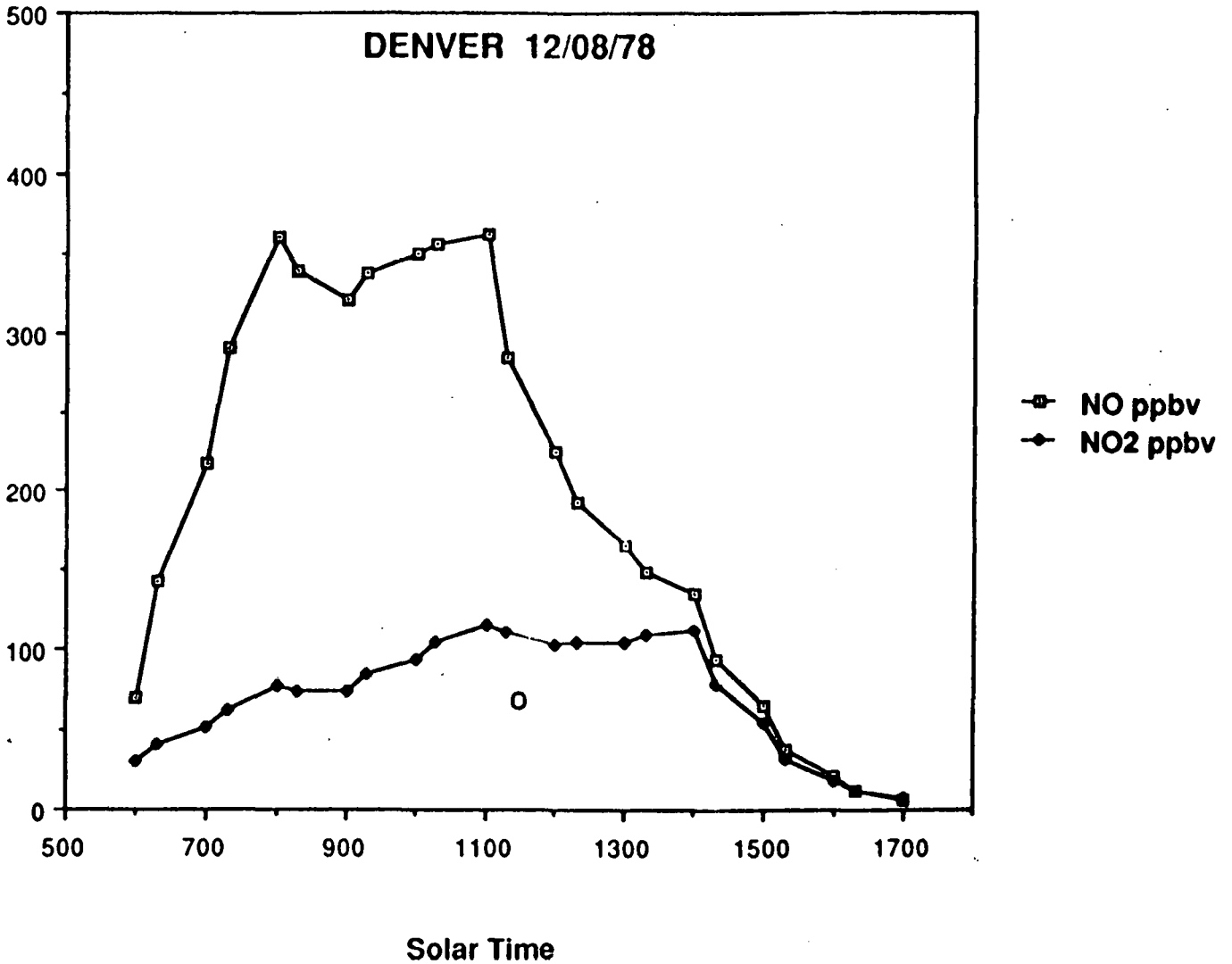

Figure 63: Modeled NO and NO_2 concentrations on the Snow Day

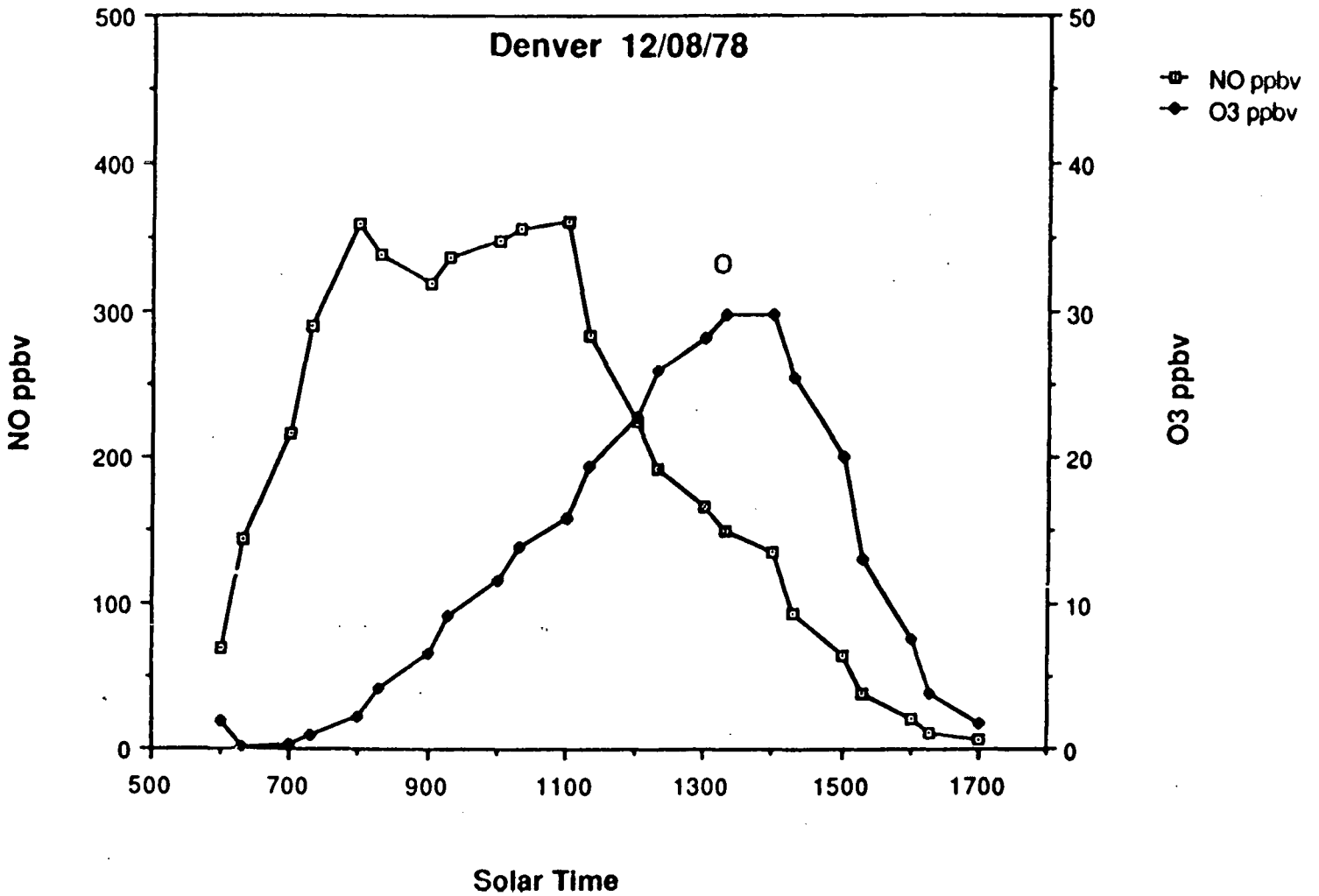

Figure 64: Modeled NO and Ozone concentrations on the Snow Day

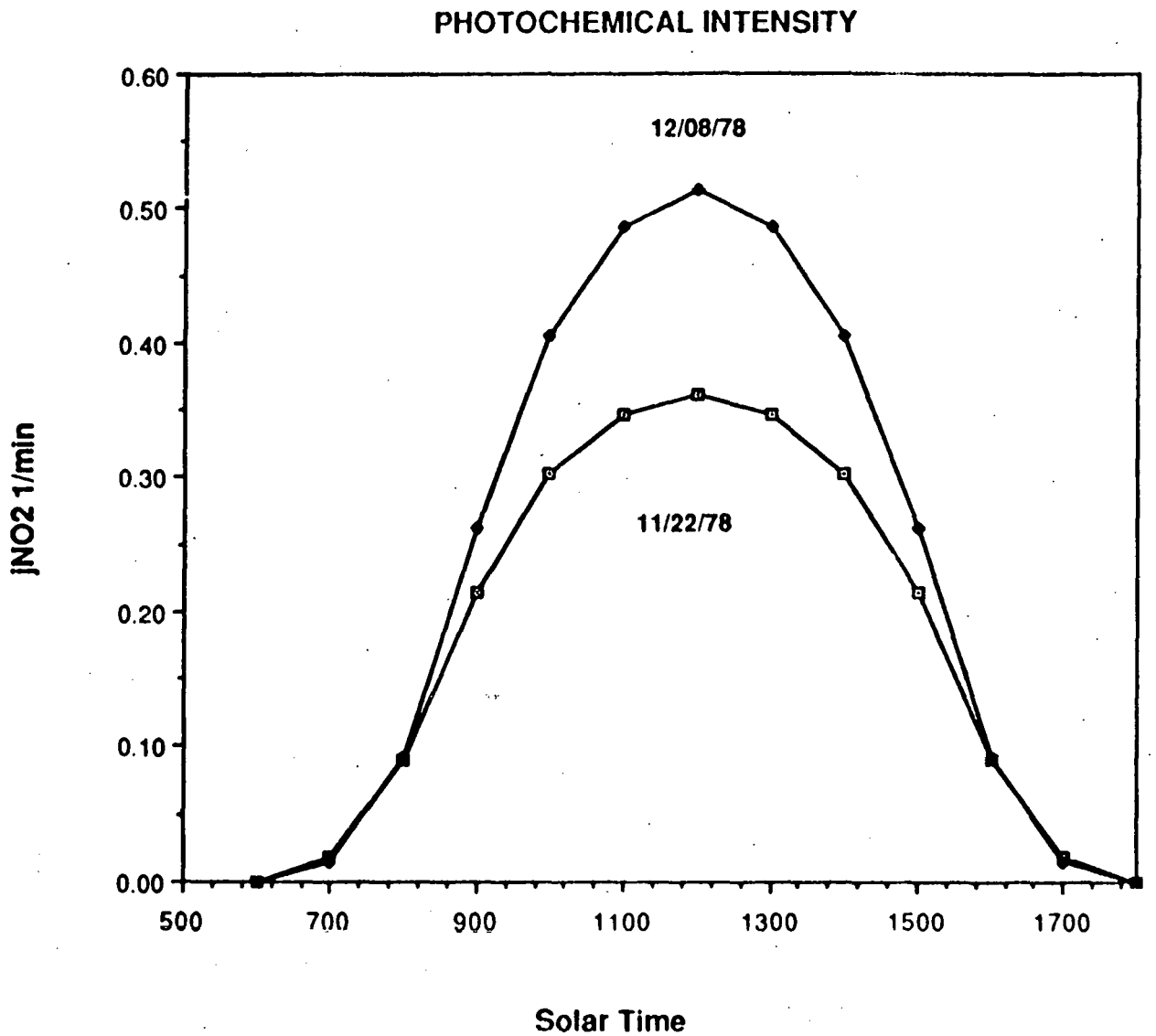

Figure 65: Modeled Photochemical Intensity on two Days

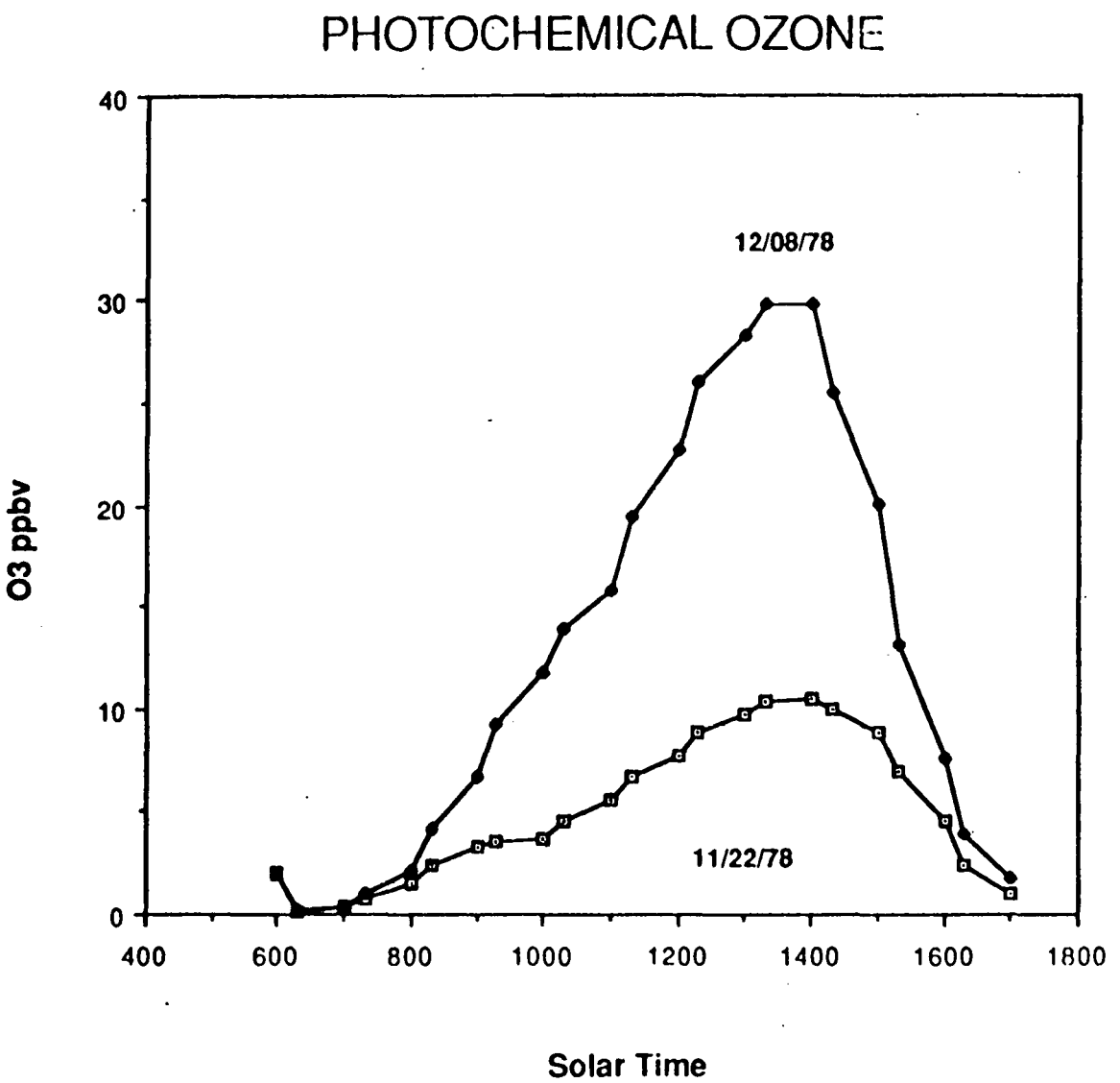

Figure 66: Comparison of Modeled Ozone Concentrations on the two Days

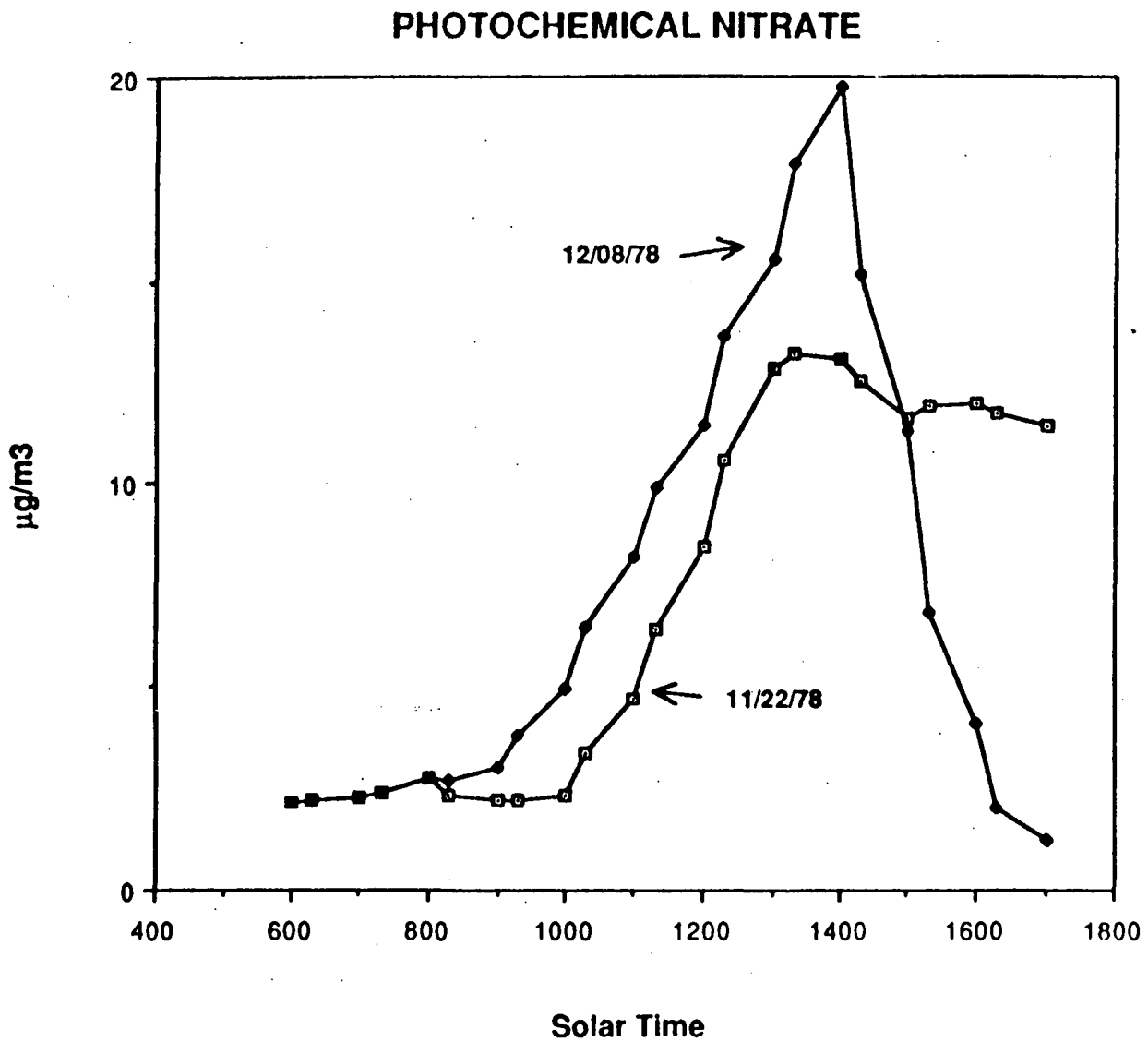

Figure 67: Comparison of Modeled Nitrate Concentrations on the two Days

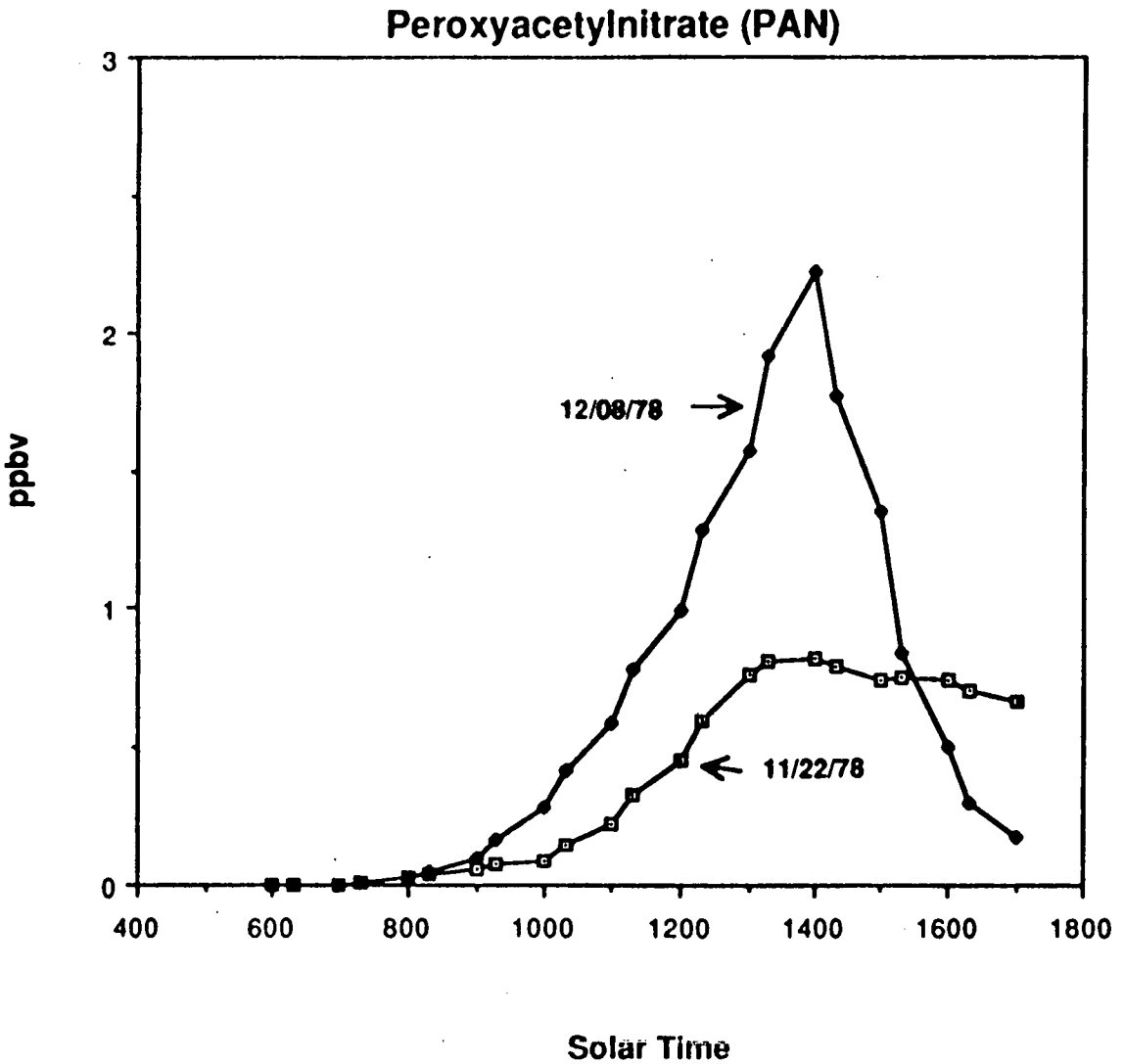

Figure 68: Comparison of Modeled Peroxyacetylnitrate Concentrations on the two Days

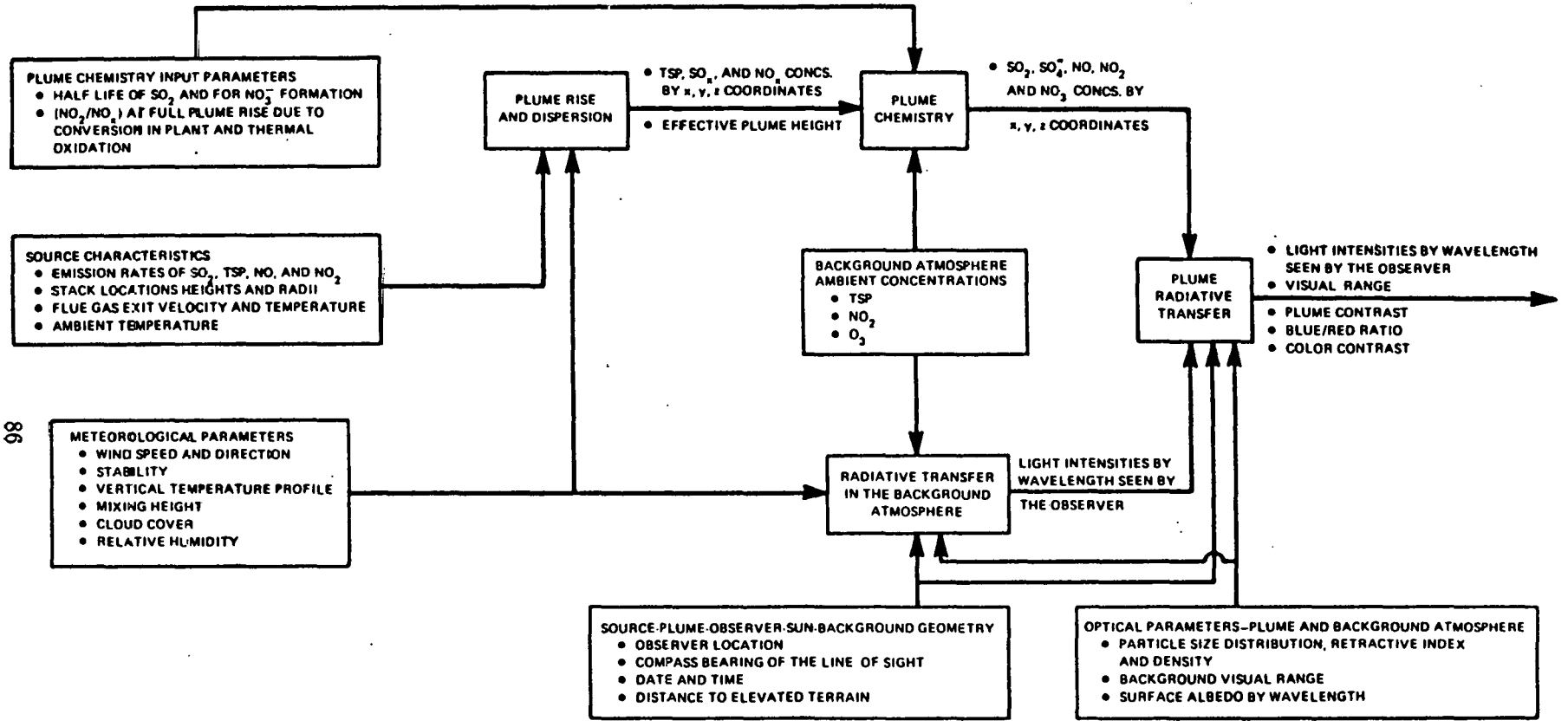

Figure 69: Schematic Logic Flow Diagram of the Visibility Model

modeling the radiative transfer in the background atmosphere, (2) modeling plume dispersion, (3) modeling plume chemistry and optical parameters, and (4) modeling of plume radiative transfer. The radiative transfer in the background atmosphere is treated in the same manner as the uniform haze case. For dispersion the most current form of the model uses RAPTAD to provide concentrations along a line of sight. The chemistry is expressed in terms of constant conversion rates which are estimated from photochemical model results. The one exception to this rule is the formation of NO_2 from NO which is given by:

$$[NO_2] = \beta\{(1-d_f)[O_{3b}] + (1-d_f)[NO_{2b}]\} + \left(\frac{[NO_2]}{[NO_x]}\right)_0 [NO_x], \qquad (28)$$

when the plume NO_x is comparable or greater than the background ozone. Otherwise the NO_2 concentrations are taken as 70% of the NO_x concentrations. The coefficient β is taken as 1. for neutral and unstable conditions which represents a simple titration of NO by background ozone. During stable conditions the photochemical model indicated that there was a significant conversion produced by the termolecular reaction of NO with ambient oxygen. A coefficient of 1.4 provided a good description of the photochemical results for stable conditions. The resulting concentrations are multiplied by the appropriate scattering or absorption coefficients to obtain absorption optical length and Mie scattering optical depths. The plume radiative transfer is then solved for a plane parallel plume oriented normal to the line of sight with boundary conditions derived from the background radiative transfer solution. Plumes are highly non-uniform so that the assumption that they can be approximated by semi-infinite planes is questionable, but the comparison with measurements to date has shown good agreement for the radiative transfer components of the model. In the future a Monte-Carlo radiative transfer code might be used for the plume radiative transfer calculations to provide a more realistic treatment. If a picture is desired as output the simulated photograph technique is used. Figure 70 depicts schematically the procedure with the exception that newer computers are now in use. Original brightnesses are obtained from the digitized clean scene. The apparent brightness of mountain as seen by the observer can be written as:

$$B_T = Tr_b B_0 + S_a \qquad (29)$$

where B_0 represents the inherent brightness of the object, Tr_b is the fractional transmission of light from the object to the observer, and S_a is the additional light scattered by the atmosphere in the line of sight which reaches the observer. The model calculates a new brightness which is given by:

$$B^* = Tr_p B_T + S_{ap}, \qquad (30)$$

which is:

$$B^* = Tr_p Tr_b B_0 + Tr_p S_a + S_{ap}. \qquad (31)$$

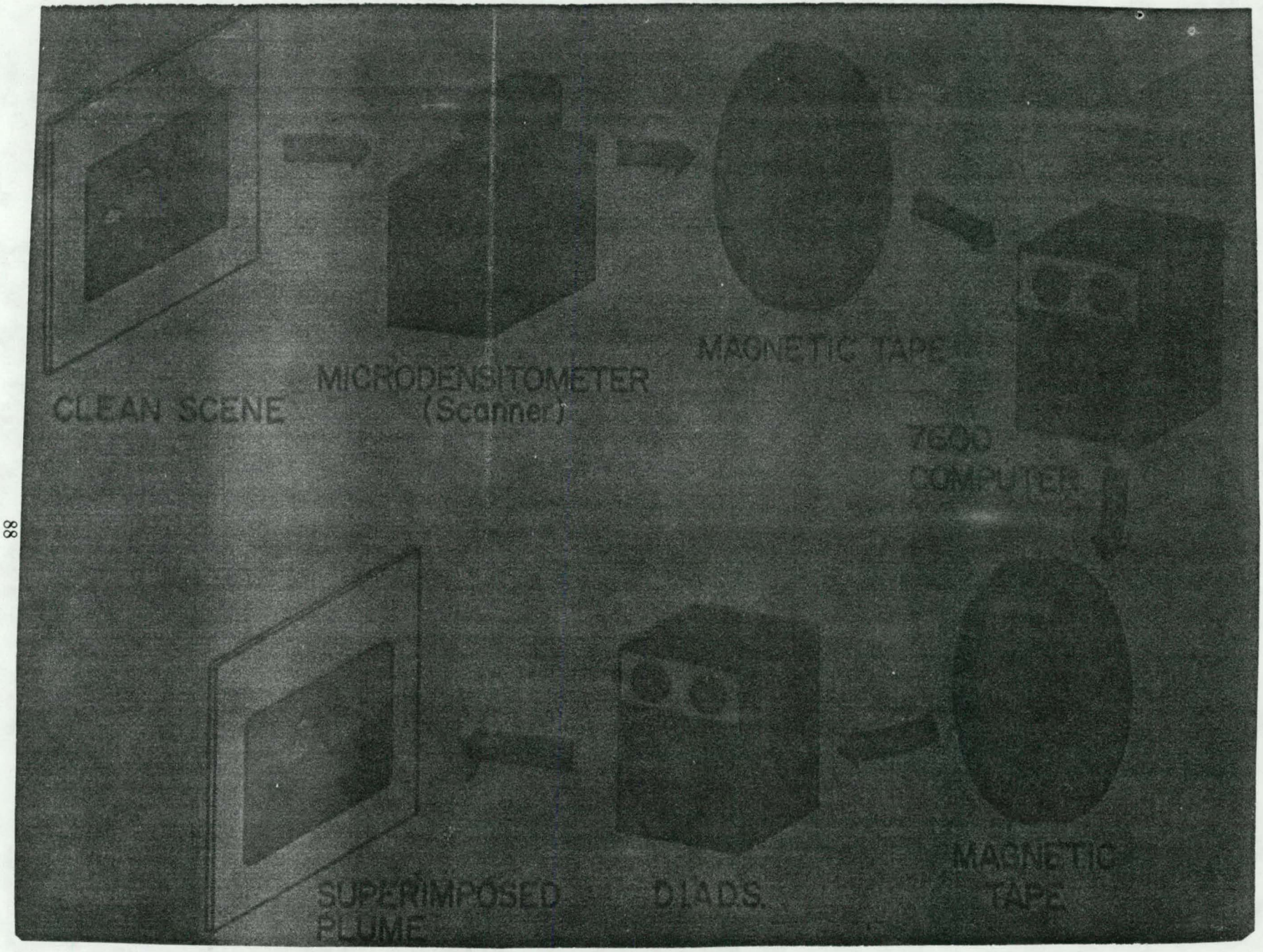

Figure 70: Schematic of the Simulated Photograph Technique

The brightness is obtained from the film density by using the films gamma curve. In practice the gamma curve is obtained from a photograph of a gray scale. The model calculates the plume transmission and the plume scattering for each line of sight and each of three primary colors, blue, green, and red. Typically a 10 by 10 array of the lines of sight will be used for a given scene with interpolated values used between.

Figure 71 displays a clean scene of Lake Tahoe. Figure 72 displays the scene after the addition of sufficient diesel aerosol to cut the visual range in half. Figure 73 displays a clean scene of Arches National Park in the state of Utah. Figure 74 displays the same scene with the plume of a large coal-fired power plant with good particulate controls drifting across it.

LAVM has been used to address questions such as the role of NO_2 in the Denver brown haze, the effects of diesel aerosols in California, and implications of Clean Air Act amendments on development and the environment in the southwestern United States (Williams, et al., 1981).

7 Conclusions

Los Alamos investigators have developed a combination of air quality modeling tools which can address a variety of circumstances and provide a variety of outputs. The HOTMAC atmospheric circulation model provides a sophisticated treatment of atmospheric processes which can provide turbulence input to an advanced dispersion code. HOTMAC is very important for describing the atmosphere in situations where complex terrain plays an important role. It is also very useful where the atmospheric measurements are sparse or unrepresentative. RAPTAD is an efficient dispersion code which can describe complex situations correctly. It has proven to be greatly superior to Gaussian puff models in representing behavior of near surface releases. The atmospheric chemistry component of the system has dealt effectively with a variety of situations including transport of the Tokyo plume to the Japanese Alps, the oxygenated fuel environment of Rio De Janiero, and the high altitude winter environment of Denver. The Los Alamos Visibility Model has the capability of producing "before" and "after" photographs which are very helpful in communicating model results to lay persons. It can also treat a variety of situations.

8 REFERENCES

T. Yamada, 1985: "Numerical Simulation of the Night 2 Data of the 1980 ASCOT Experiments in the California Geysers Area," Archives for Meteorology, Geophysics, and Bioclimatology, Ser. A34, pp 223-247.

G. I. Mellor, and T. Yamada, 1982: "Development of a Turbulence Closure

Figure 71: Clean Scene of Lake Tahoe

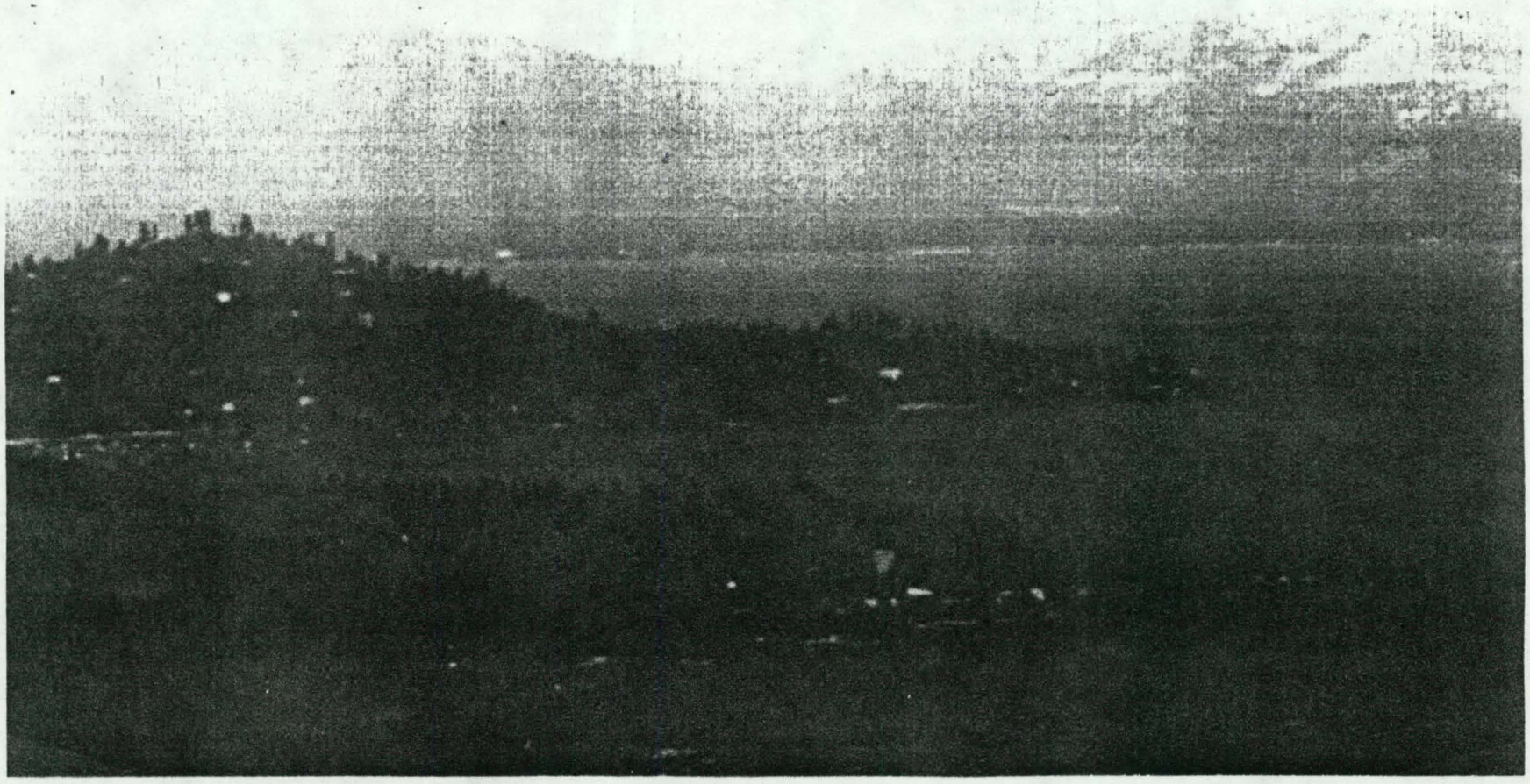

Figure 72: Lake Tahoe with Visual Range Reduced in Half by Diesel Aerosols

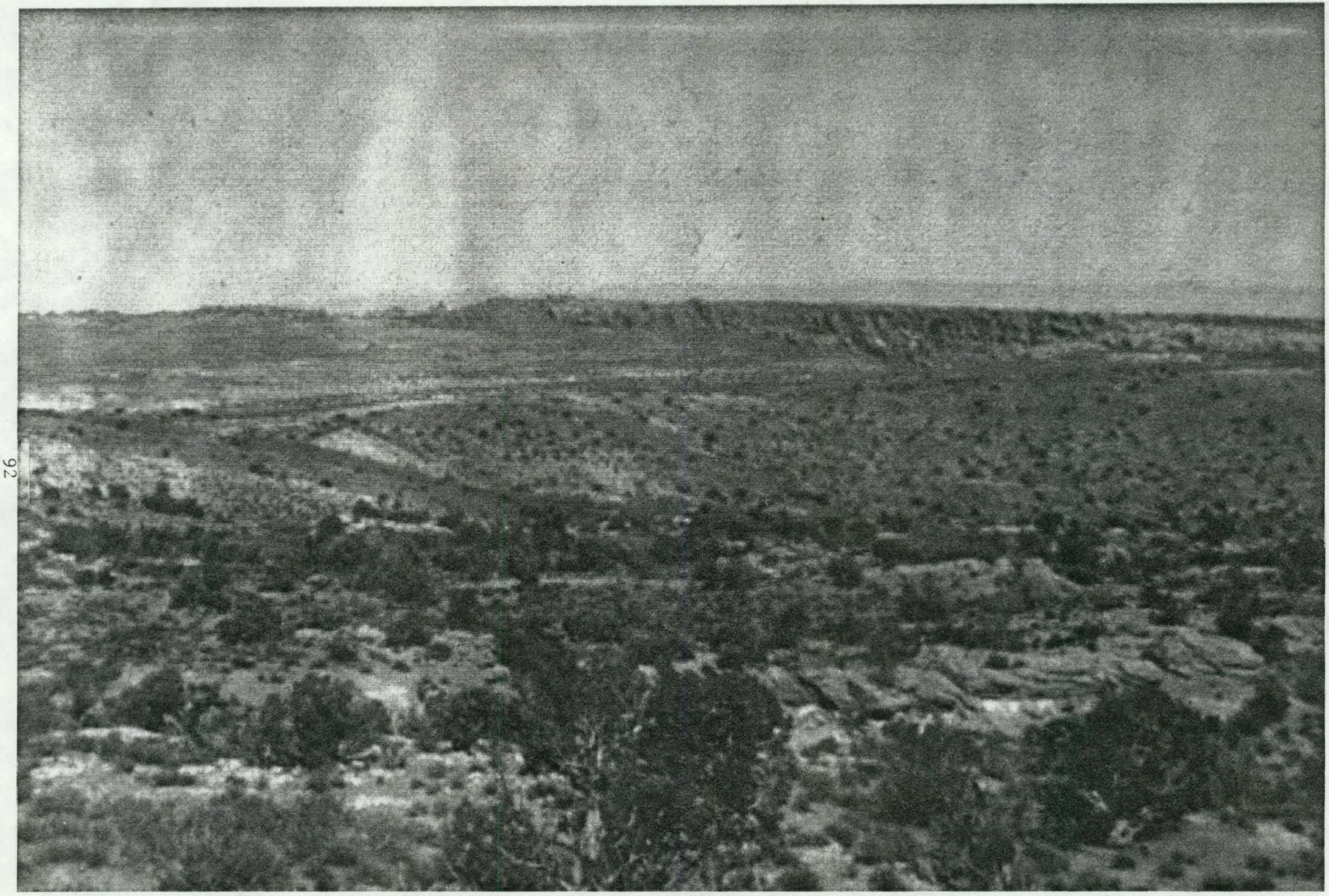

Figure 73: Clean Scene of Arches National Park

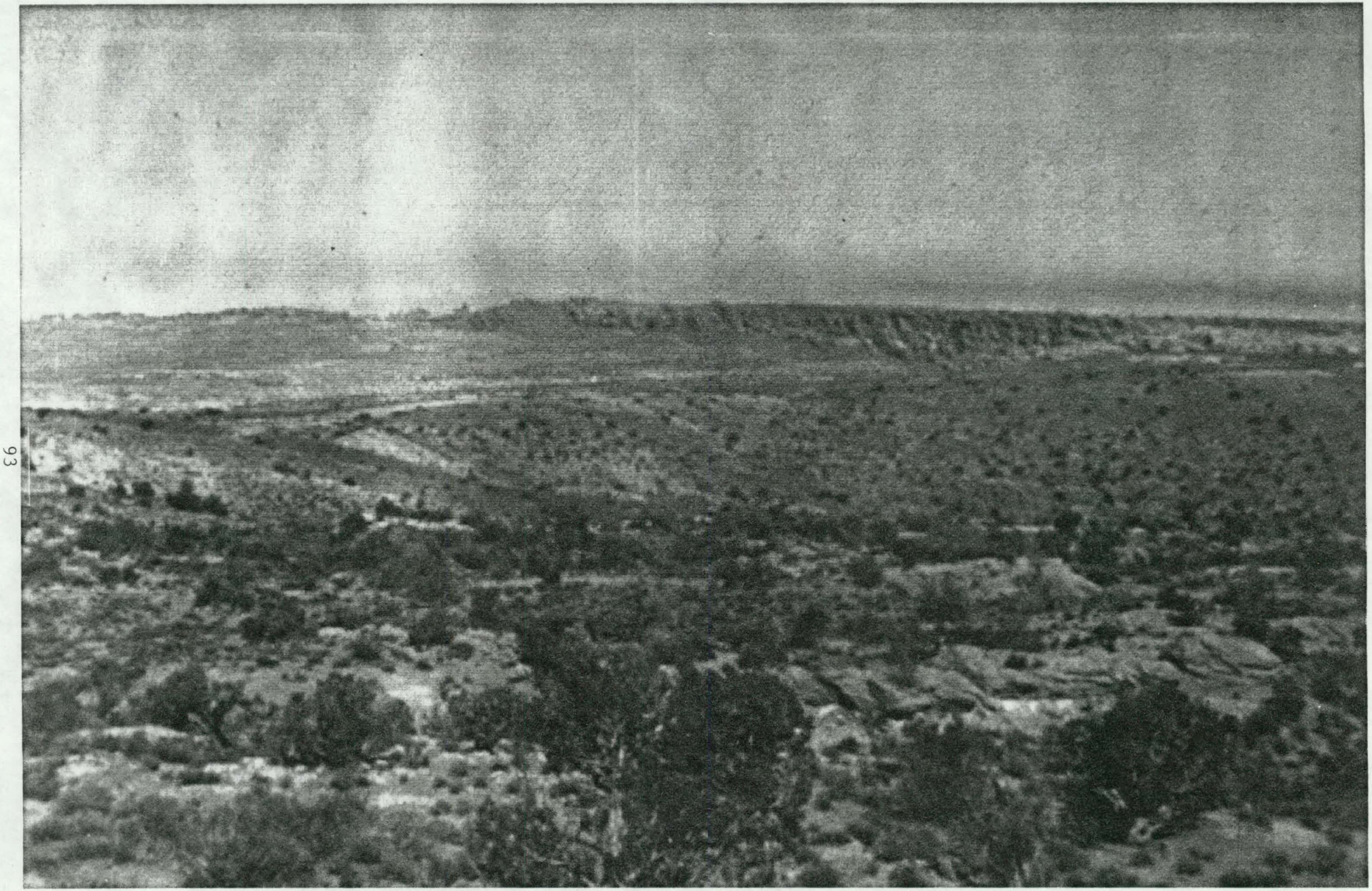

Figure 74: Scene of Arches National Park with Plume from a Power Plant

Model for Geophysical Fluid Problems," Rev. Geophys. Space Phys., vol 20, pp 851-875.

T. Yamada, 1982: "A Numerical Model Study of Turbulent Airflow in and Above a Forest Canopy," J. Meteor. Soc. Japan, vol 60, pp 439-454.

T. Yamada, 1981: "A Numerical Simulation of Nocturnal Drainage Flow," J. Meteor. Soc., Japan, vol 59, pp 108-122.

A. J. Dyer, and B. B. Hicks, 1970: "Flux-Gradient Relationships in the Constant Flux Layer," Quart. J. Roy. Meteor. Soc., vol 96 pp 715-721 .

T. Yamada, and S. Bunker, 1988: "A Numerical Model Study of Nocturnal Drainage Flows with Strong Wind and Temperature Gradients," it J. Appl. Meteor., (submitted,).

T. Yamada, 1975: "The Critical Richardson Number and the Ratio of the Eddy Transport Coefficients Obtained from a Turbulence Closure Model," J. Atmos. Sci., vol 32 pp926-933.

T. Yamada, 1978: "A Three-Dimensional, Second-Order Closure Numerical Model of Mesoscale Circulations in the Lower Atmosphere," Argonne National Laboratory, ANL/RER-78-1, 67 pp. Available from National Technical Information Service, U.S. Department of Commerce, 5285 Port Royal Road, Springfield, VA 22161.

R. J. Legg and M. F. Raupach, 1982: "Markov-Chain Simulation of Particle Dispersion in Inhomogeneous Flows: The Mean Drift Velocity Induced by a Gradient in Eulerian Velocity Variance," Boundary-Layer Meteorol., vol 24 pp3-13.

G. I. Taylor, 1921: "Diffusion by Continuous Movements," Proceedings of the London Mathematical Society, Ser. 2, vol 20 pp196-211 .

T. Yamada, M. Williams, and G. Stone, 1989: "Chemical Downwind Hazard Modeling Study", Los Alamos National Laboratory LA-UR-89-1061,

G. T. Wolff, R. J. Countess, P.J. Groblicki, M. A. Ferman, S. H. Cadle and J.

L. Muhlbaier, 1981: "Visibility-Reducing Species in the Denver Brown Cloud -II. Sources and Temporal Patterns," Atmospheric Environment vol 15. pp 2485-2502.

M. D. Williams, C. Mangeng, S. Barr, and R. Lewis, 1981: "Air Quality in the Four Corners Study Region–vol. I: Local Analysis," Los Alamos National Laboratory LA-UR-81-1145.

M. D. Williams, E. Treiman, and M. Wecksung, 1980: "Plume Blight Visibility Modeling with a Simulated Photograph Technique," APCA Journal, vol. 30, pp 131-134.

David H. Nochumson, Michael D. Williams, Lo Yin Chan, and Renate J. Lewis, 1982: "User's Manual for the Los Alamos Visibility Model (LAVM)," Los Alamos National Laboratory, LA-UR-82-1322.